LICENCIATURA EN FISICA MEDICA

BIOFISICA

CAPITULO 11. Parte 4.

La Luz. La Electromagnética. La Optica. La Fotónica. Los Ojos y la Visión Humana

NATURALEZA DE LA LUZ
ONDAS COHERENTES

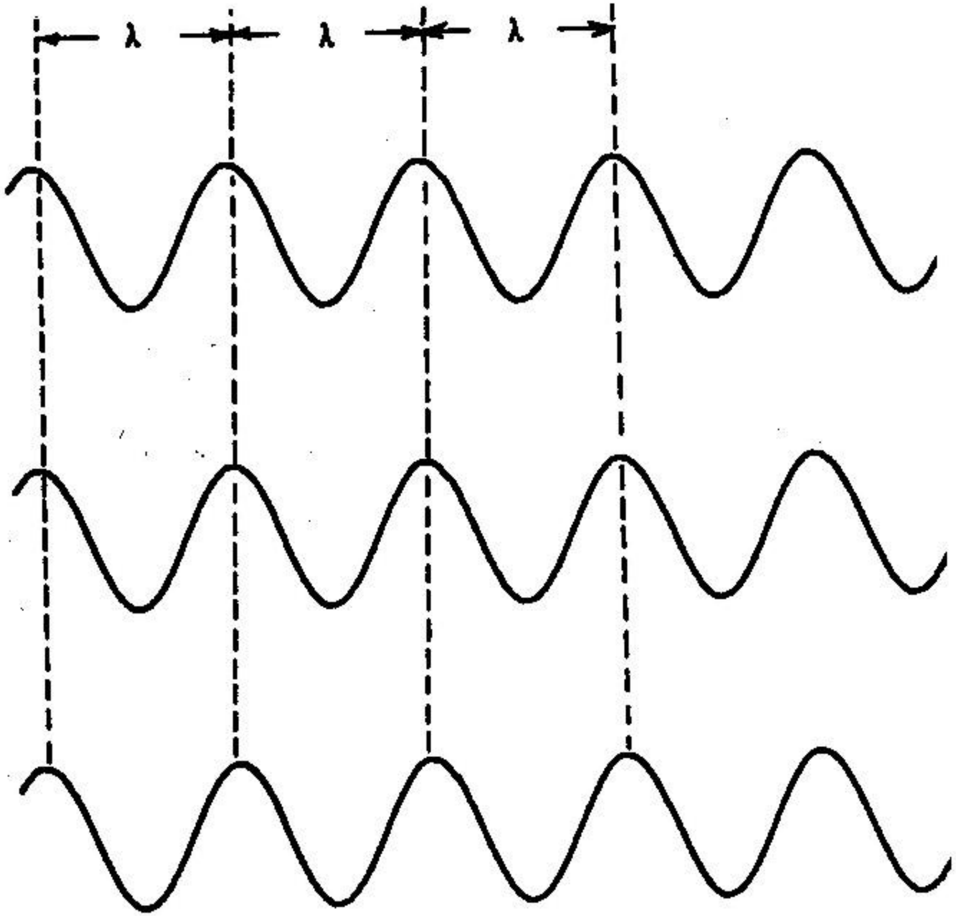

Figure 2-31. Phase relation for temporal coherence. In a laser beam, not only are the waves in step (spatial coherence), but the wavelengths of all the waves are the same and in phase (temporal coherence).

FRENTES DE ONDA E INTERFERENCIA

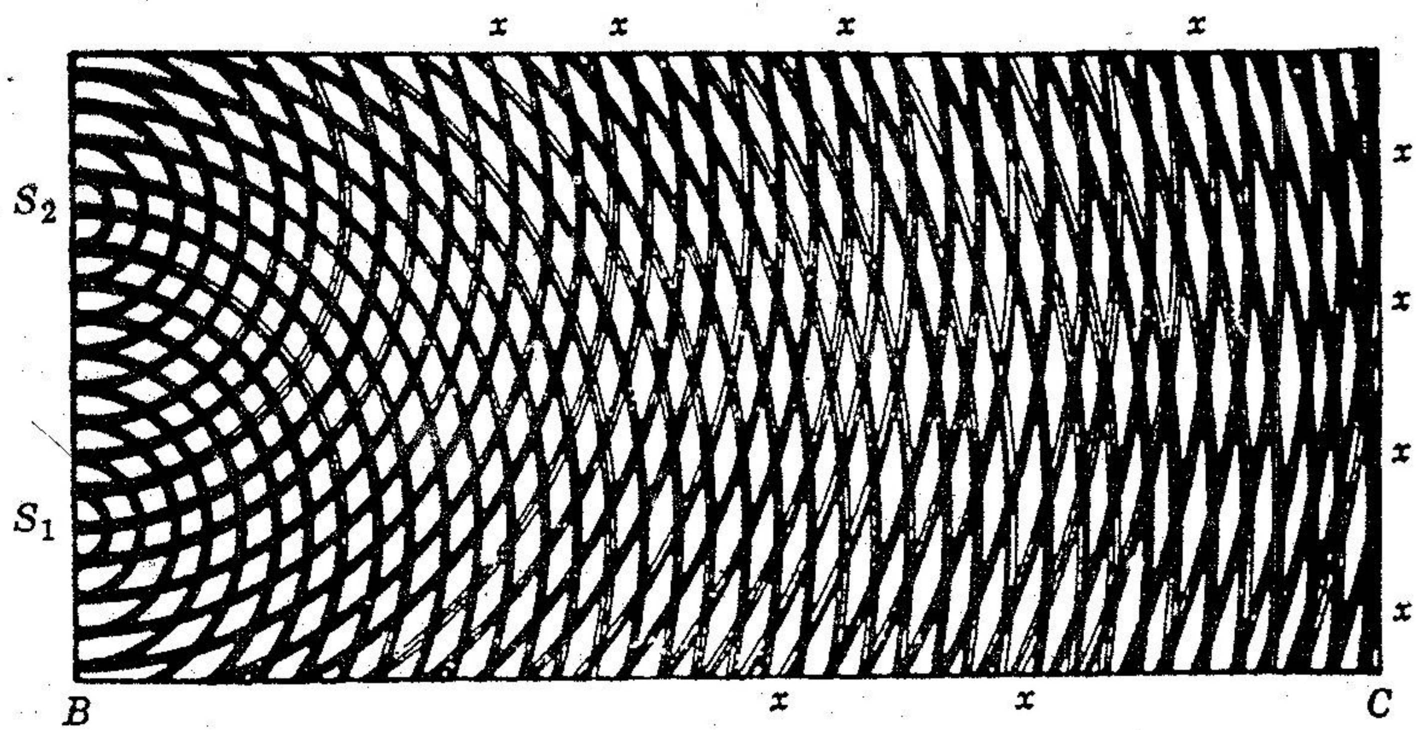

En 1801 Thomas Young ilustró así cómo concebía su Principio de Interferencia de ondas luminosas.

INTERFEROMETRO DE YOUNG

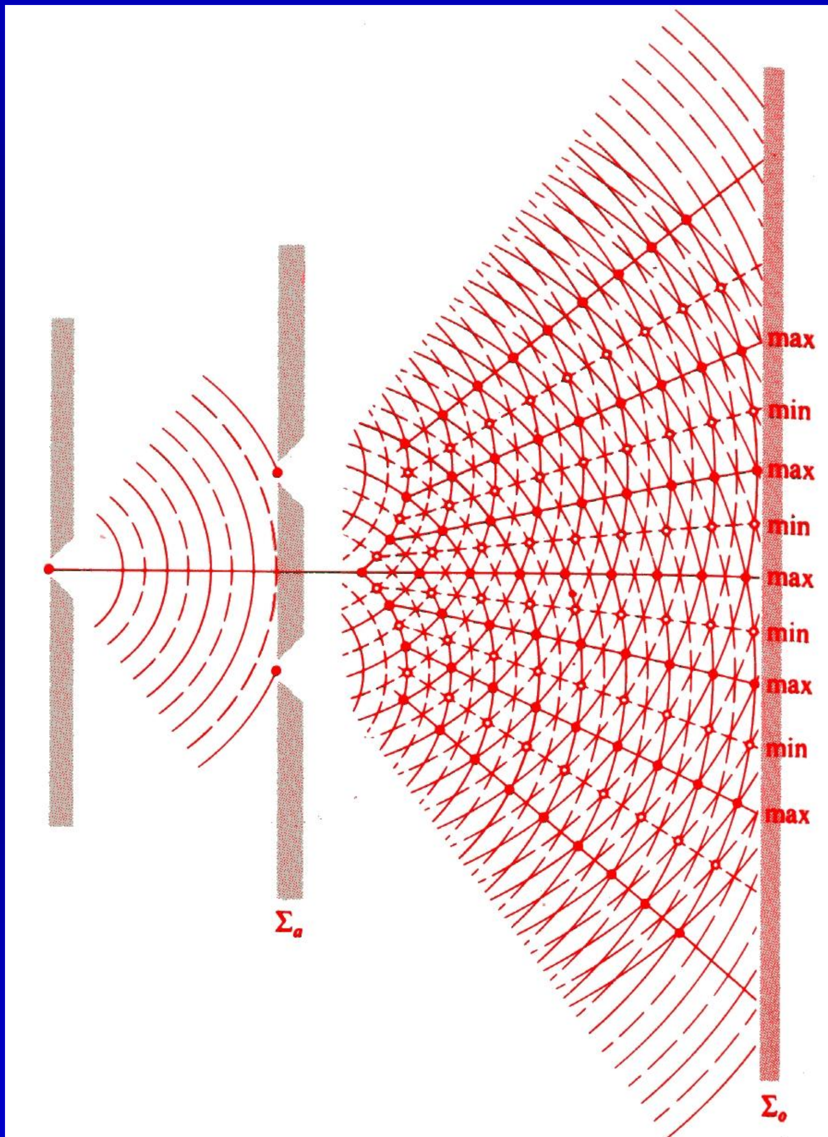

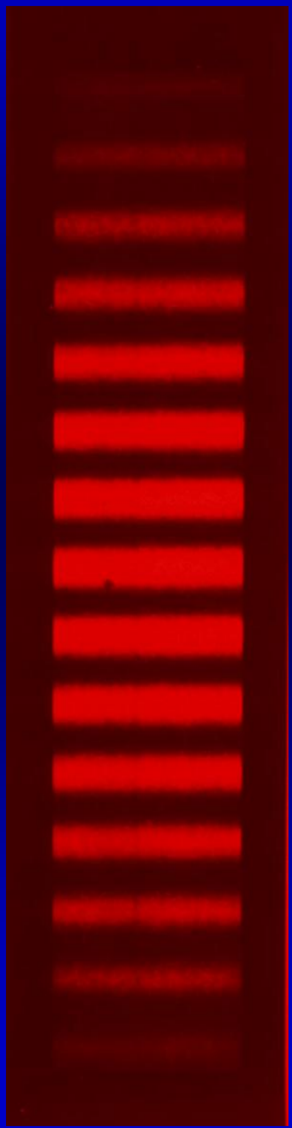

Franjas no localizadas en el espacio y temporalmente estacionarias.

Se lo emplea en la observación clínica de la viabilidad de la intervención por cataratas.

INTERFEROMETRO DE NEWTON I

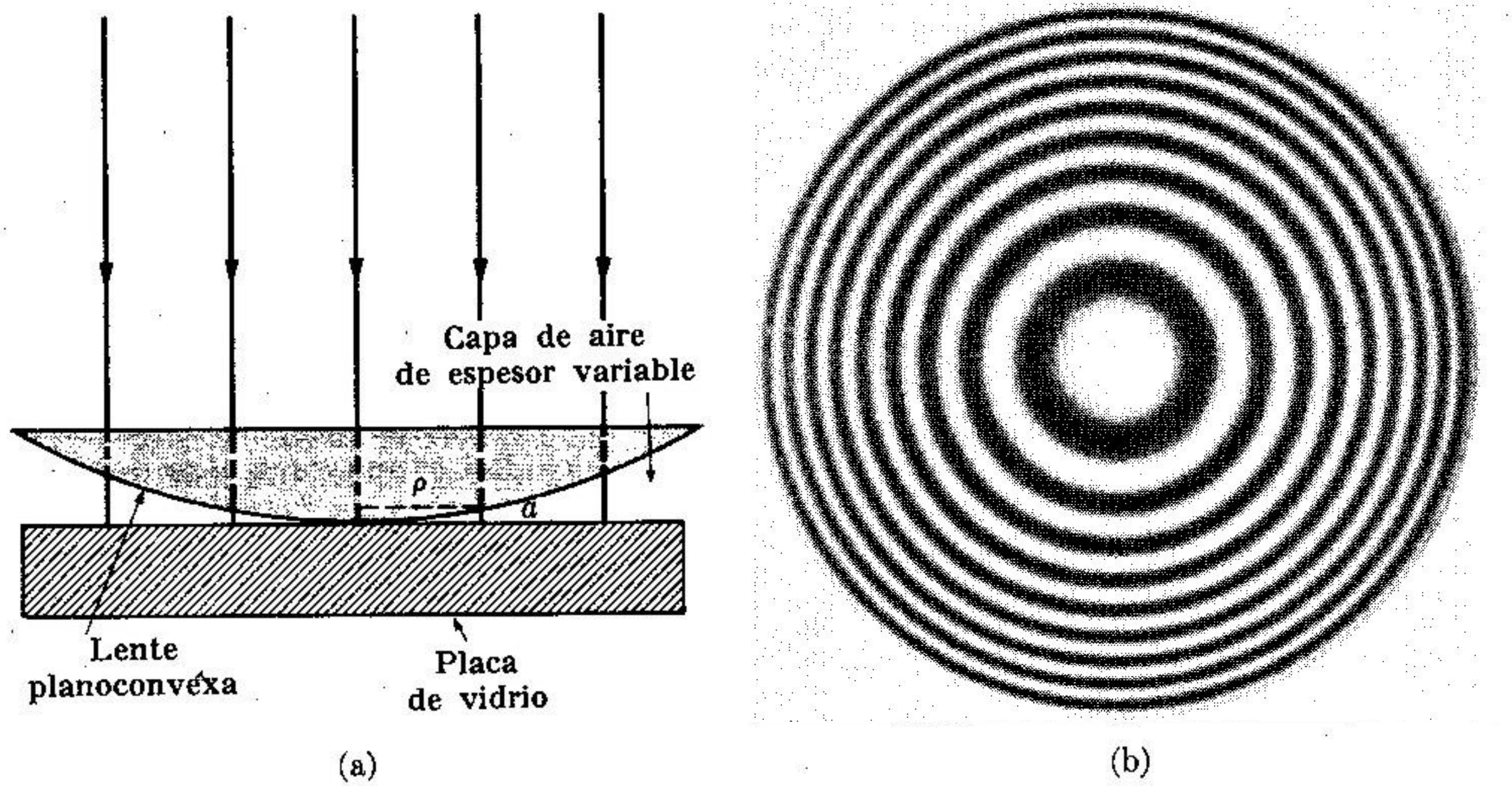

Anillos de Newton, formados por interferencia en la película de aire existente en el espacio entre una superficie convexa y una plana. (a) Dibujo esquemático. (b) Fotografía de los anillos. (Cortesía Bausch and Lomb Optical Co.).

Observados independientemente, hacia 1650, por R. Boyle y R. Hooke.

INTERFEROMETRO DE NEWTON II

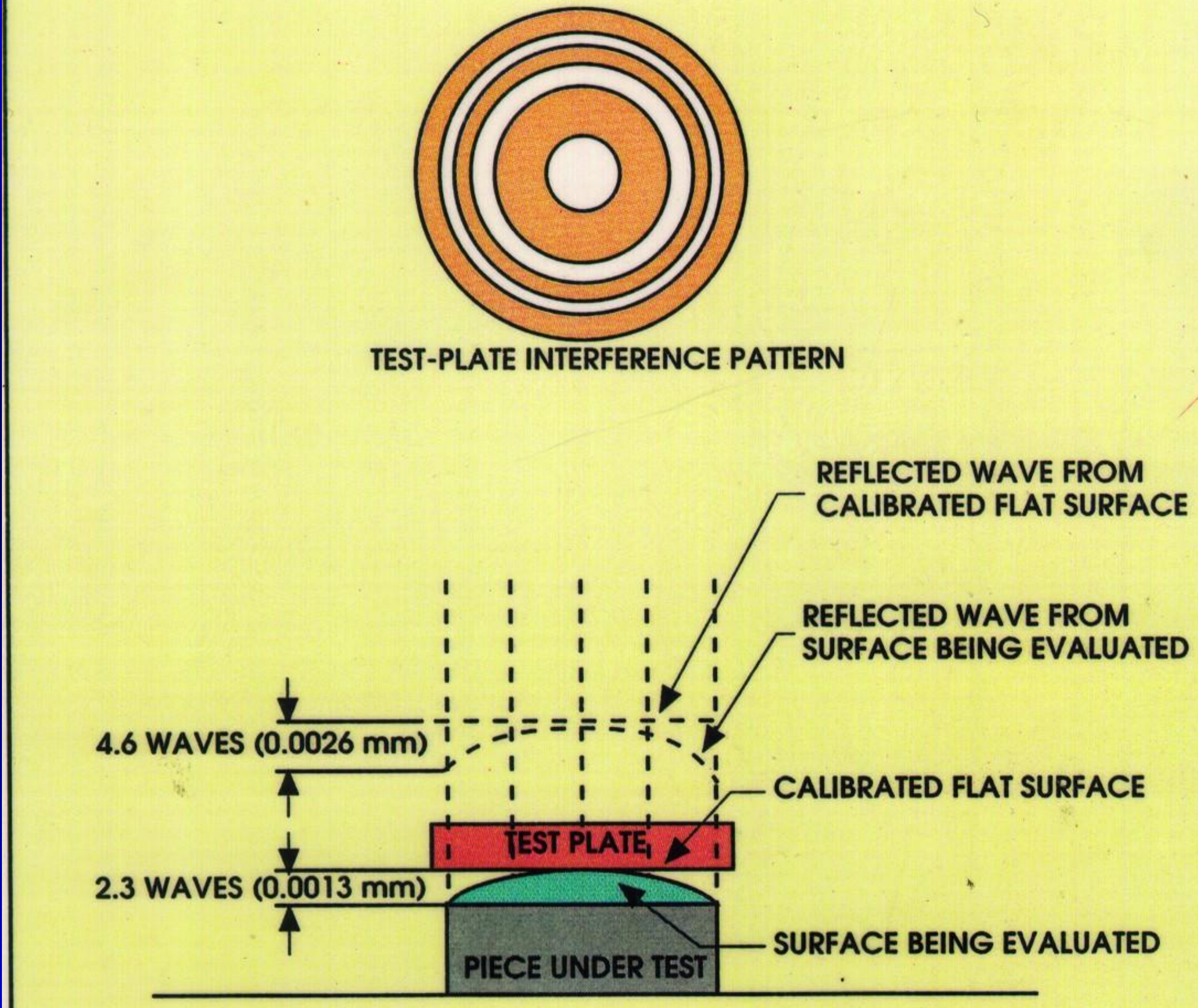

Figure 3. *Test-plate procedure performed on a window with a curved surface.*

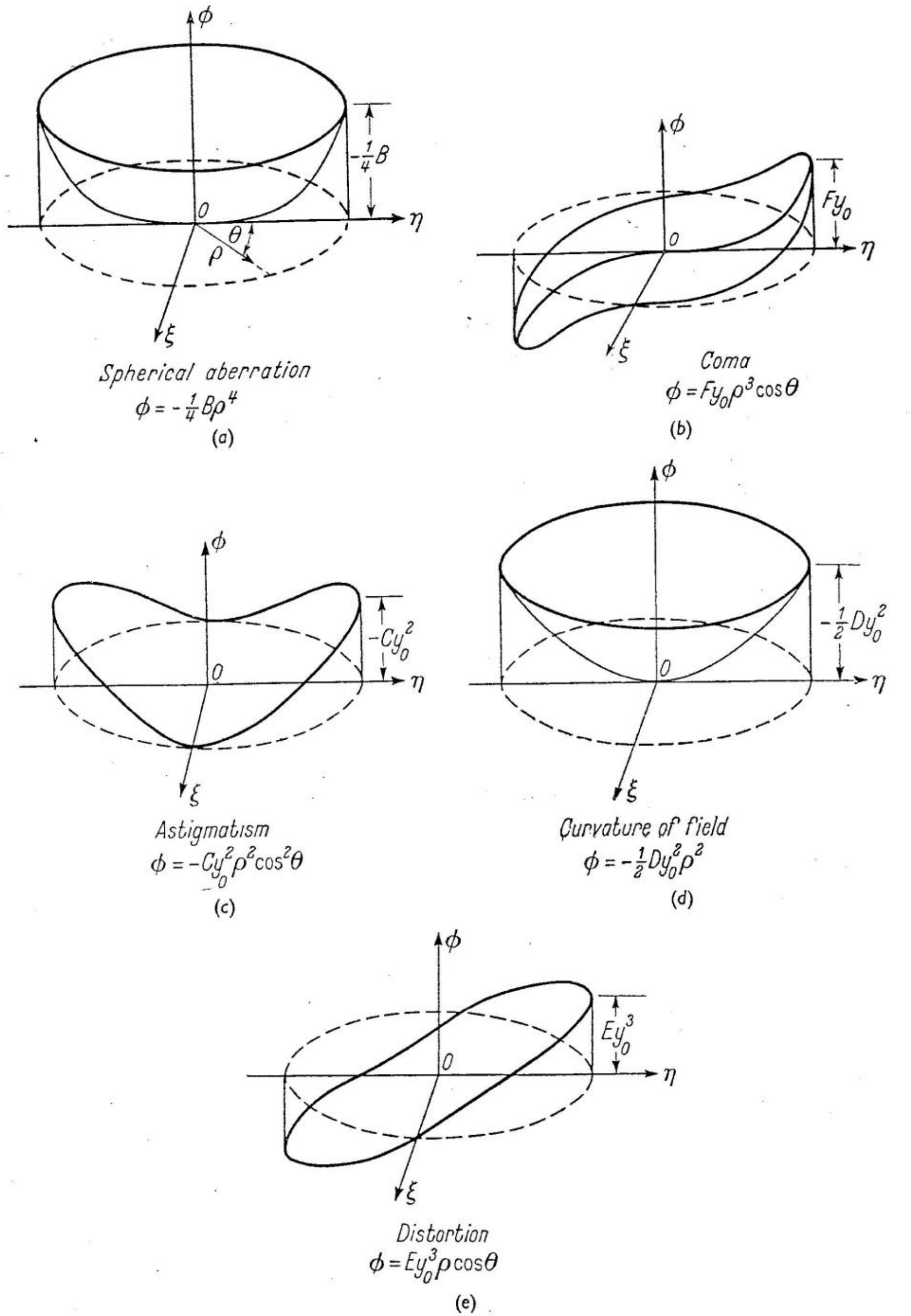

Fig. 5.3. The primary wave aberrations.

INTERFEROMETRO DE NEWTON III

Frentes de onda por aberraciones de von Seidel:
Esférica (ρ^4),
Coma (ρ^3),
Astigmatismo (ρ^2),
Curvatura de campo (ρ^2), y
Distorsión (ρ)

INTERFEROMETRO DE NEWTON IV

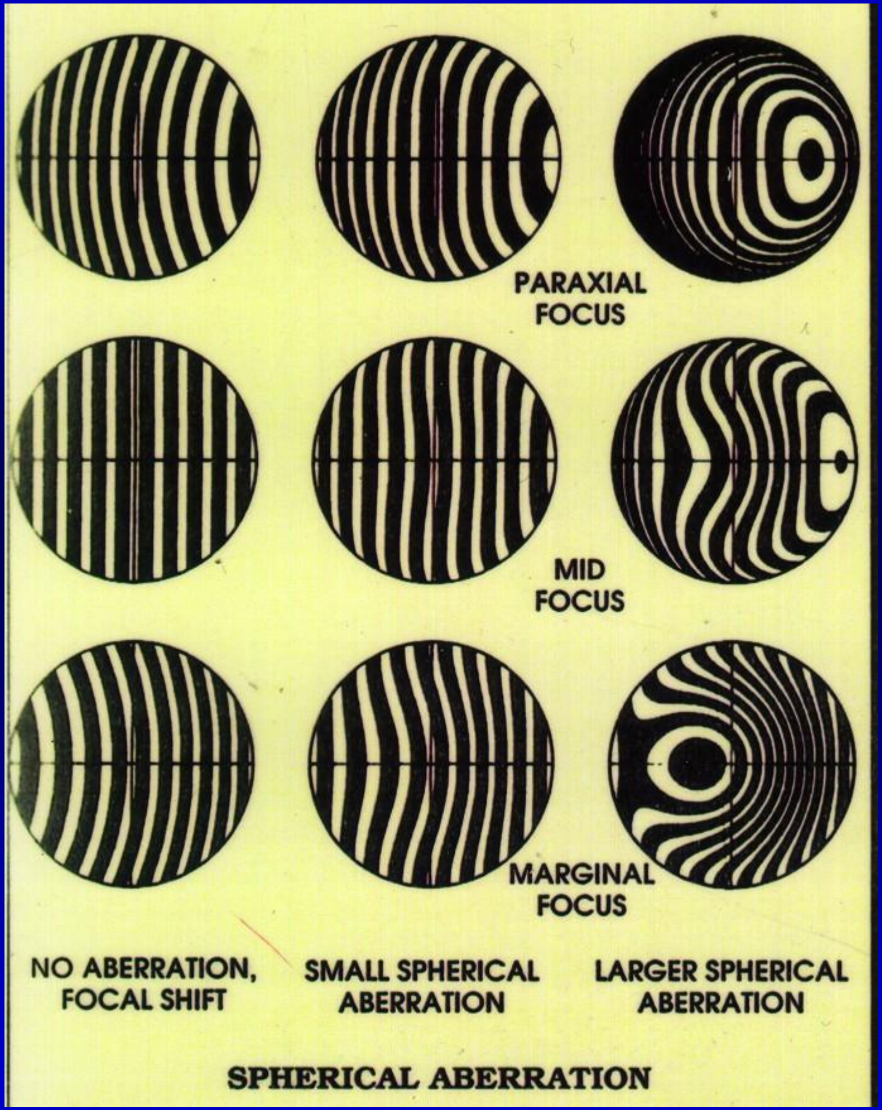

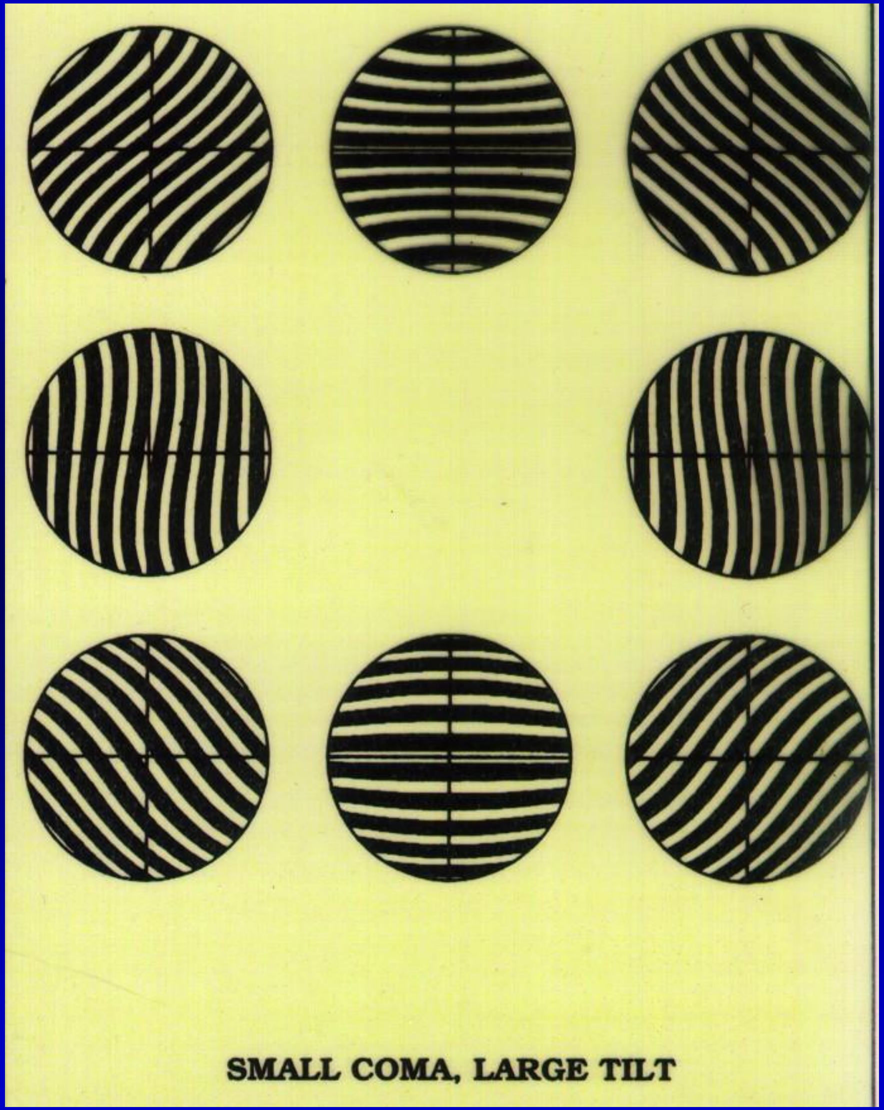

INTERFEROMETRO DE NEWTON V

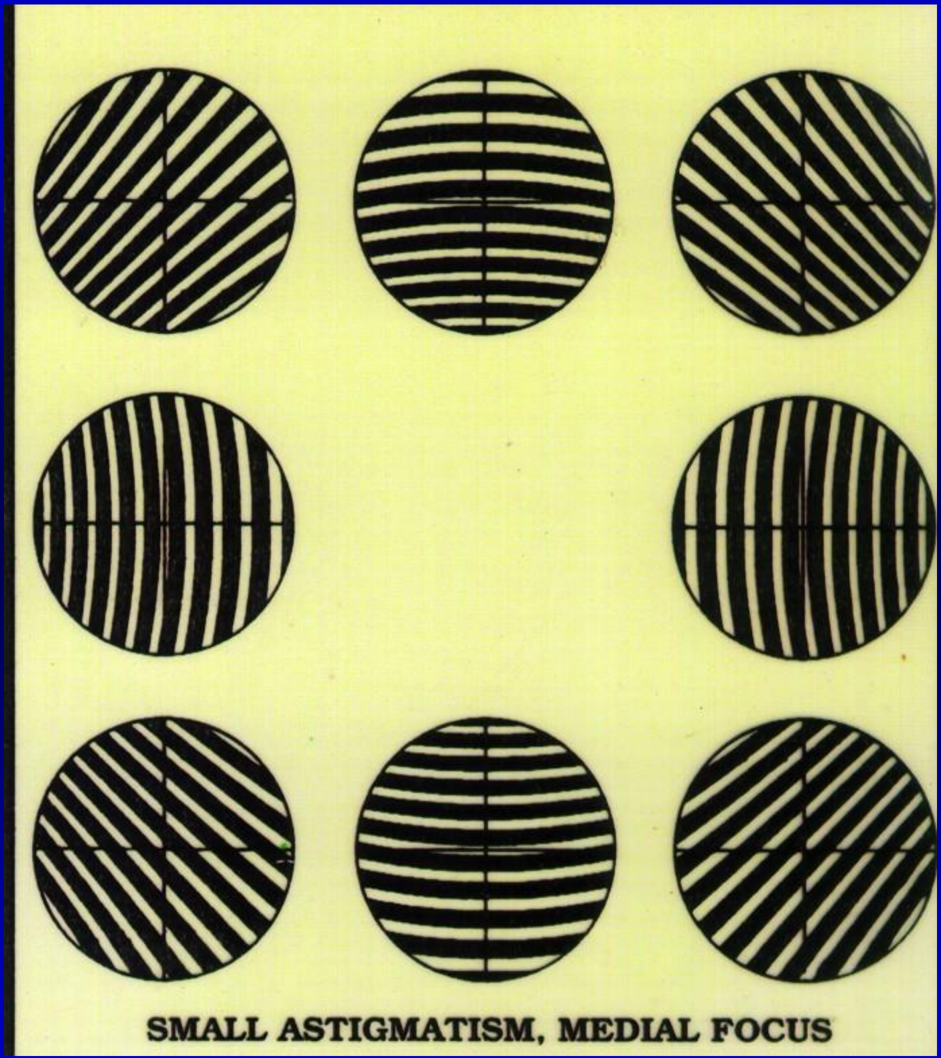

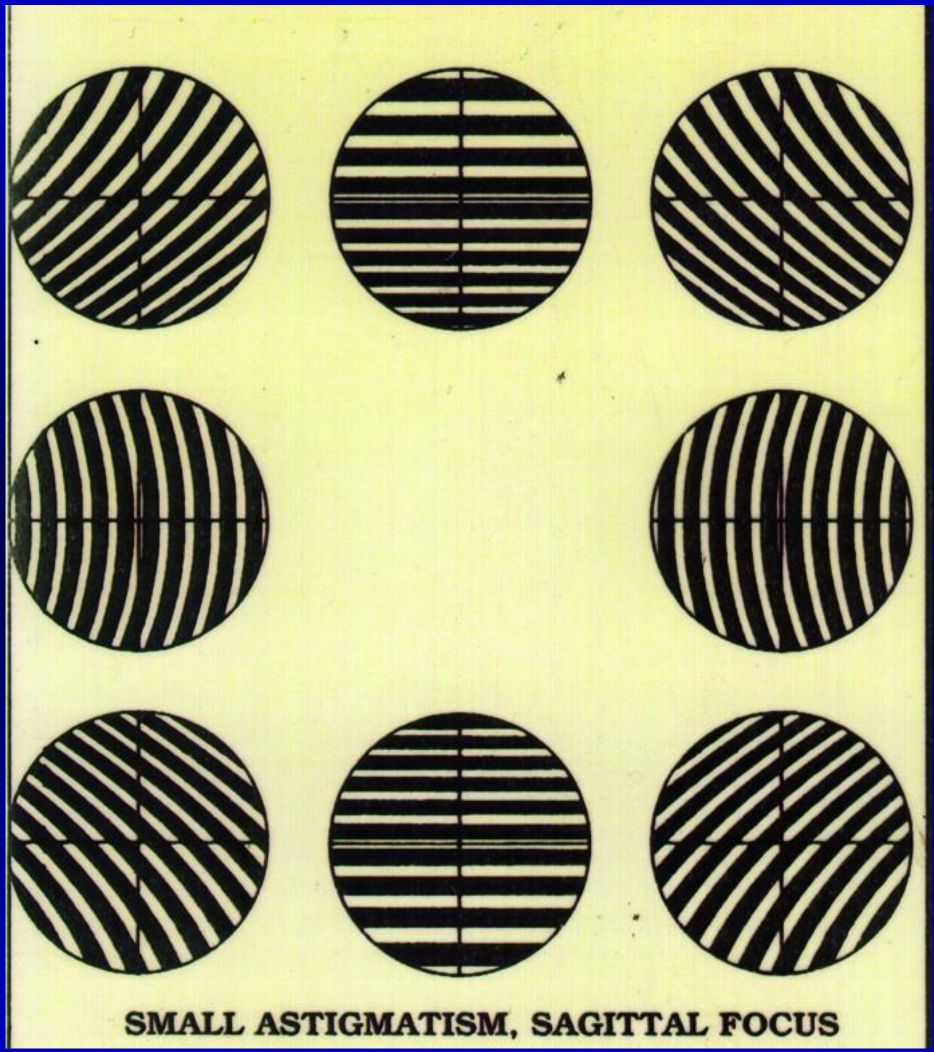

INTERFEROMETRO DE NEWTON VI

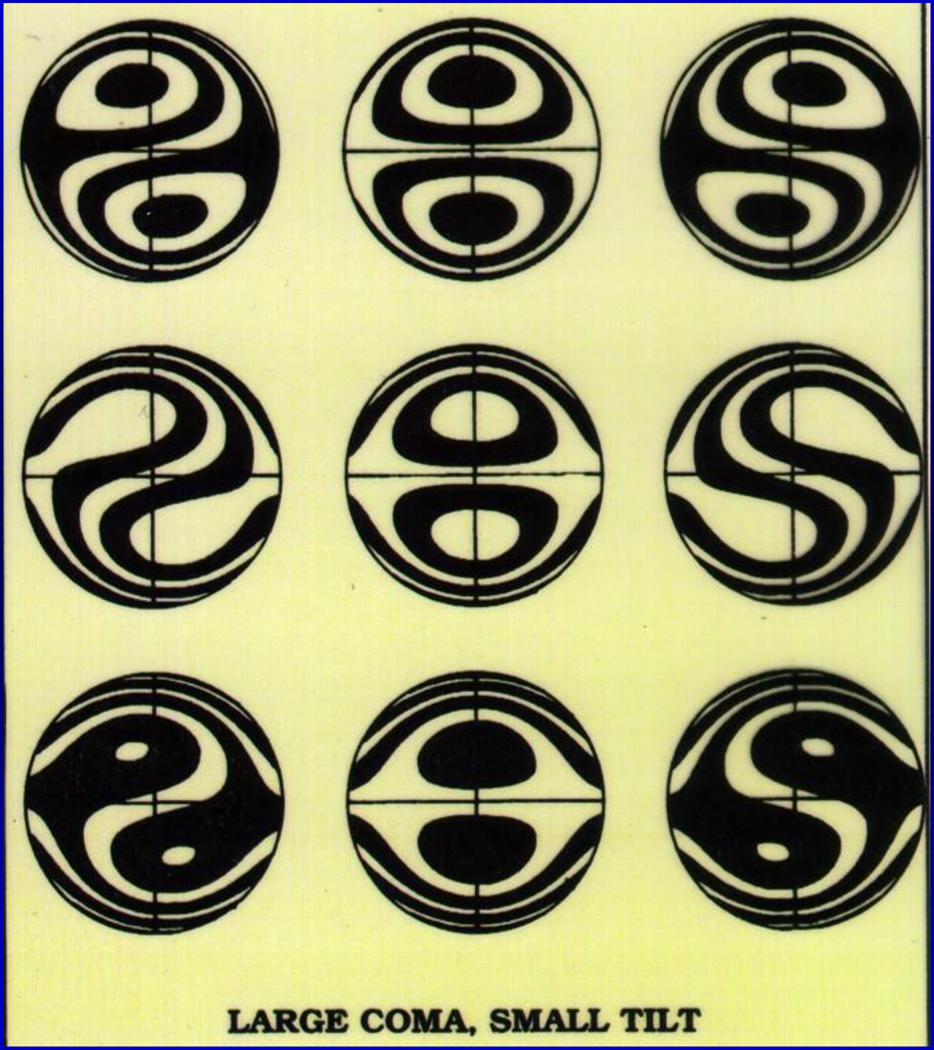

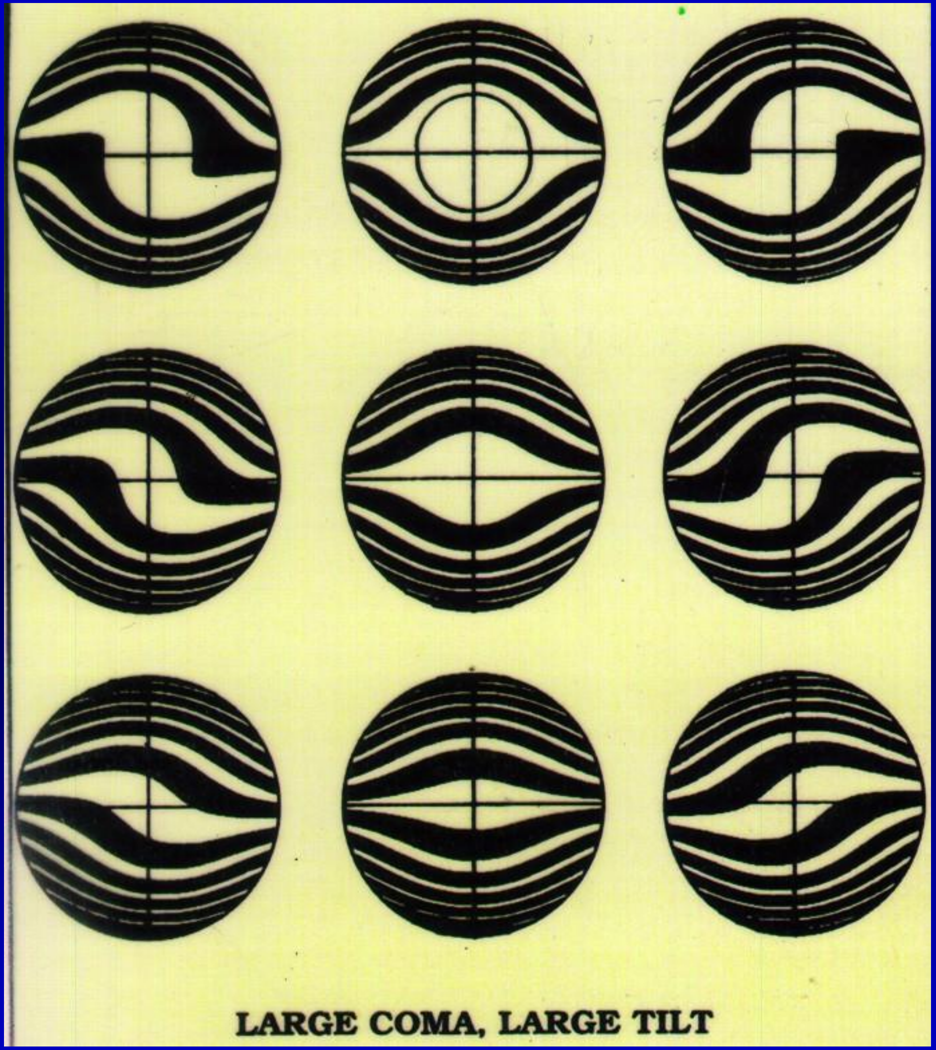

INTERFEROMETRO DE NEWTON VII

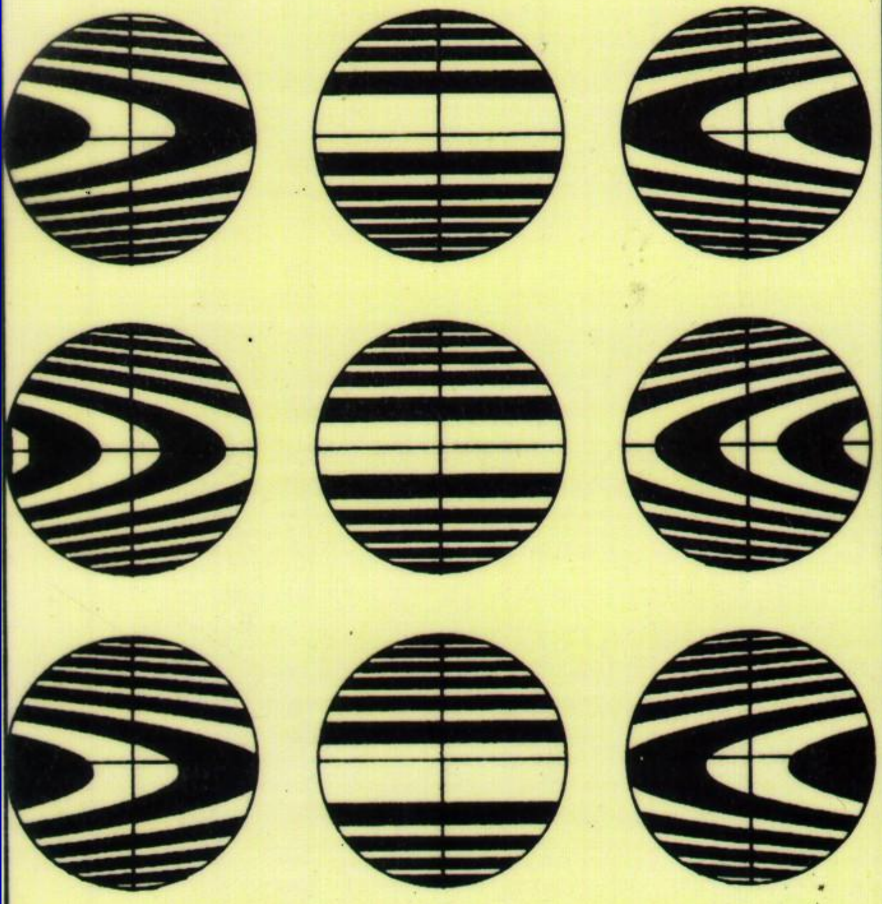

LARGE ASTIGMATISM, SAGITTAL FOCUS, SMALL TILT

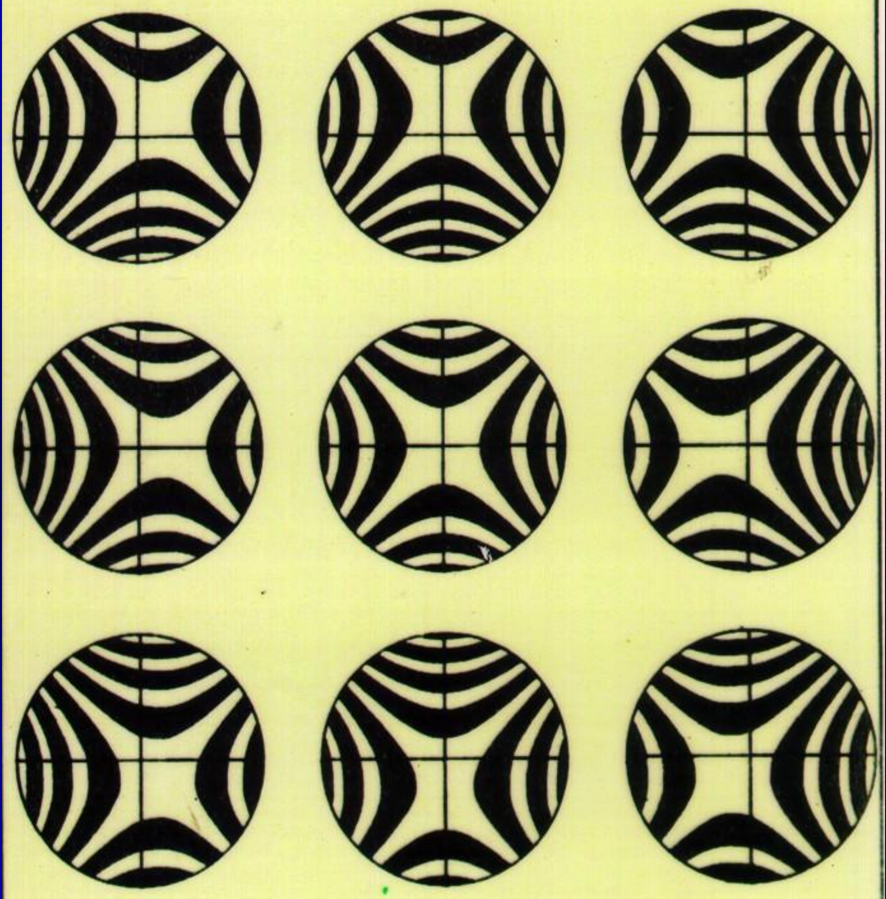

LARGE ASTIGMATISM, MEDIAL FOCUS, SMALL TILT

INTERFEROMETRO DE NEWTON VIII

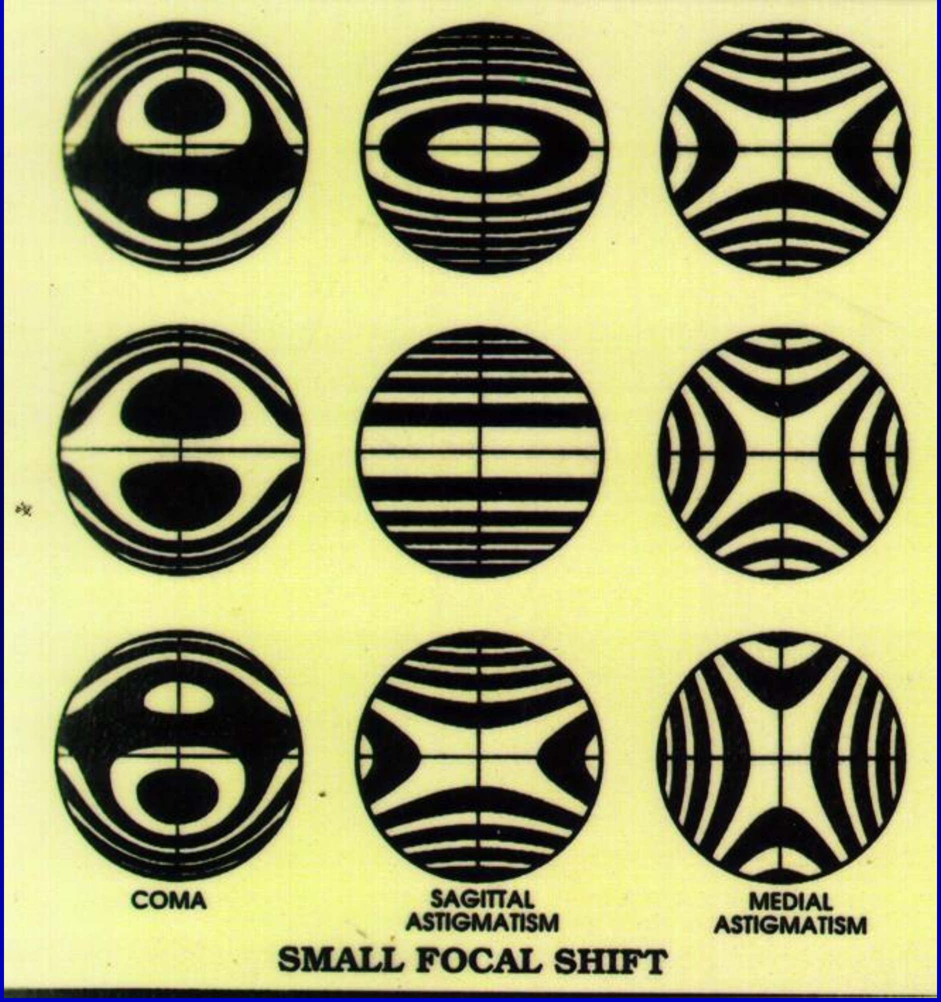

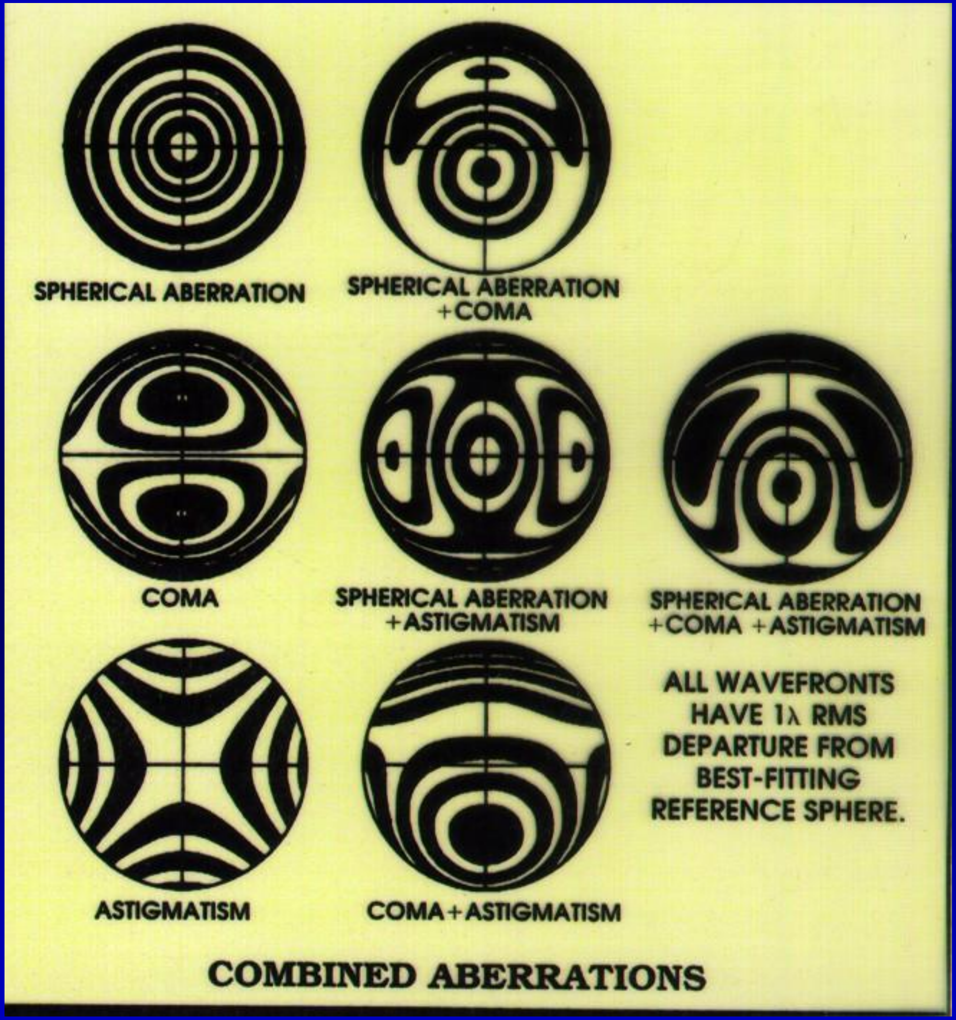

INTERFEROMETRO DE NEWTON IX

Control de calidad de producción de un plano

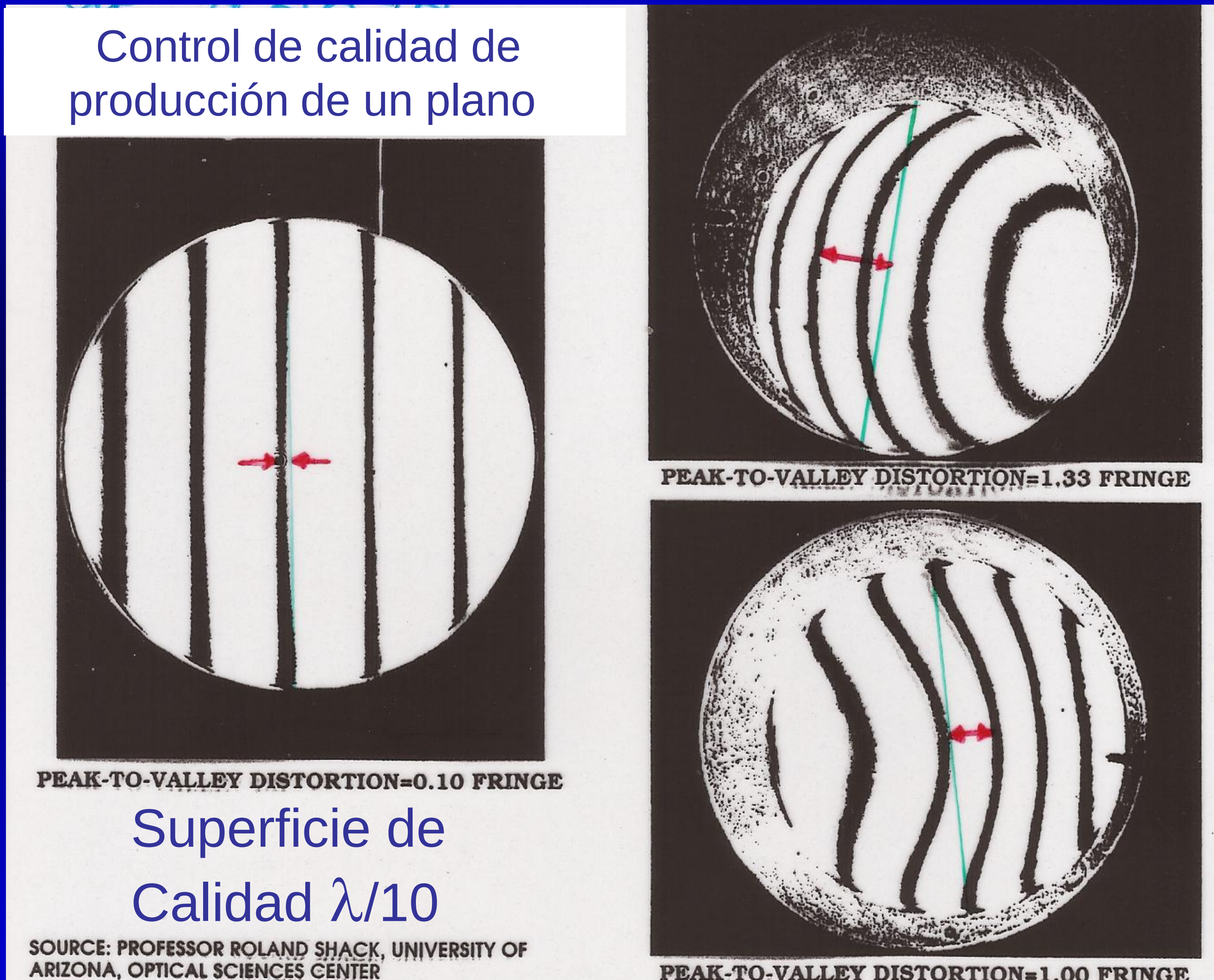

Superficie de Calidad $\lambda/10$

INTERFEROMETRO DE MICHELSON

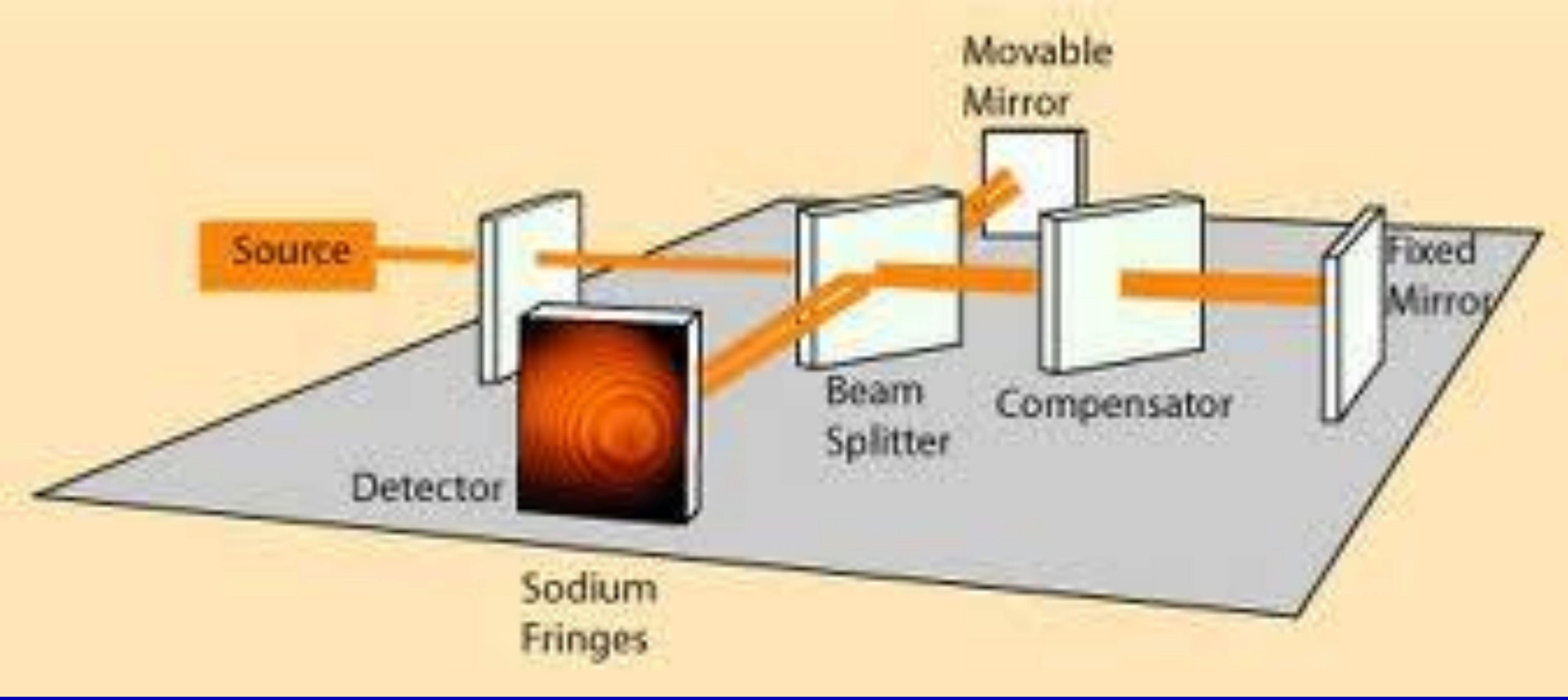

INTERFEROMETRO DE MICHELSON Y OPTICAL COHERENCE TOMOGRAPHY

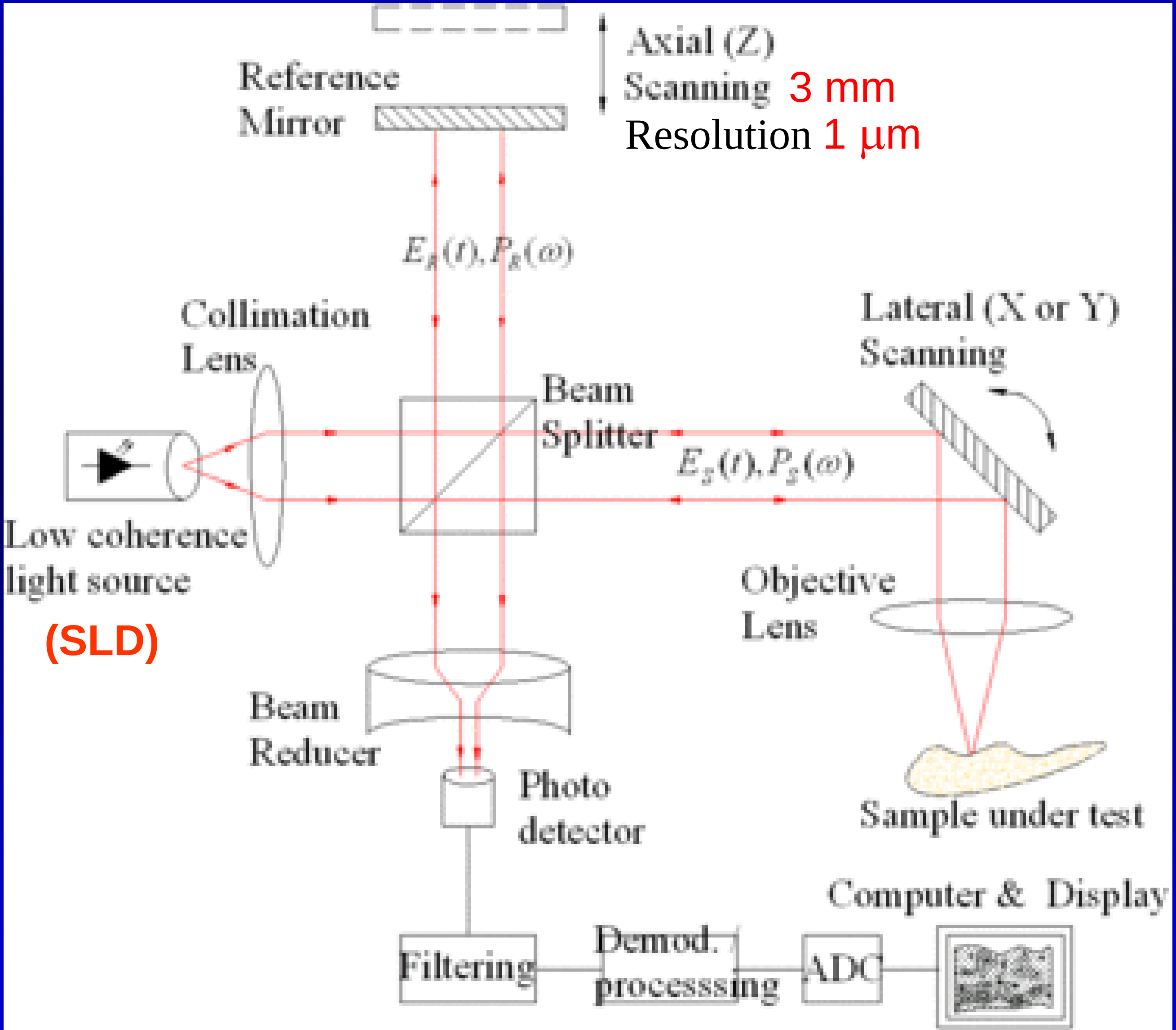

INTERFEROMETRO DE MICHELSON POR FIBRAS OPTICAS Y OPTICAL COHERENCE TOMOGRAPHY

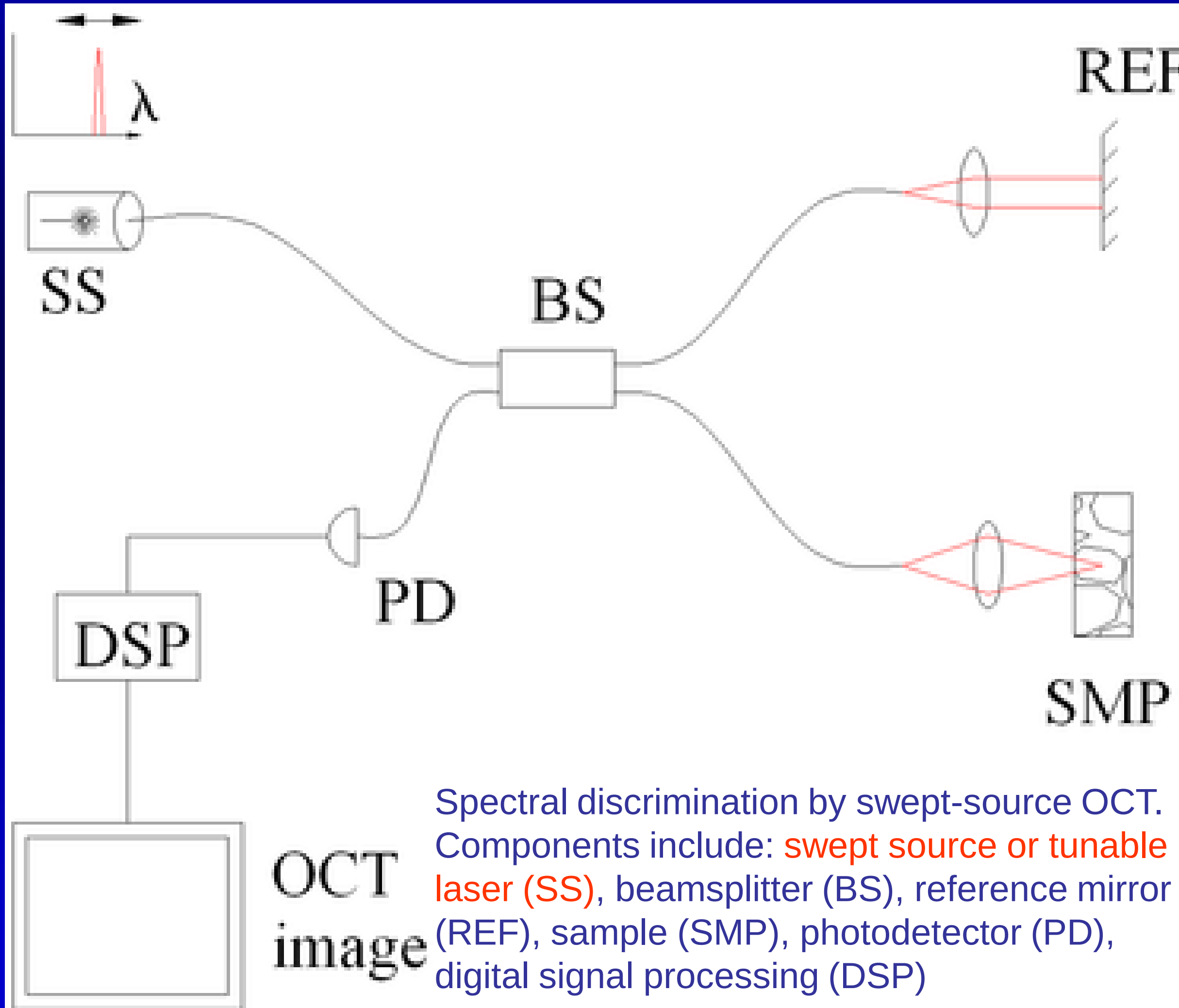

Spectral discrimination by swept-source OCT. Components include: swept source or tunable laser (SS), beamsplitter (BS), reference mirror (REF), sample (SMP), photodetector (PD), digital signal processing (DSP)

IMAGENES POR OCT

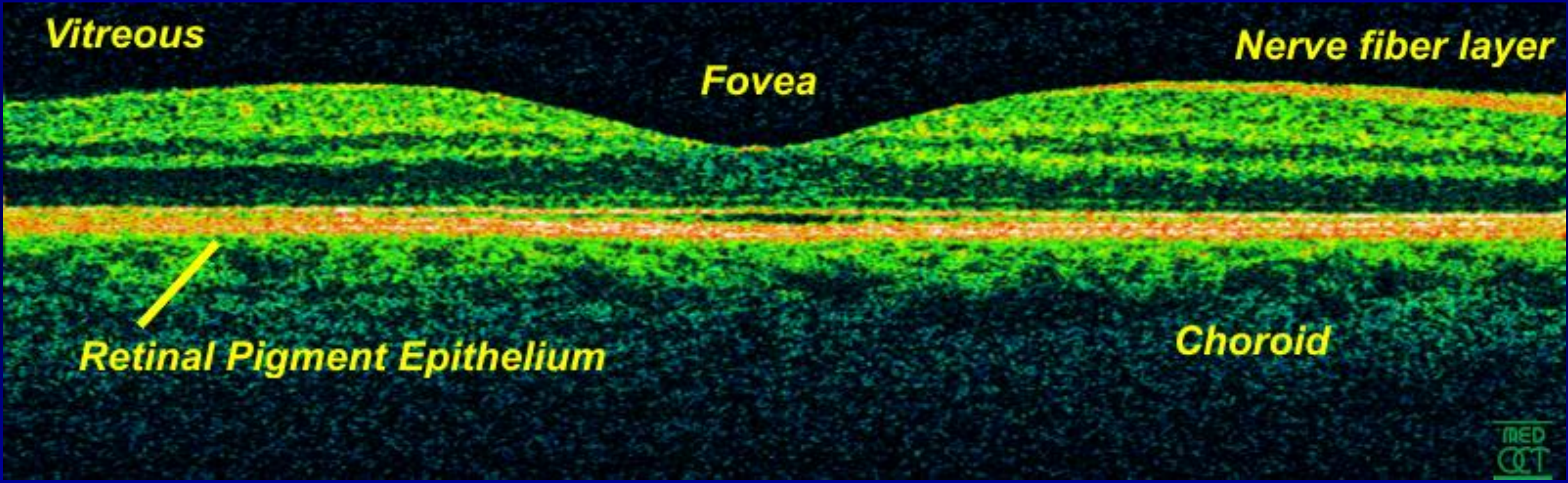

IMAGENES POR OCT I

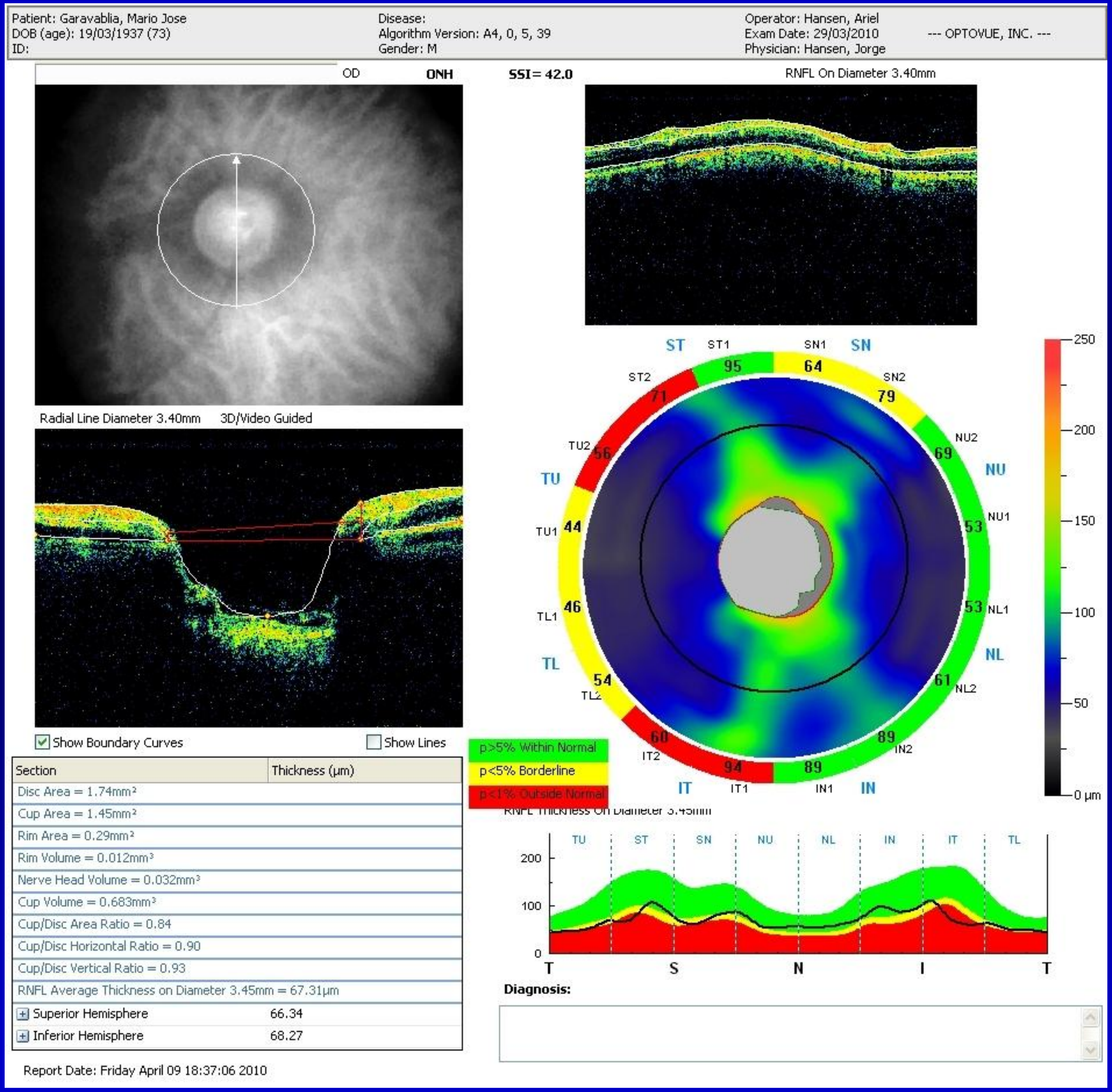

OCT scan of a retina at 800 nm with an axial resolution of 3µm.

IMAGENES POR OCT II

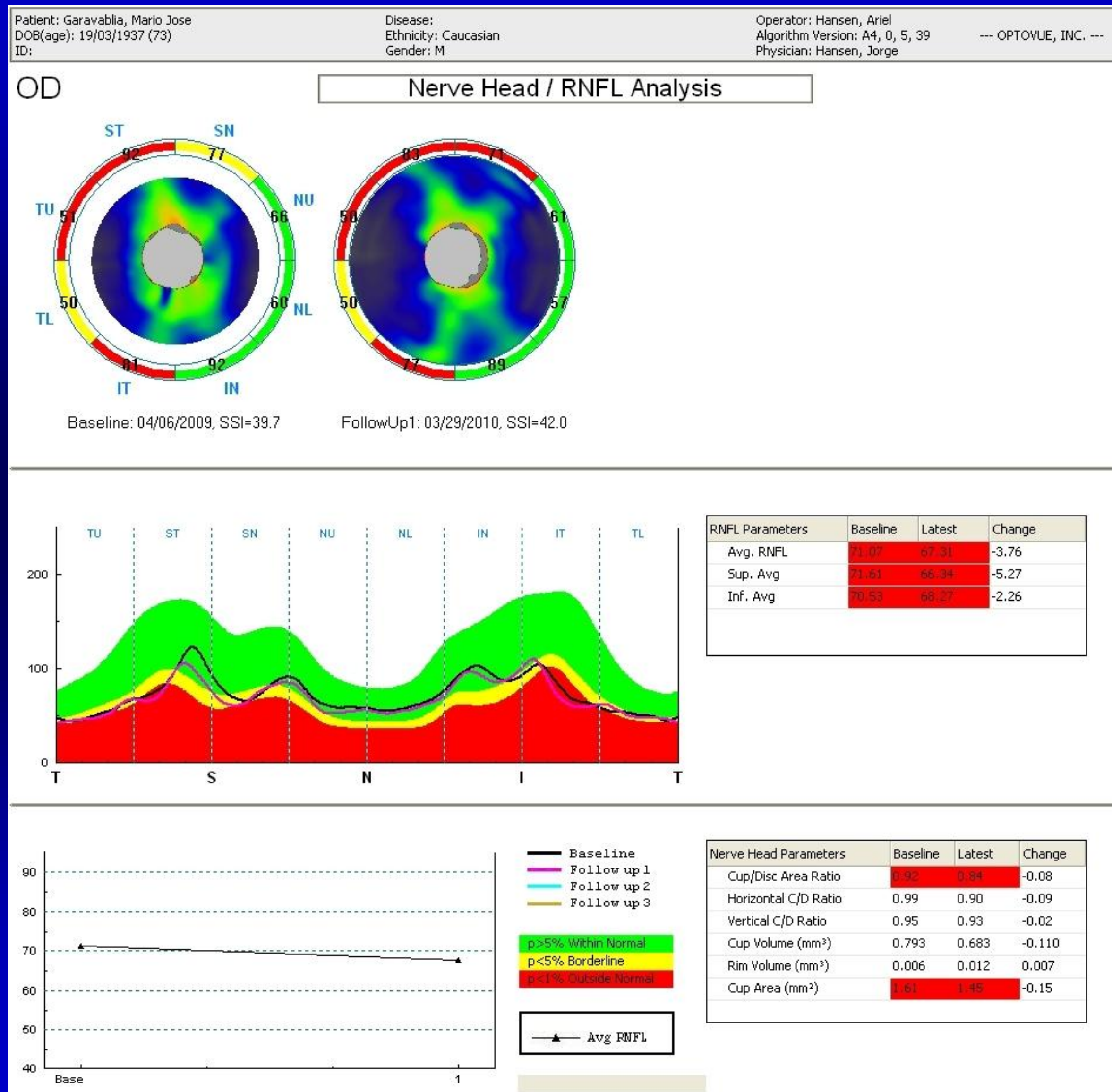

RNFL Parameters	Baseline	Latest	Change
Avg. RNFL	71.07	67.31	-3.76
Sup. Avg	71.61	66.34	-5.27
Inf. Avg	70.53	68.27	-2.26

Nerve Head Parameters	Baseline	Latest	Change
Cup/Disc Area Ratio	0.92	0.84	-0.08
Horizontal C/D Ratio	0.99	0.90	-0.09
Vertical C/D Ratio	0.95	0.93	-0.02
Cup Volume (mm^3)	0.793	0.683	-0.110
Rim Volume (mm^3)	0.006	0.012	0.007
Cup Area (mm^2)	1.61	1.45	-0.15

IMAGENES POR OCT III

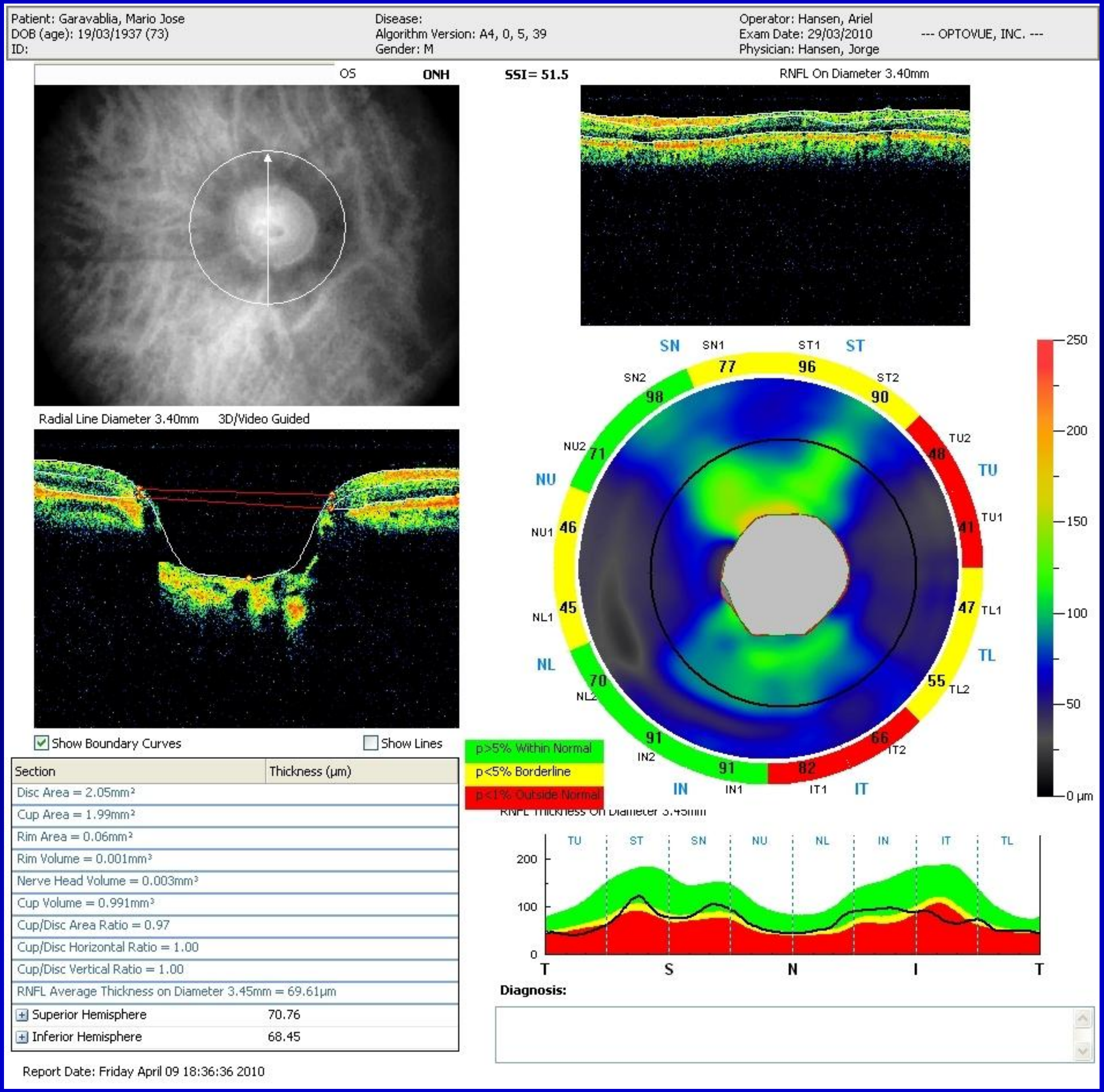

IMAGENES POR OCT IV

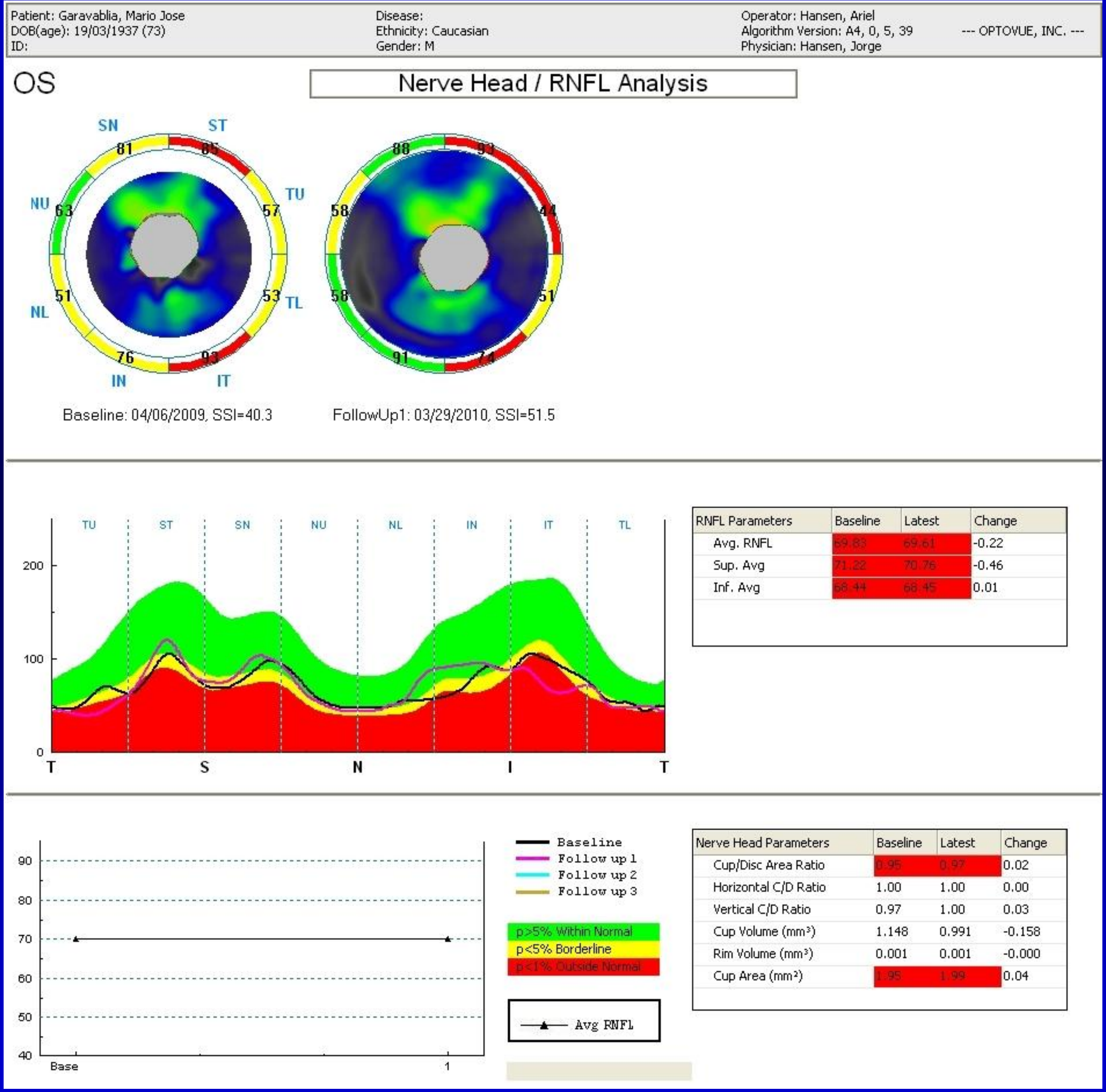

DIFRACCION POR UNA PUPILA CIRCULAR

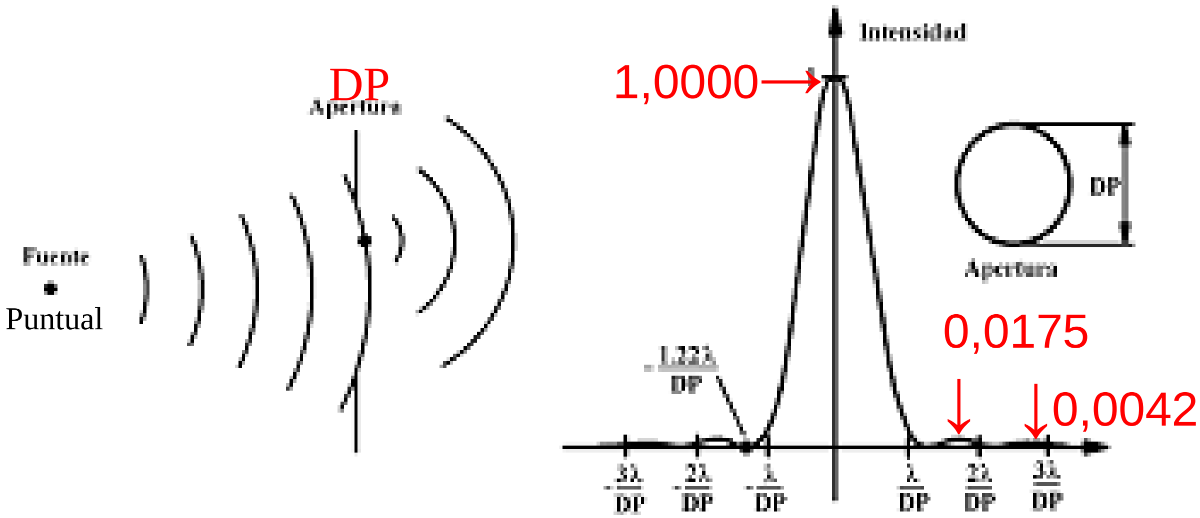

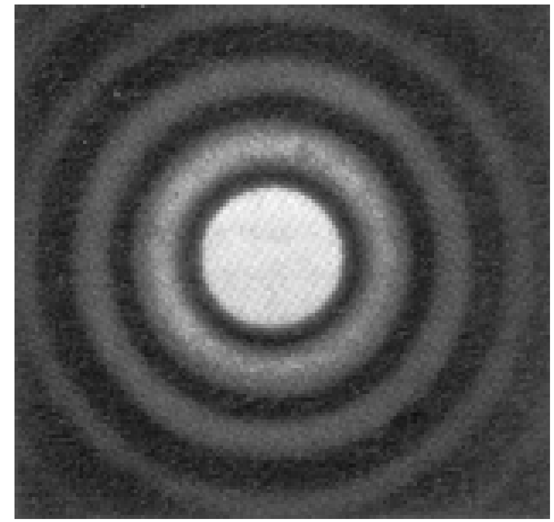

Difracción de la luz en una pupila circular de diametro DP para ángulos de incidencia nulo.

Distribución de Airy o *Point Spread Function* (PSF) o Función de Punto Difractado

The Point Spread Function, or PSF, is the image that an optical system forms of a point source. The point source is the most fundamental object, and forms the basis for any complex object.

The PSF is analogous to the Impulse Response Function in electronics.

$$\theta = \frac{1.22\lambda}{a}$$

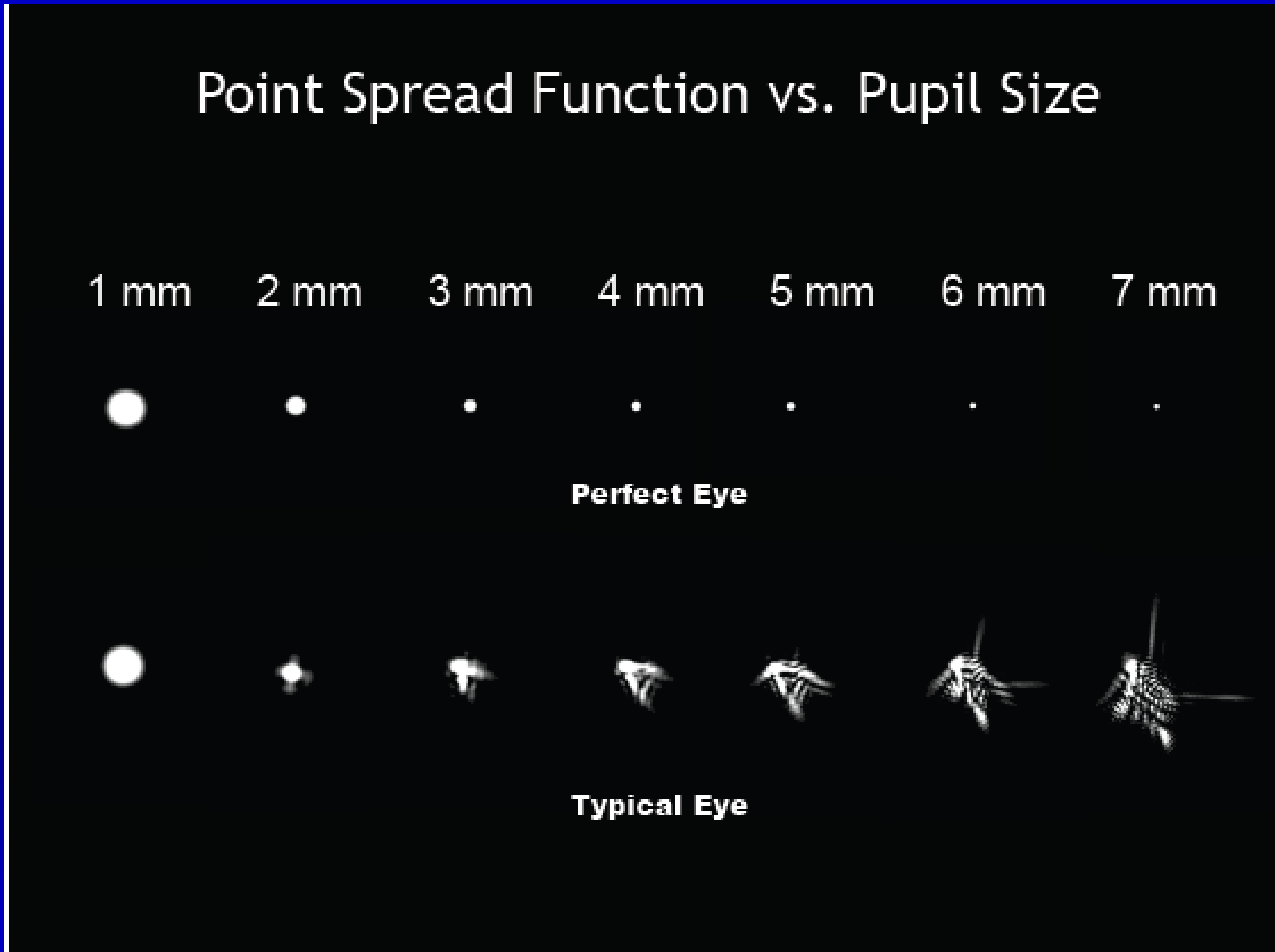
Point Spread Function vs. Pupil Size
1 mm
2 mm
3 mm
4 mm
5 mm
6 mm
7 mm
Perfect Eye
Typical Eye

LENTE CON ABERRACION ESFERICA

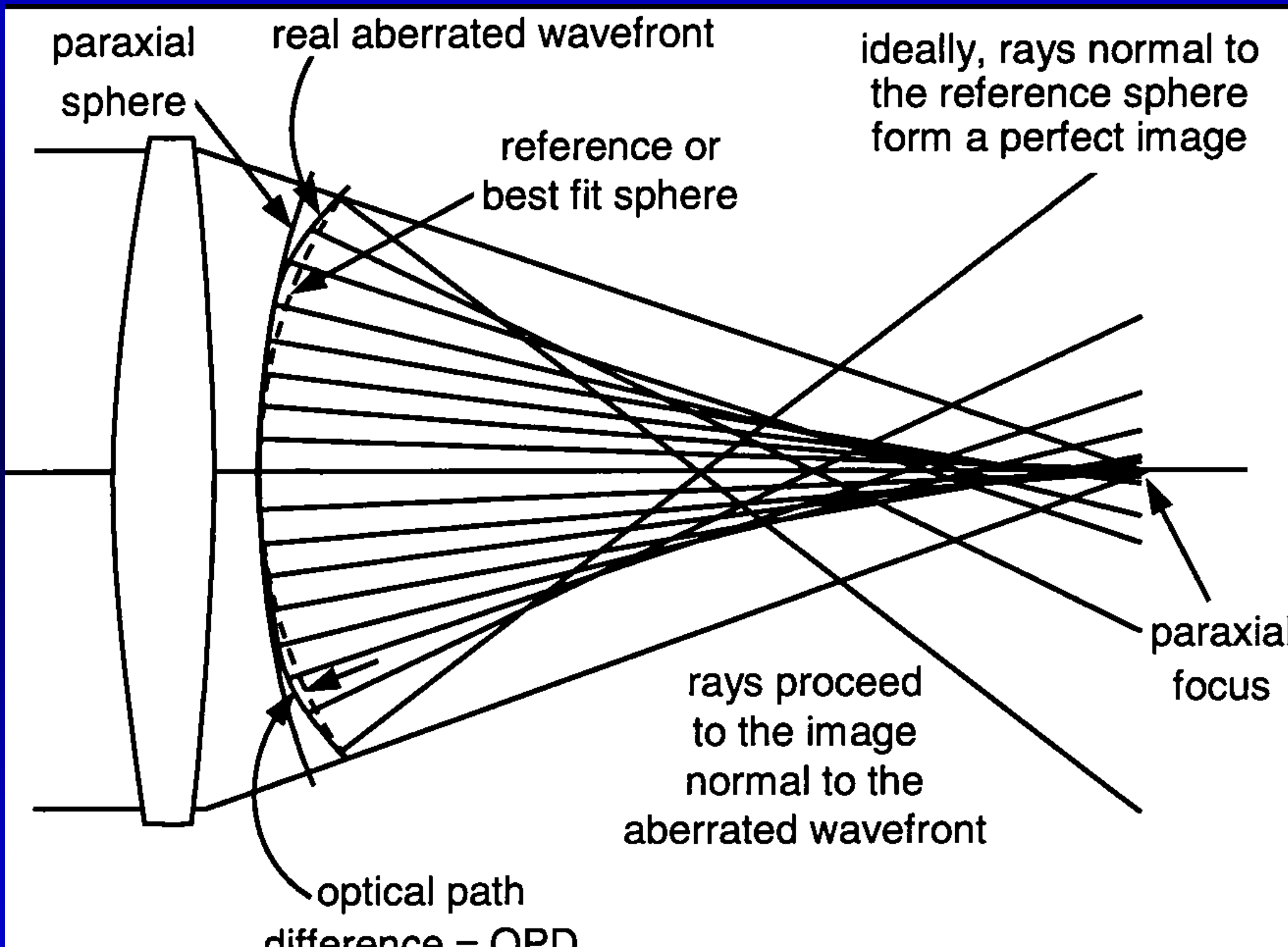

EVALUACIÓN DE LA ABERRACIÓN

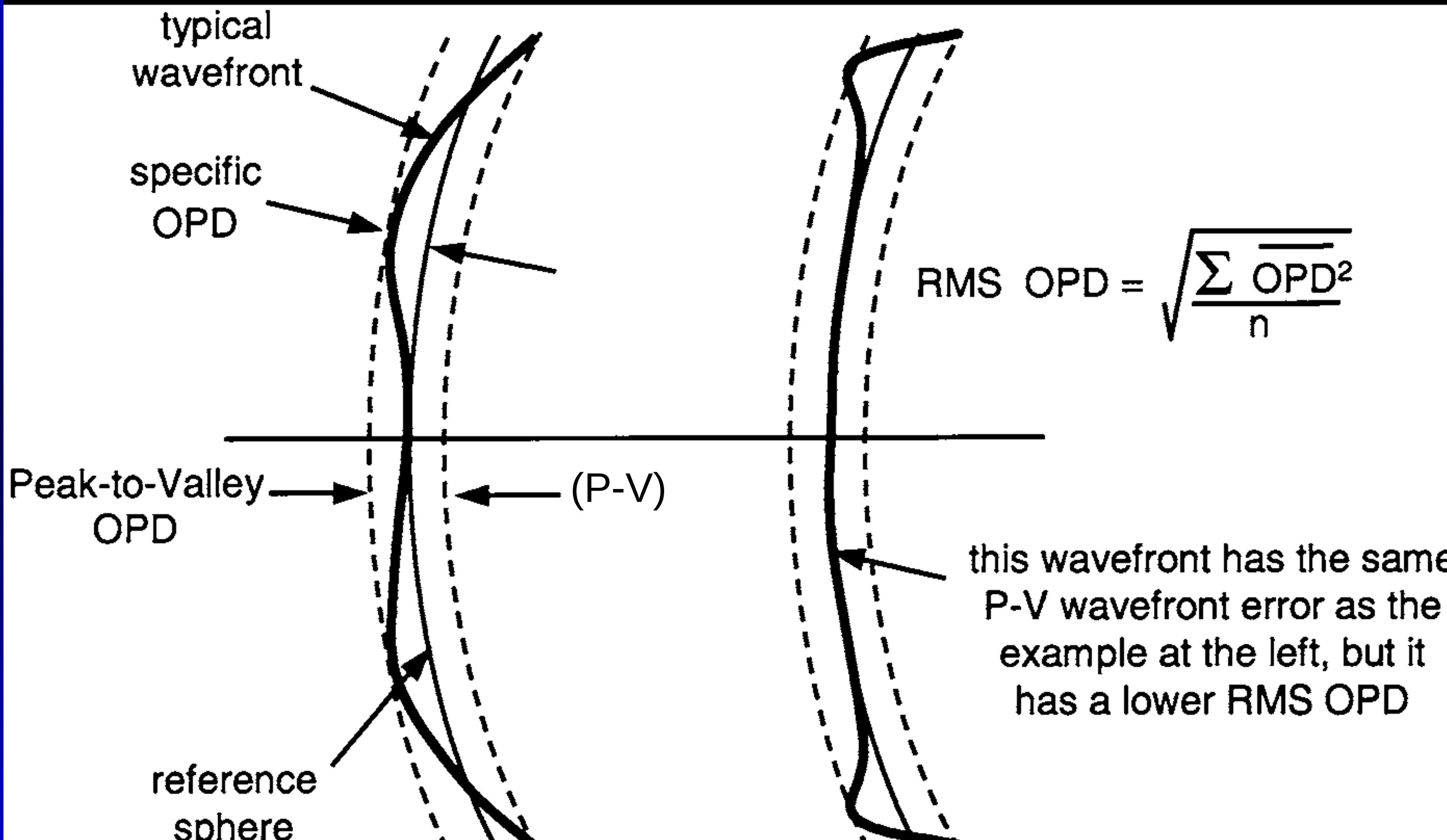

ABERRACION POR CURVATURA DE CAMPO O DE PETZVAL I

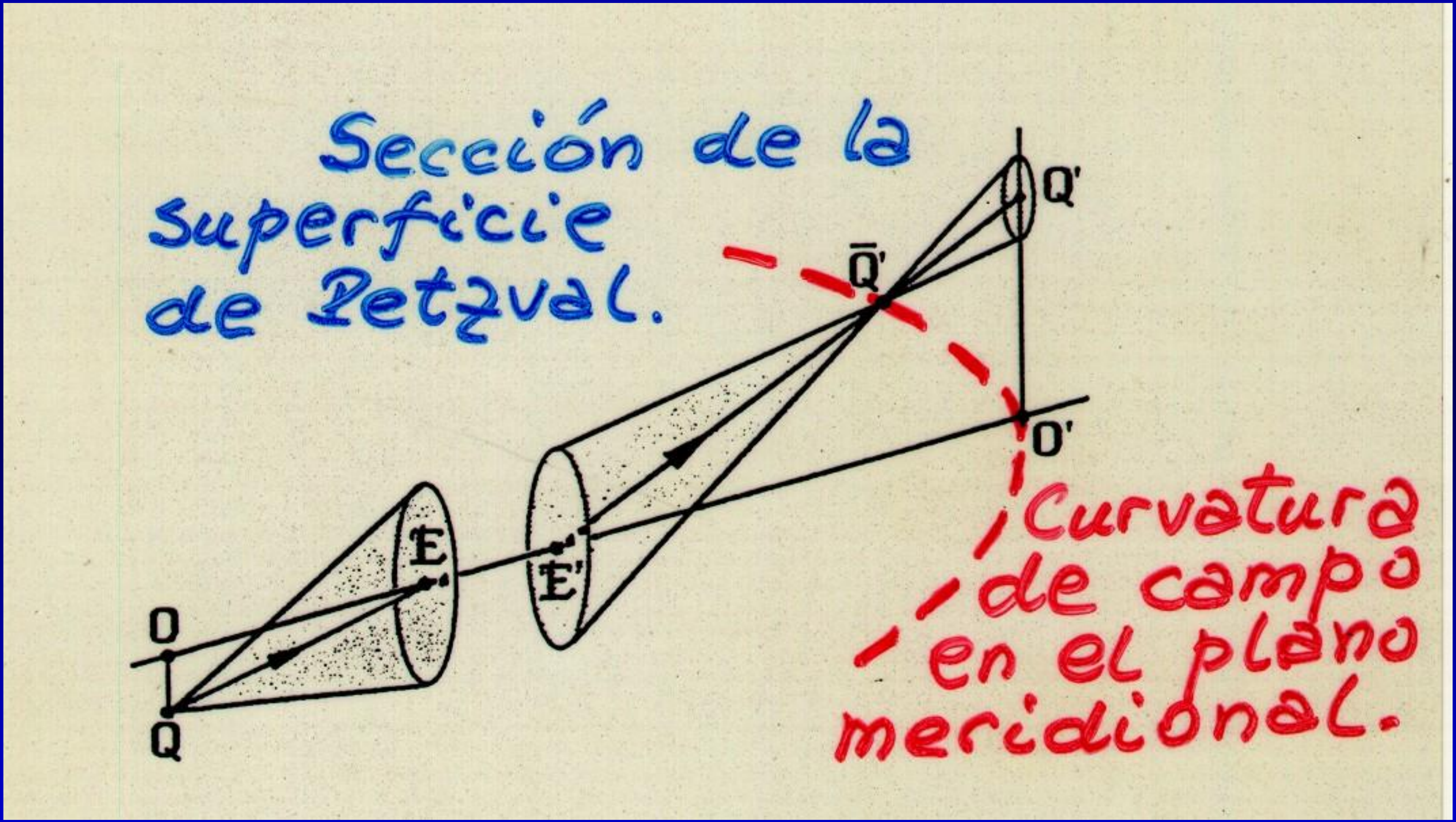

ABERRACION POR CURVATURA DE CAMPO O DE PETZVAL II

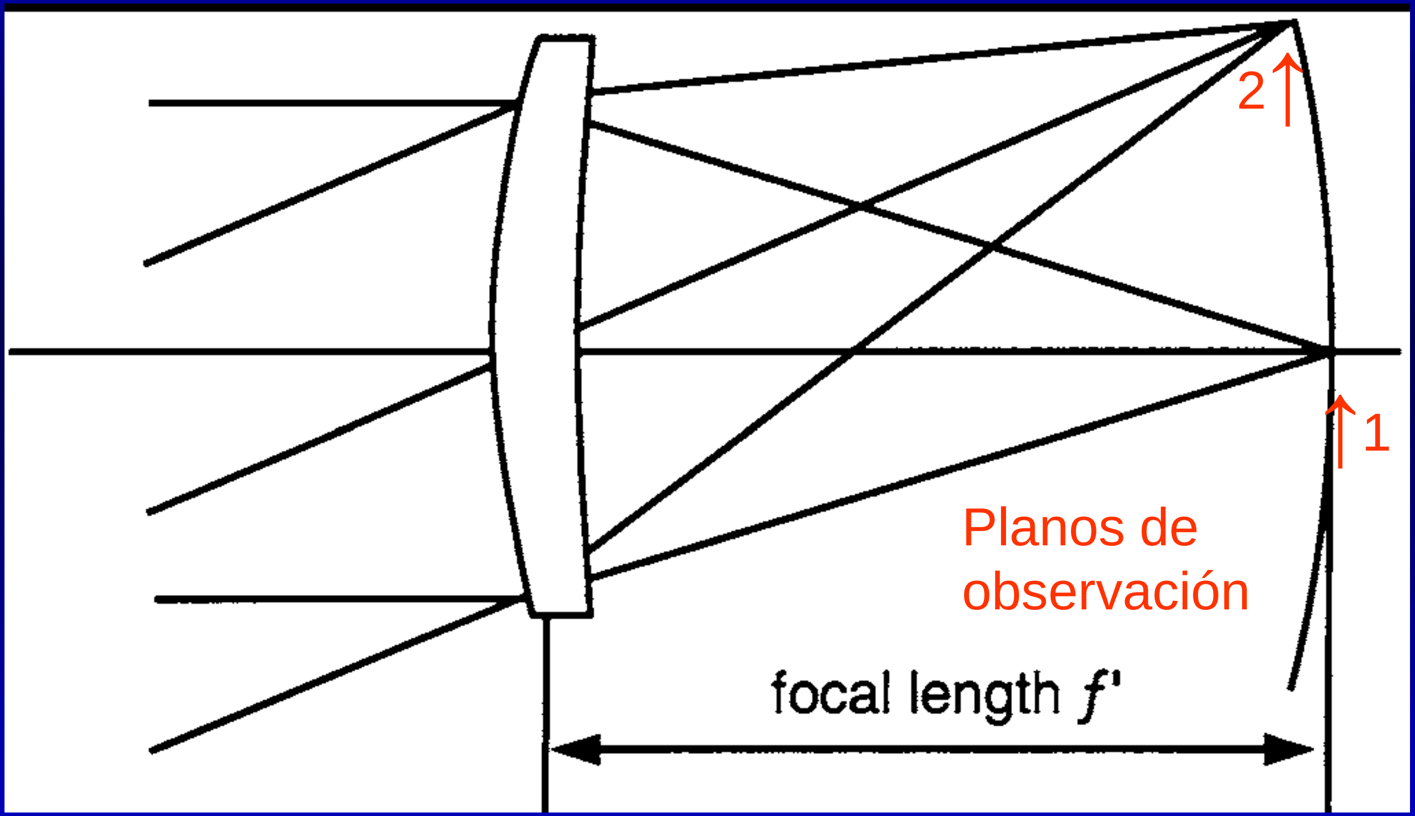

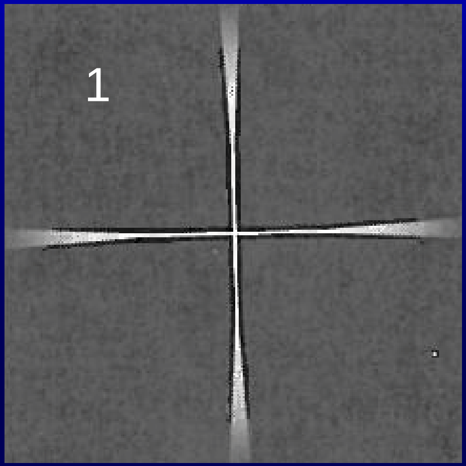

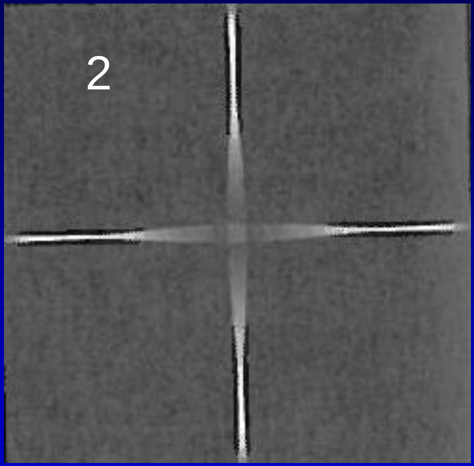

ABERRACION POR DISTORSION

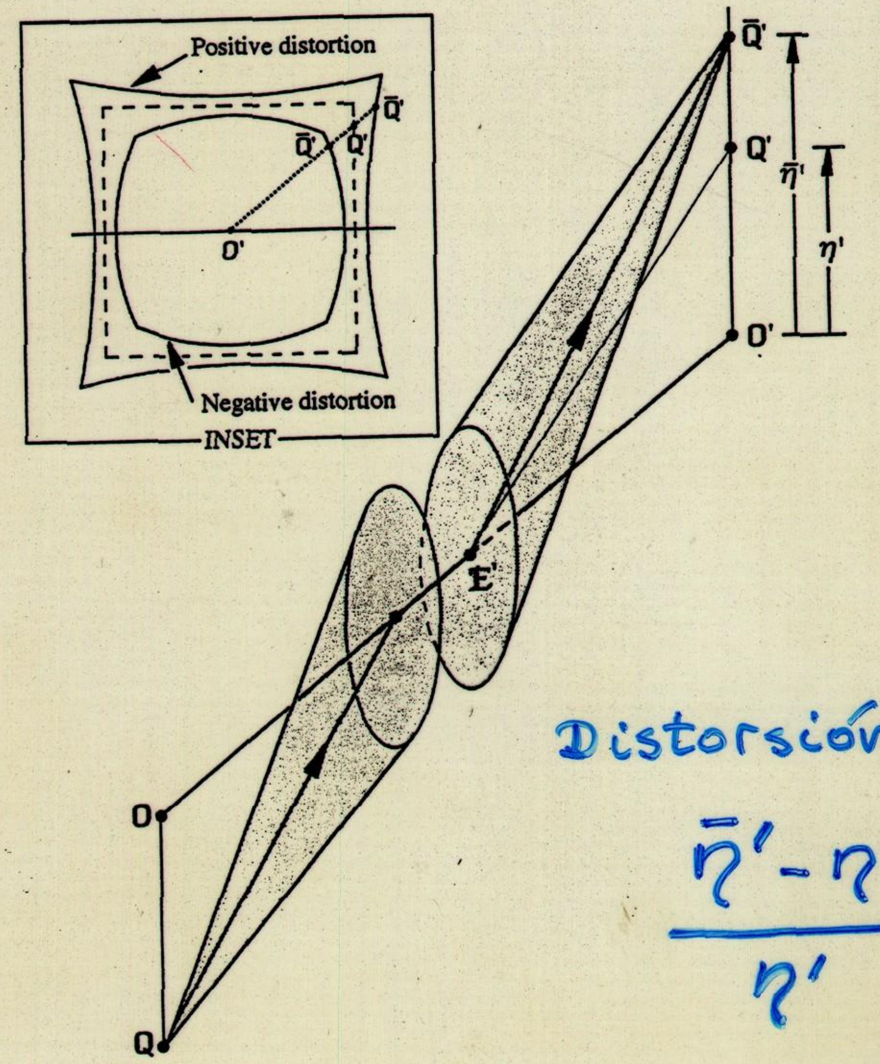

Fig. 5.8: Distortion aberration and, in the inset, the effect of distortion on the image of a square. The dashed line is the Gaussian image of the square.

Distorsión relativa:

$$\frac{\bar{\eta}' - \eta'}{\eta'} \gtrless 0$$

Strehl Ratio

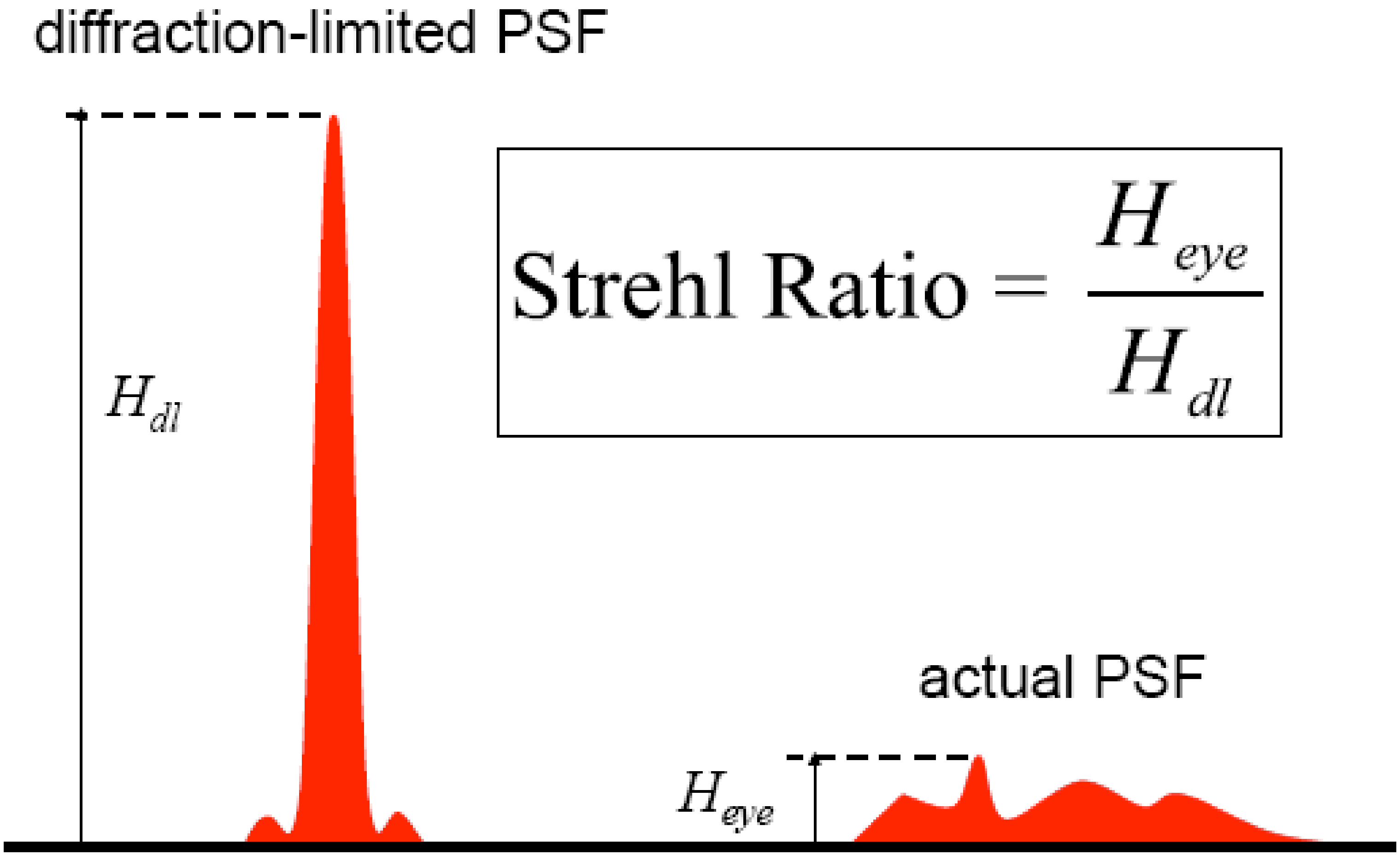

$$\text{Strehl Ratio} = \frac{H_{eye}}{H_{dl}}$$

DIFRACCION POR UNA PUPILA CIRCULAR DE FRENTES DE ONDA ABERRADOS

COCIENTE DE STREHL Ia/Ip
DE IMAGENES PUNTUALES ABERRADAS

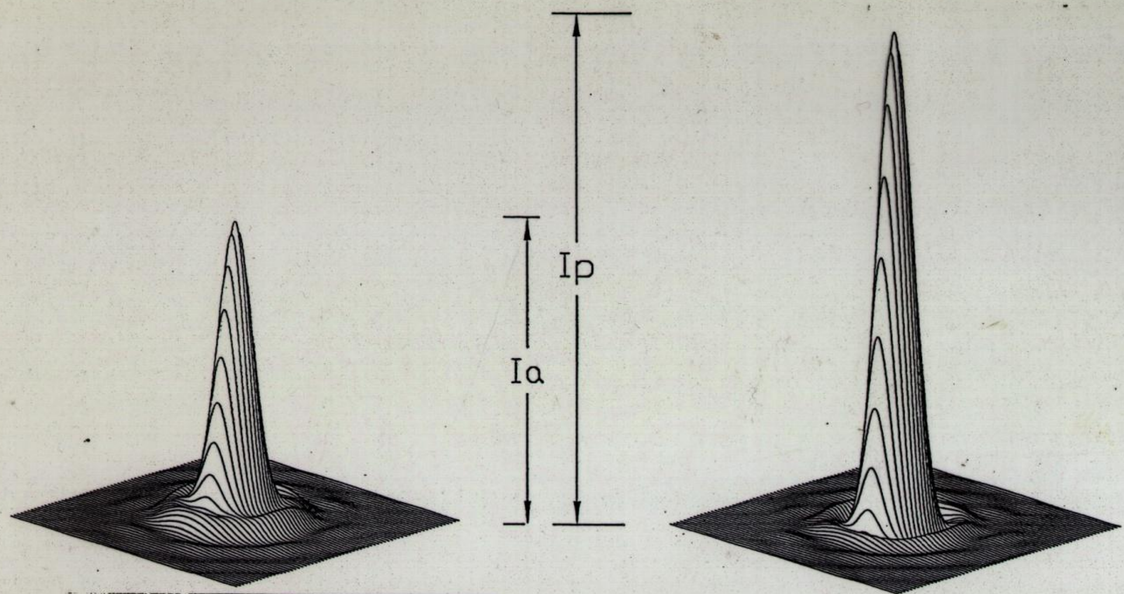

Calidad de imagen	perfecta	excelente	aceptable	pobre
ecm de onda	0	0.05=1/20	0.07=1/14	0.10=1/10
cociente de Strehl	100%	90%	80%	60%

Karl Strehl, Z.f. Instrumkde., 22, 213, 1902.

Cuando el Cociente de Strehl supera el 80 % el sistema óptico cumple con el **Criterio de Marechal**. Si supera el 90% se indica que es **Superresolvente**.

ecm: Error Cuadrático Medio

CALIDAD DEL FRENTE DE ONDA

La aberración del frente de onda disminuye el poder resolvente de todo sistema óptico, incluso de nuestros ojos.

El poder resolvente guarda relación con la **Agudeza Visual**.

Cociente de Strehl: 25%

(¡Pésimo!)

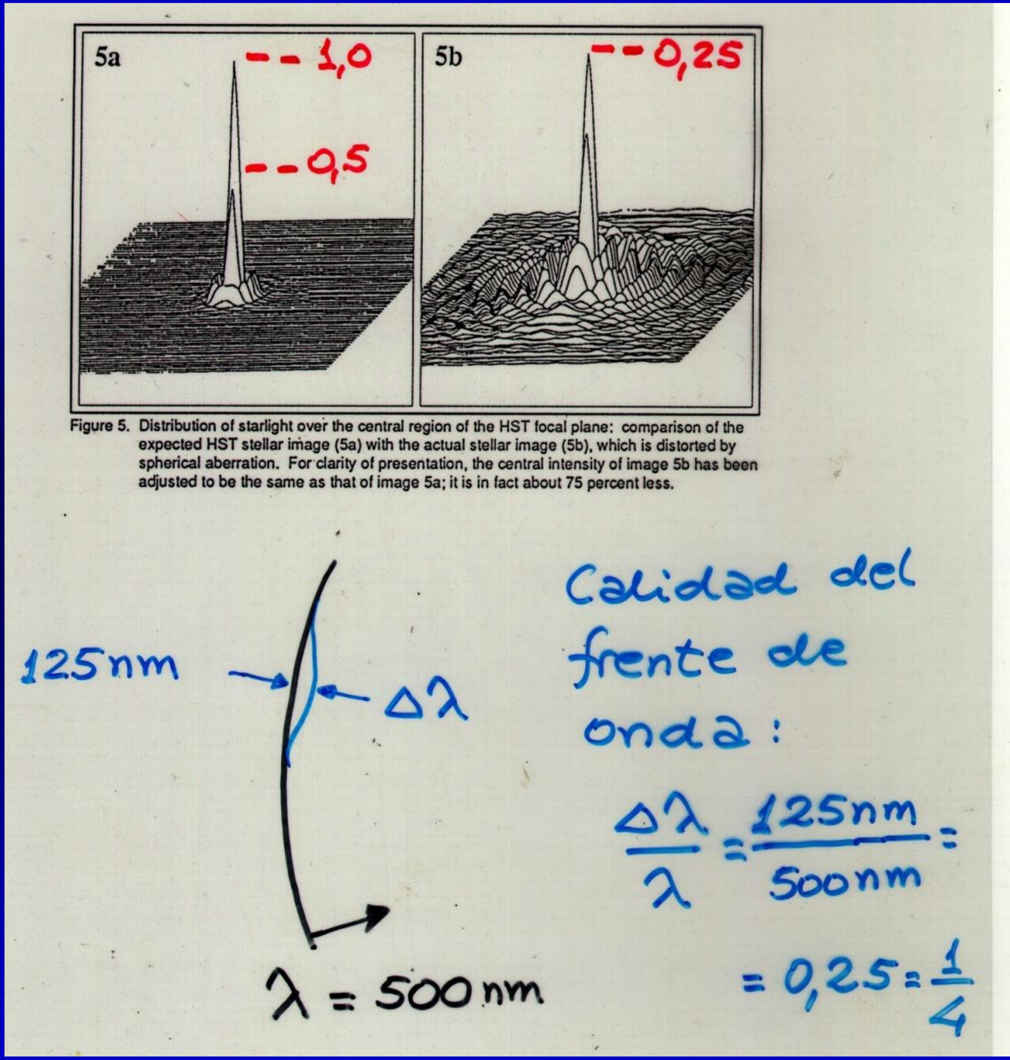

FACTORES QUE AFECTAN EL COMPORTAMIENTO DE LOS OJOS

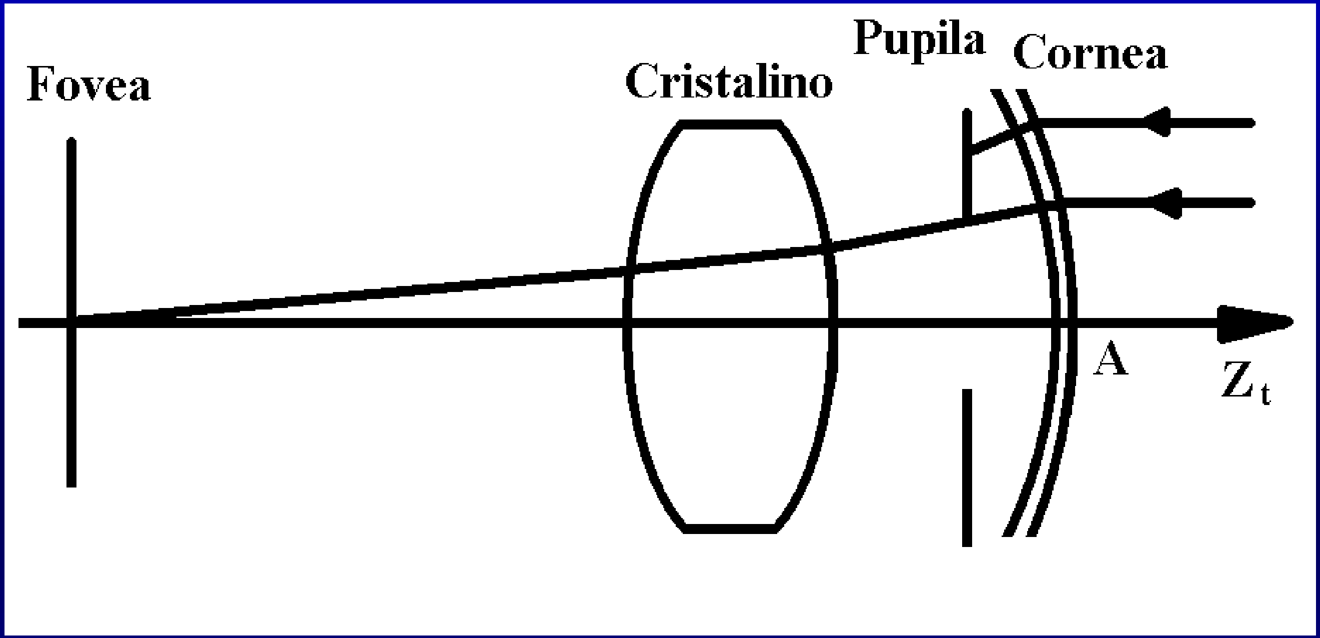

- Curvaturas, centrado, tamaños, distancias relativas e índices de refracción de las componentes (hipermetropía, miopía, astigmatismo y aberraciones de orden superior)
- Transparencia u opacidad de los medios (cataratas)

ANALISIS DE LAS ABERRACIONES I

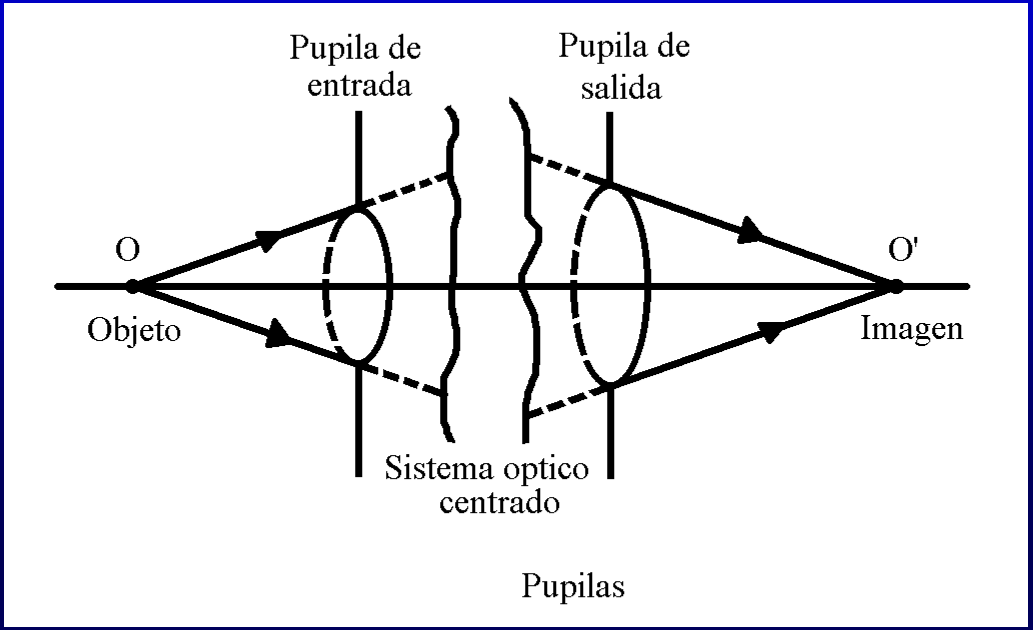

En la región paraxial la imagen de un punto es un punto, es decir, un frente de ondas esférico a la entrada origina un frente de ondas esférico a la salida (Optica de Gauss).

Fuera de la región paraxial aparecen aberraciones que afectan la imagen, la que en vez de un punto es una mancha (Optica de von Seidel).

Pupila de entrada: imagen del diafragma de apertura en el espacio objeto

Pupila de salida: imagen del diafragma de apertura en el espacio imagen

Ellas limitan el haz que atraviesa el sistema controlando las aberraciones.

DETERMINACION DE LAS ABERRACIONES TOTALES

Aberrómetros más usados en la actualidad:

- **Laser Ray Tracing (LRT):** evaluación secuencial para cada punto de la pupila
- **Sensor Hartmann-Shack (H-S):** evaluación simultánea para toda la pupila

DETERMINACION DE ABERRACIONES POR **L**ASER **R**AY **T**RACING (LRT)

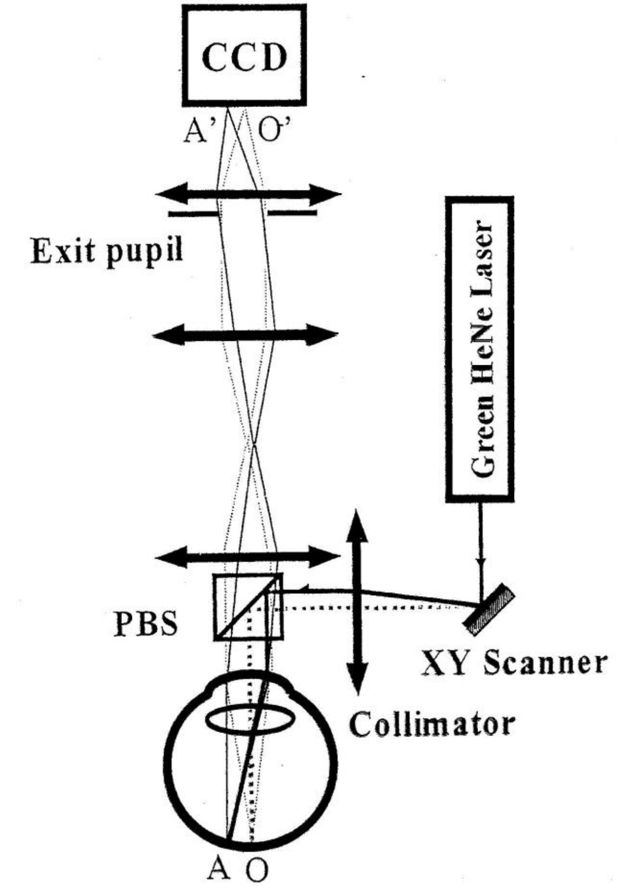

Fig. 1. LRT method: A narrow laser pencil is deflected by a computer-controlled two-dimensional laser scanner. The beam, after passing through a beam splitter and a given point at the pupil plane, forms a small spot of light at the retina. The position offset, AO, between this spot and that formed by the chief ray is the aberration of that ray. A CCD camera records the image of each spot to compute its centroid. PBS, polarization beam splitter.

LRT Y CALCULO DEL FRENTE DE ONDA ABERRADO

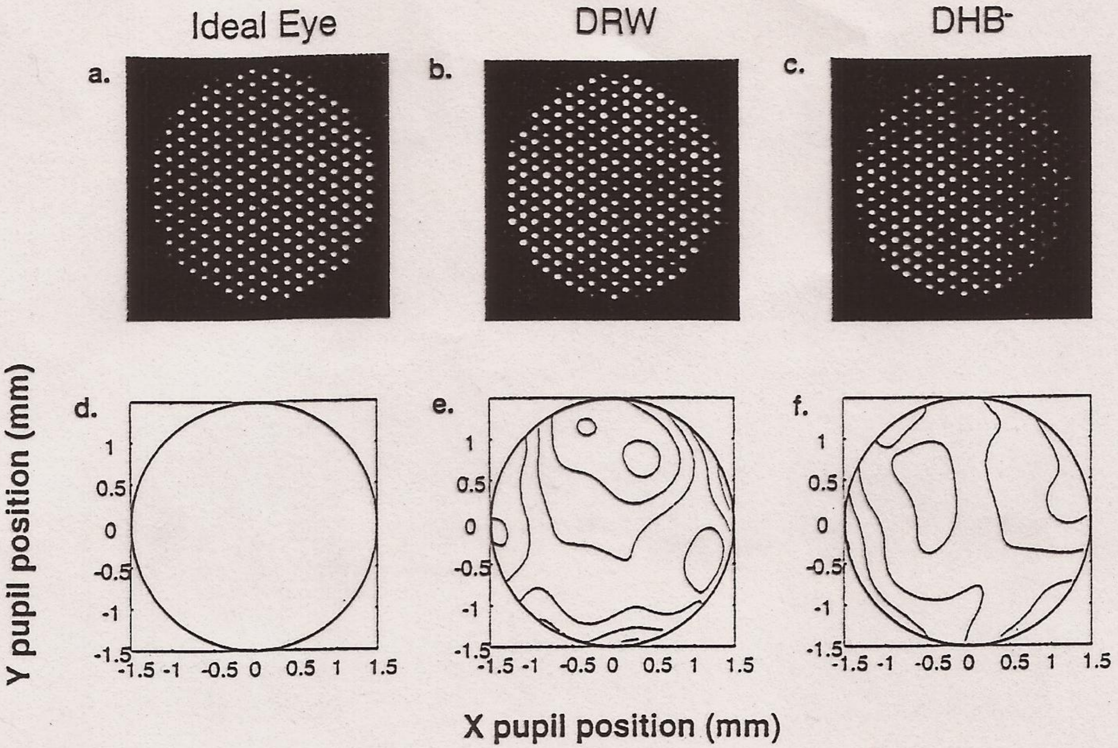

Fig. 2. Wave-front-sensor images and wave aberration of eyes for a small 3-mm pupil. a. The image from the wave-front sensor for an ideal eye on the left, which corresponds to no phase error across the pupil, as shown in the wave aberration on the right. b. and c. show the wave-front-sensor images for two real eyes along with the calculated wave aberration. The contour interval in the wave-aberration plots (d.–f.) is 0.15 μm. The pupil was sampled with a center-to-center spacing of 0.2 mm.

RESULTADOS DEL TEST DE **LRT** Y DE LOS CALCULOS DE LA ABERRACION DEL FRENTE DE ONDA Y SU CUANTIFICACION

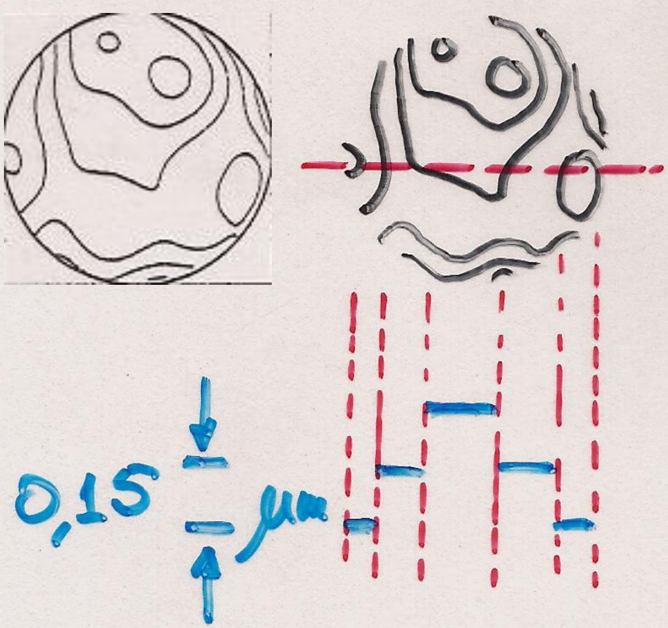

Intervalo entre los contornos equivale a una aberración del frente de onda de 0,15 µm.

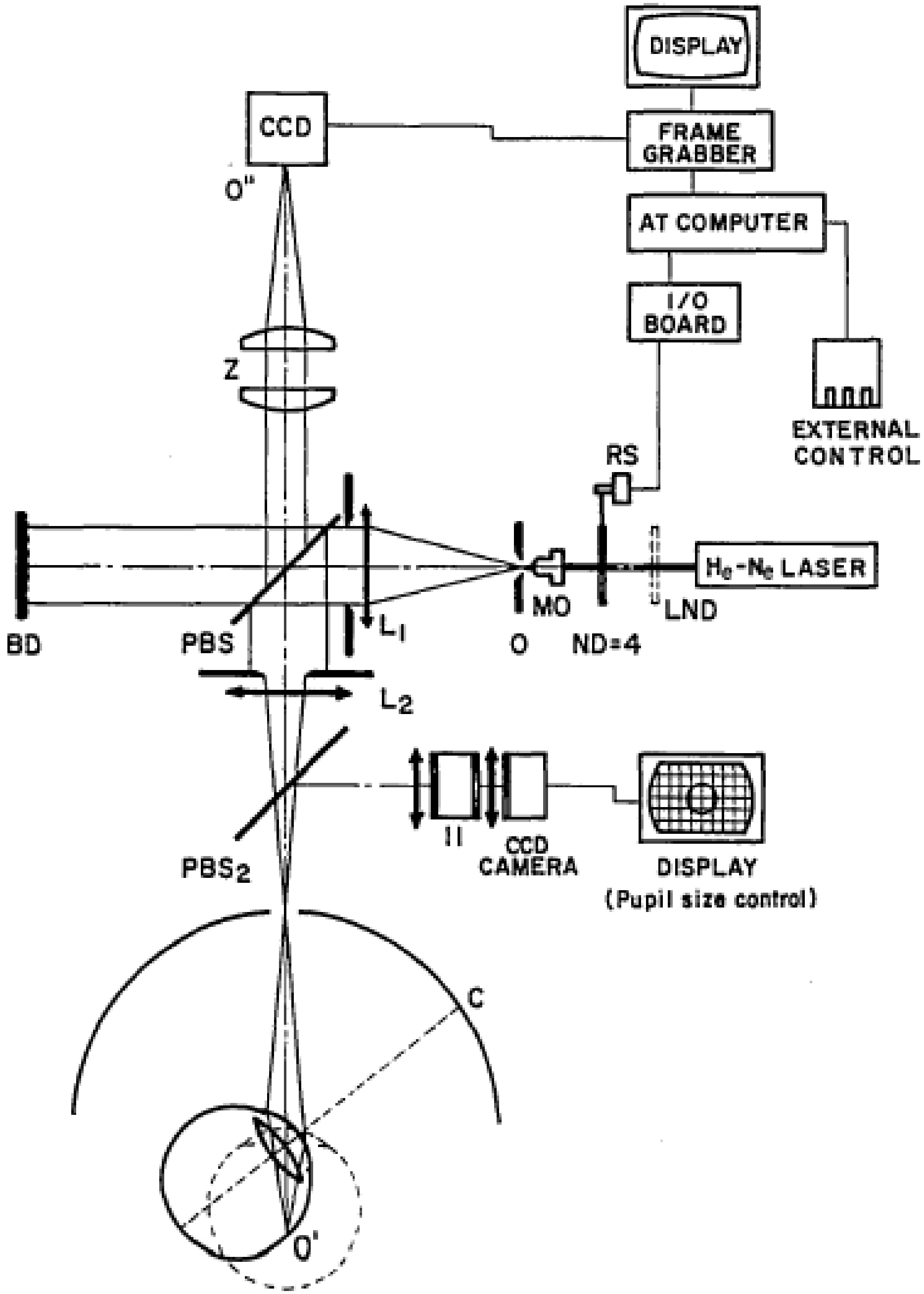

Fig. 1. Experimental setup for recording and digital processing of the double-pass aerial image of a point source (see text for a detailed description).

OBSERVACION DIRECTA DE LA PSF RETINIANA EN FUNCION DEL ANGULO DE INCIDENCIA

PSF OBSERVADAS I

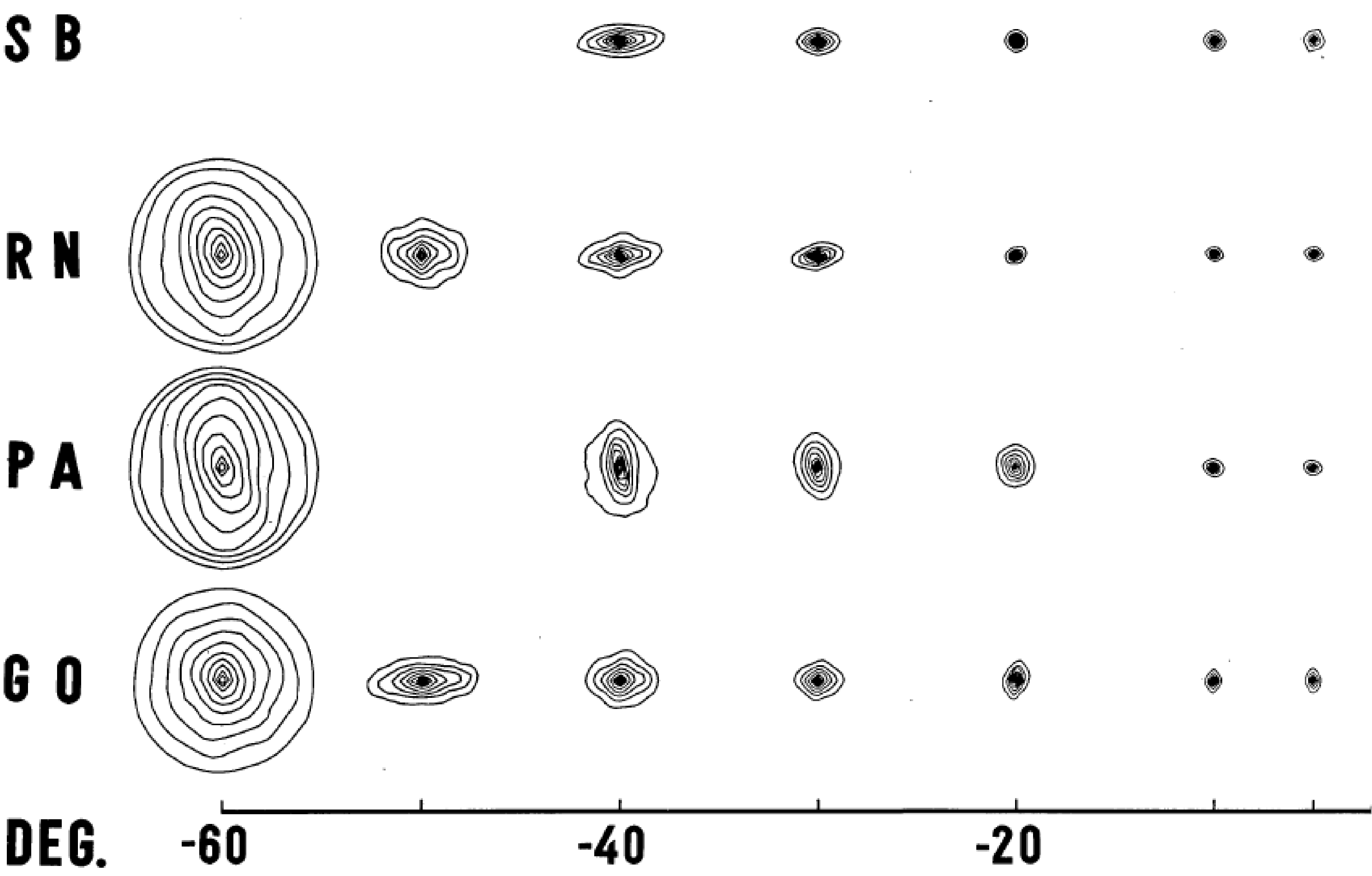

PSF OBSERVADAS II

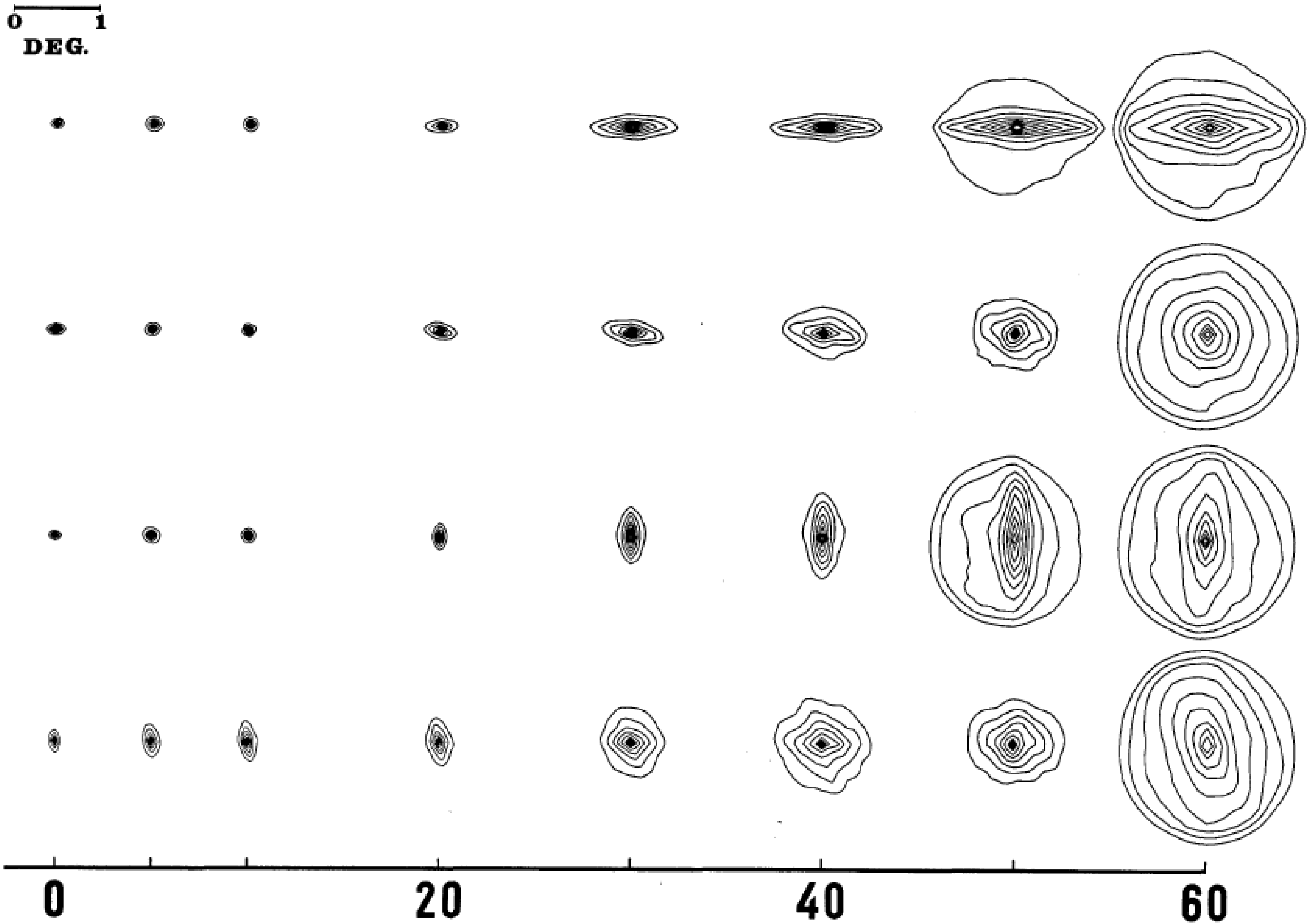

PSF DE JOVENES Y DE VIEJOS

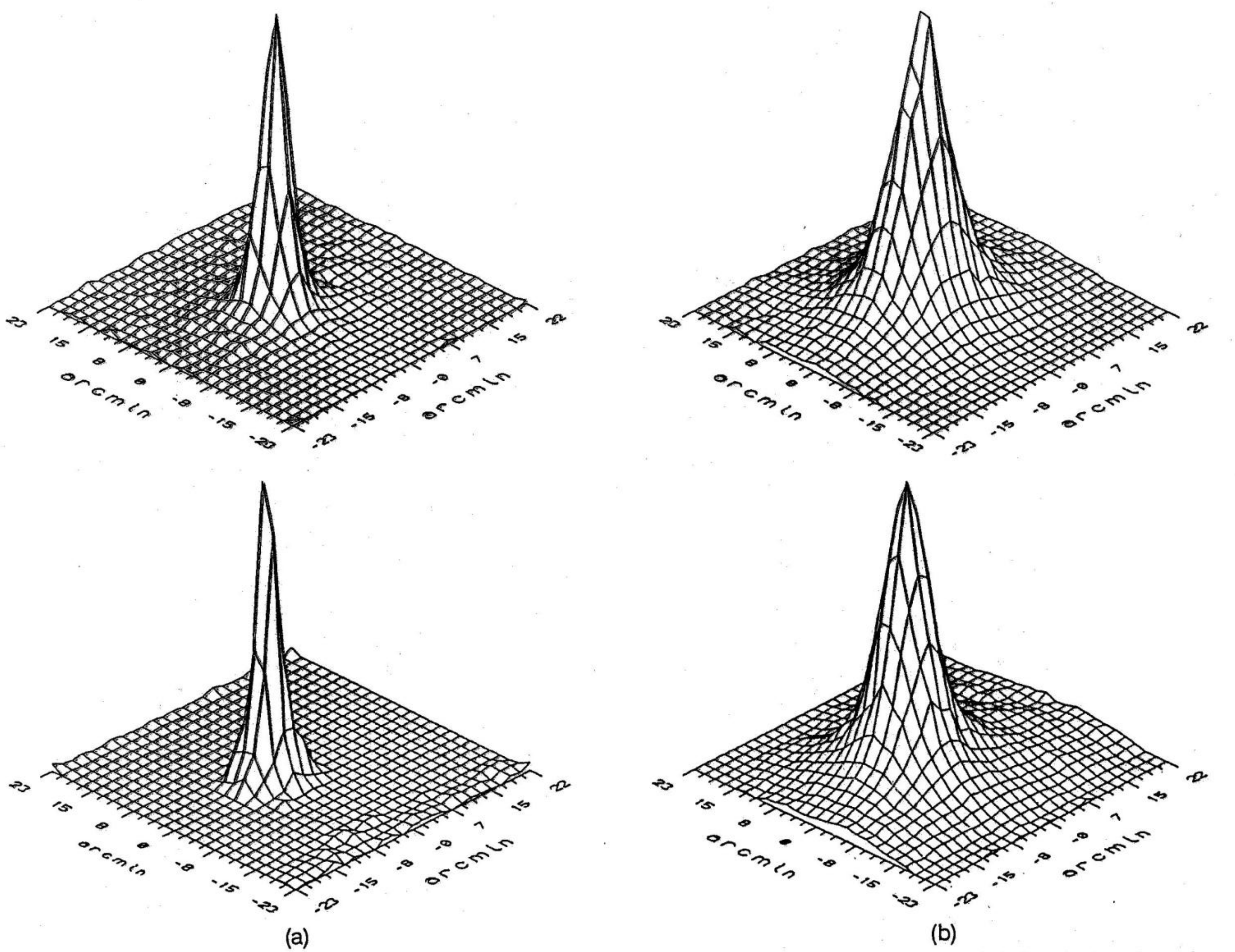

Fig. 2. Aerial retinal images for four subjects: (a) younger subjects, (b) older subjects. The x–y axis is in minutes of arc.

PSF DE OJO EMETROPE Y CUATRO CON IMPLANTES INTRAOCULARES

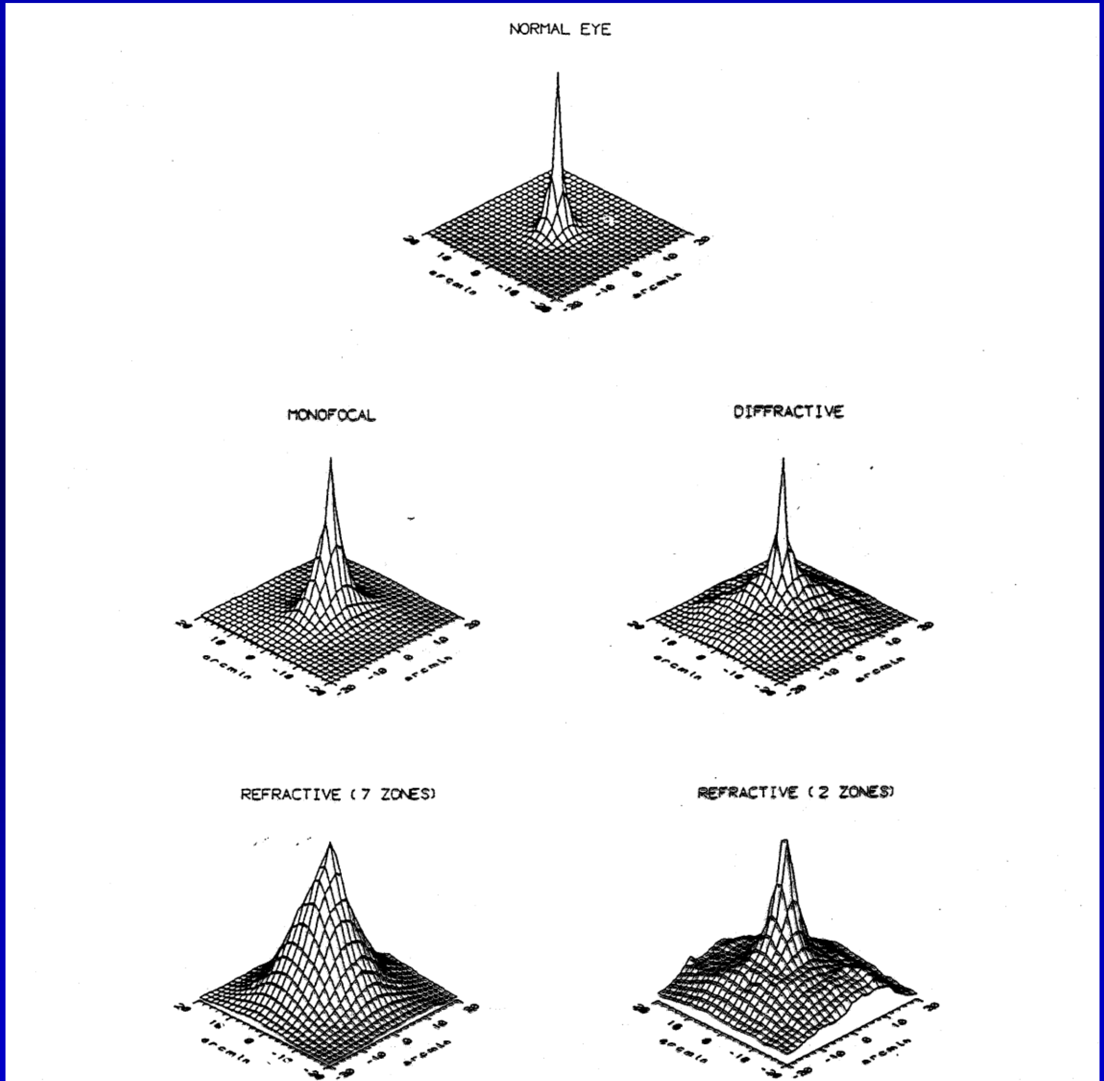

Fig. 2. Perspective three-dimensional plots of the intensity distribution of aerial point-spread functions. Five examples are included illustrating the cases of a normal emmetropic young eye (top) and eyes with implanted IOL's: MO (middle left) and DI (middle right). The lower plots correspond to a refractive multifocal with seven zones (left) and two zones (right).

ABERROMETRO I

Determina:

1- Topografía corneal por Anillos de Placido.

2- Aberraciones totales por incidencia de un haz láser sobre la retina empleando el Sensor de Hartmann-Shack.

ABERROMETRO II
Imagen de la PSF en la retina

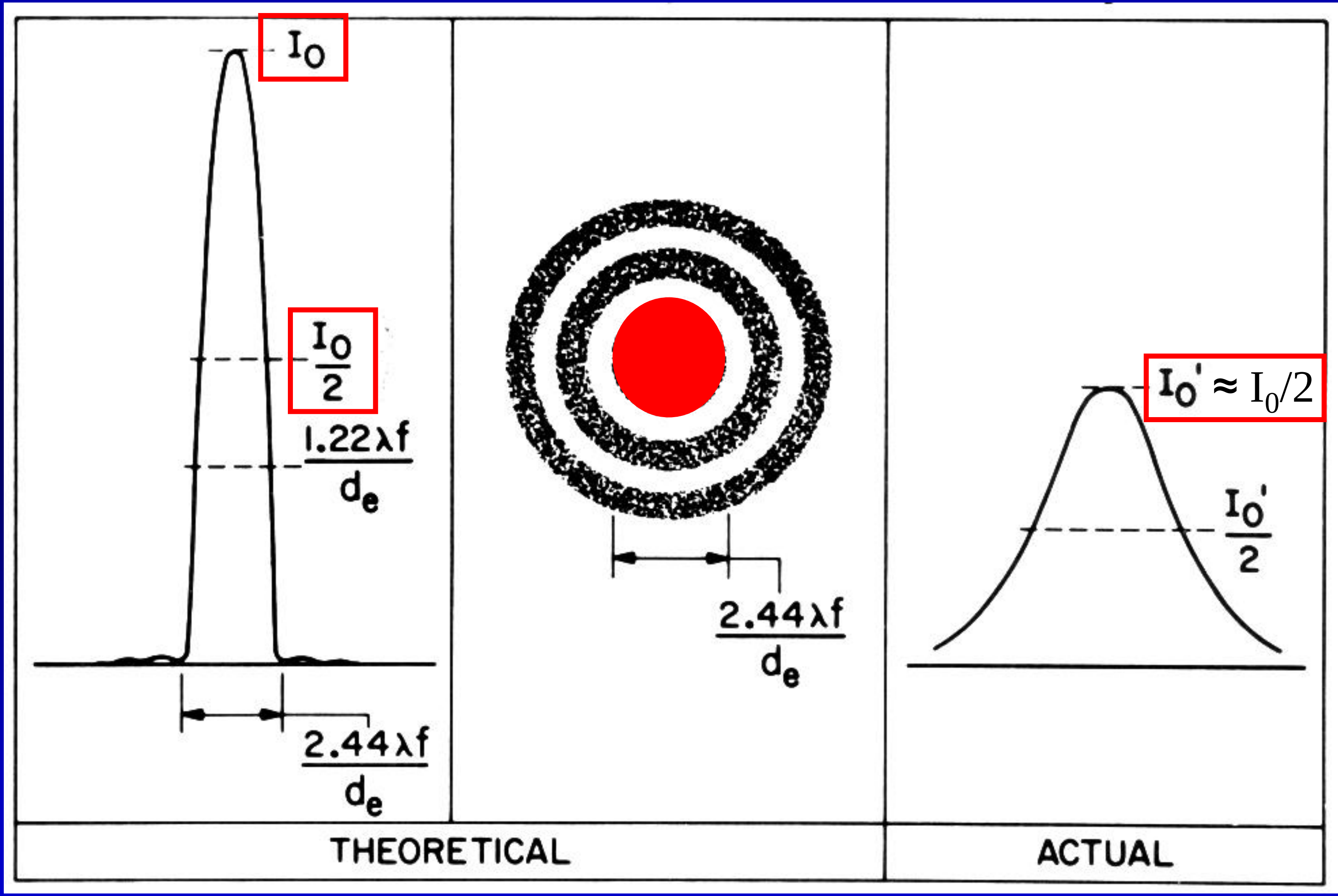

ABERROMETRO III

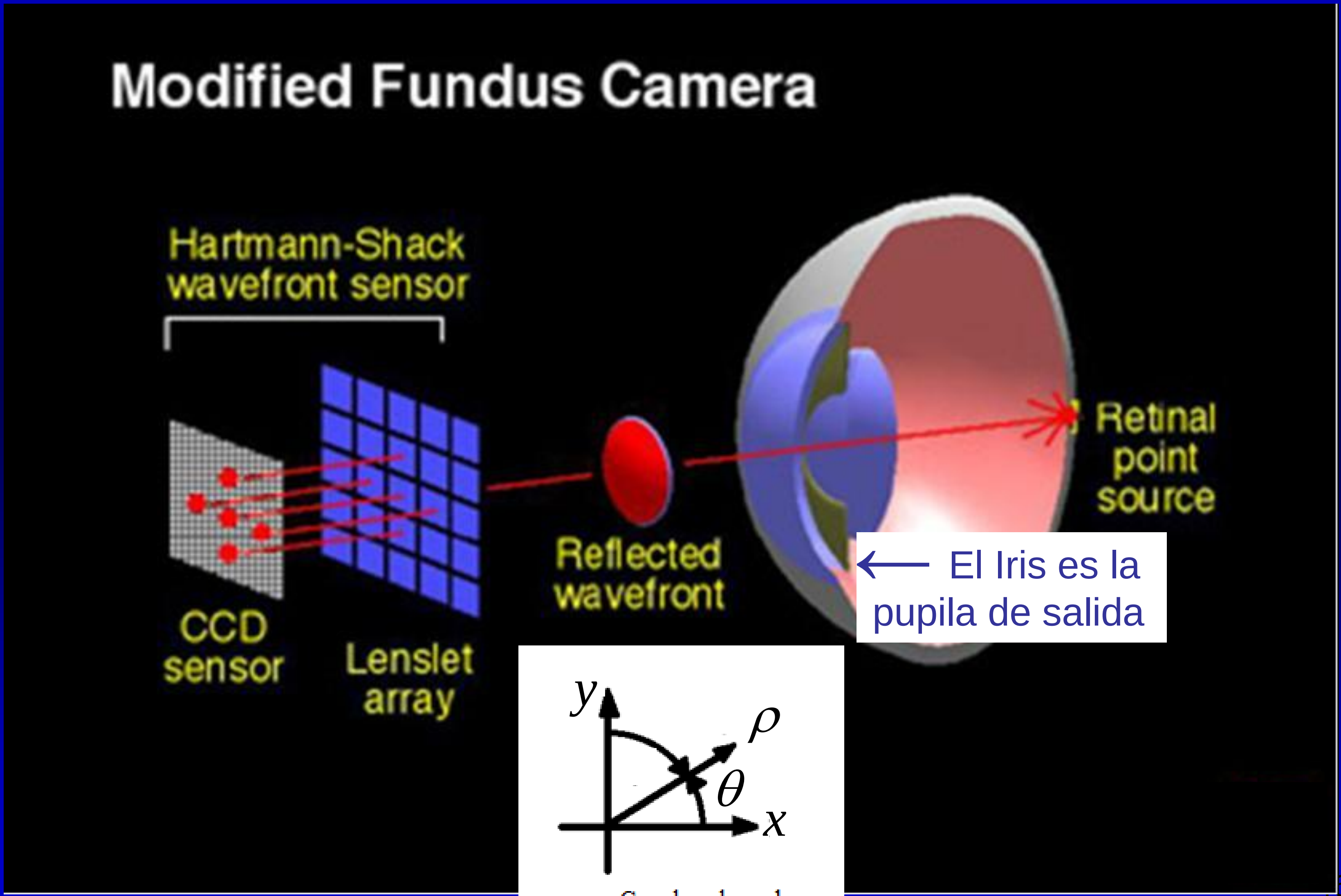

. Coordenadas polares en la pupila de salida.

ABERROMETRO IV

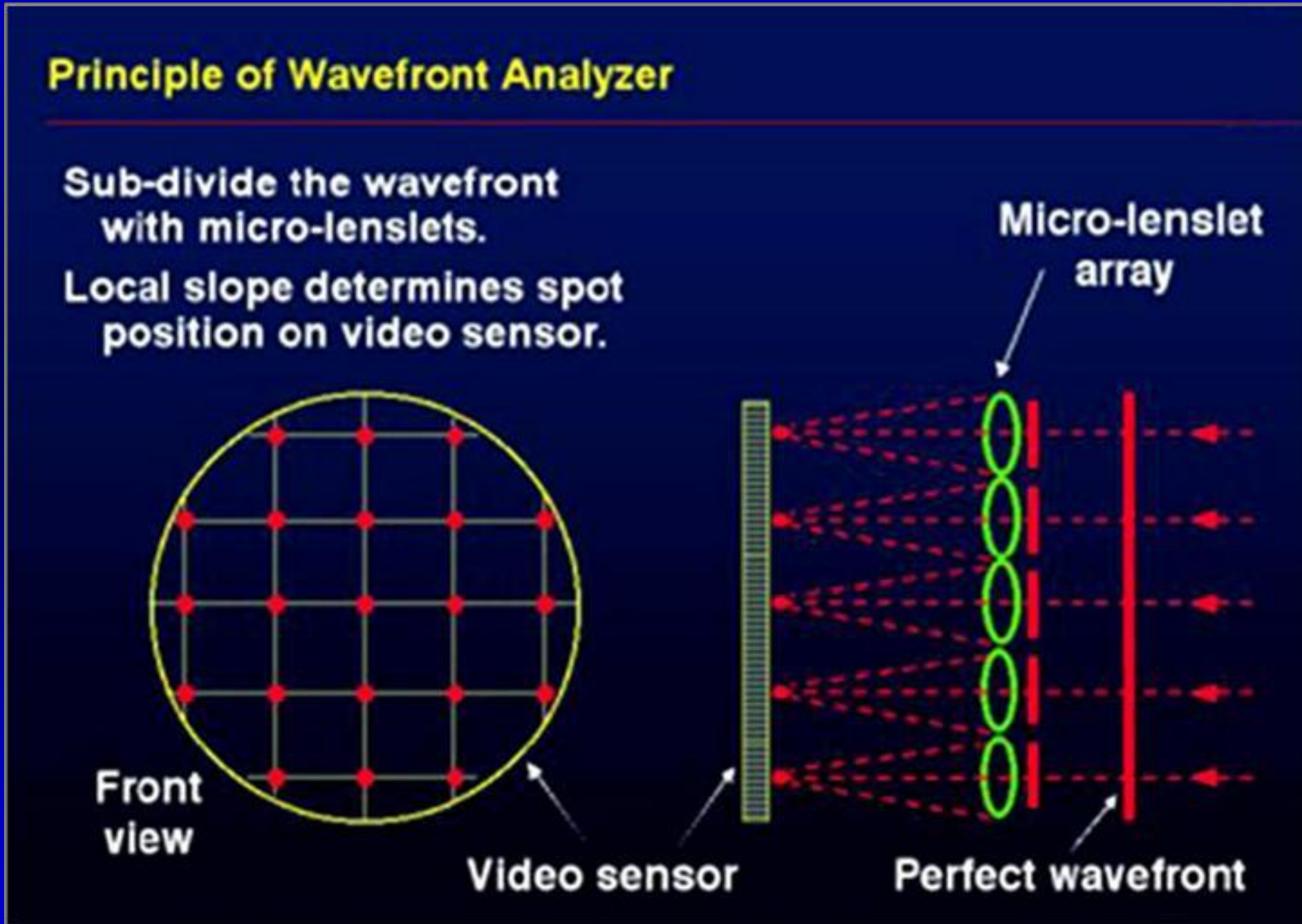

ABERROMETRO V

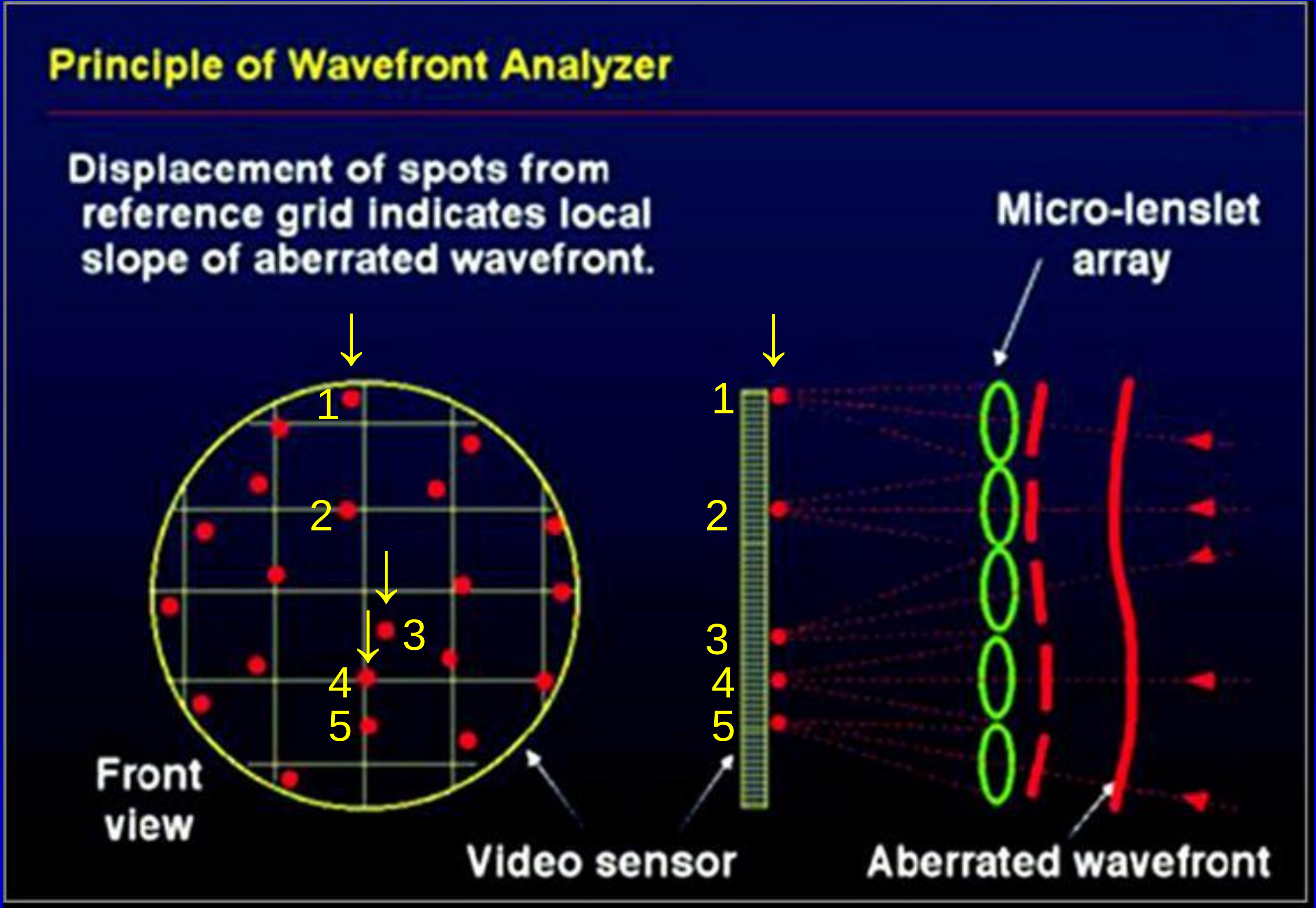

ABERROMETRO VI

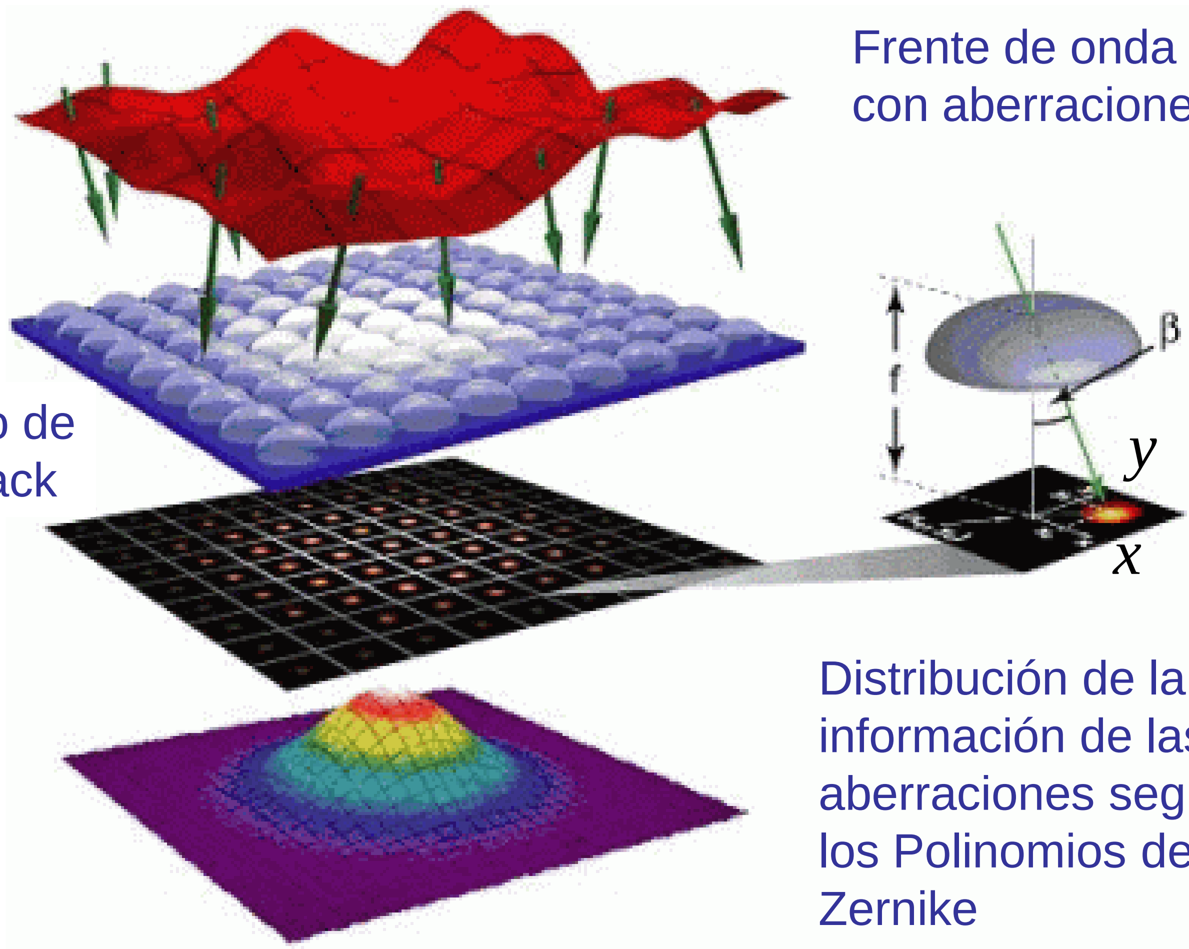

Frente de onda con aberraciones

Sistema Optico de Hartmann- Shack

Distribución de la información de las aberraciones según los Polinomios de Zernike

Fig.10

ABERROMETRO VII

The Shack-Hartmann wavefront sensor uses a grid to measure aberrations in a human eye. This measurement may one day lead to customized laser surgery that will significantly improve vision. Courtesy of Jim Schwiegerling.

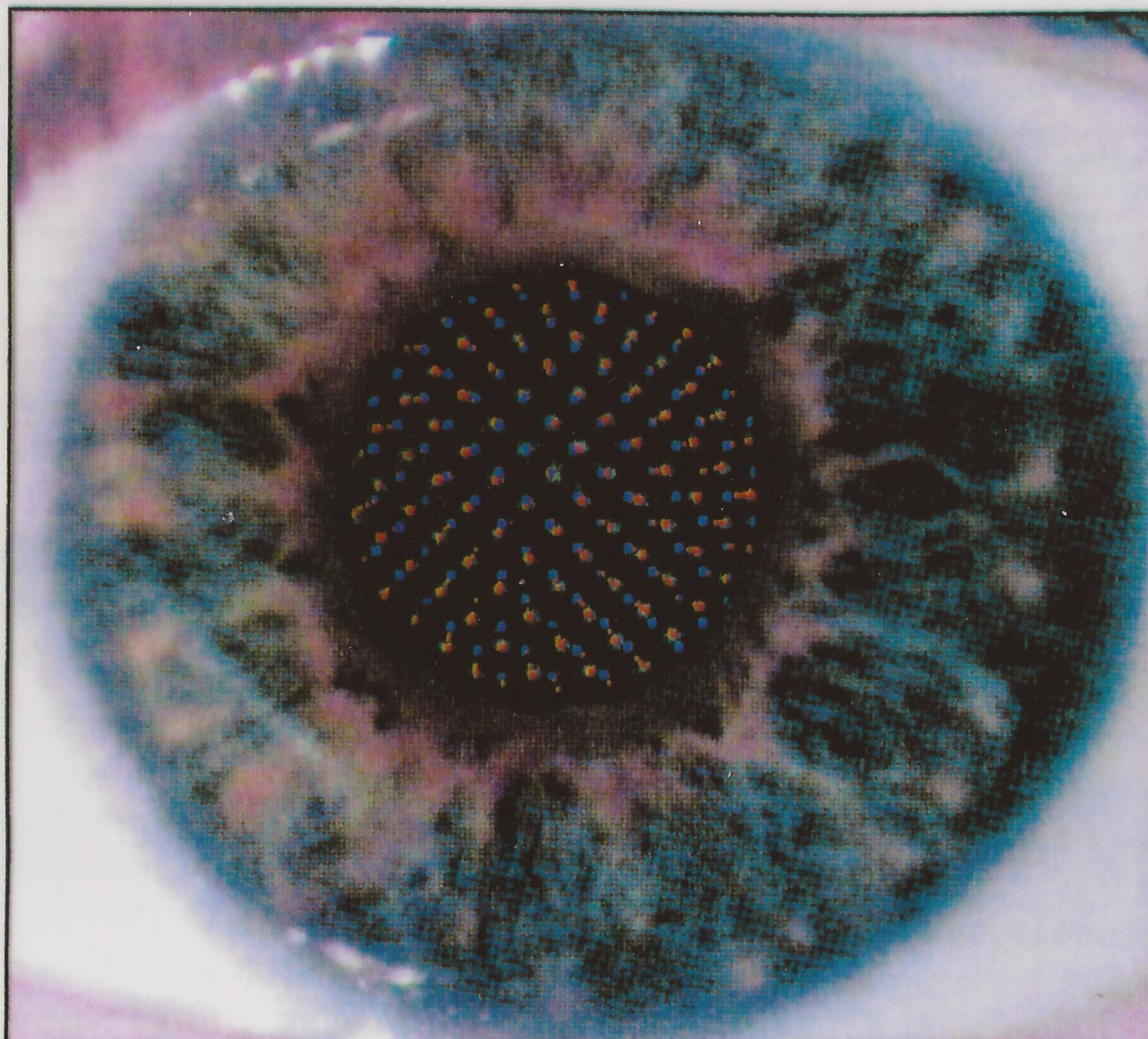

ABERROMETRO X

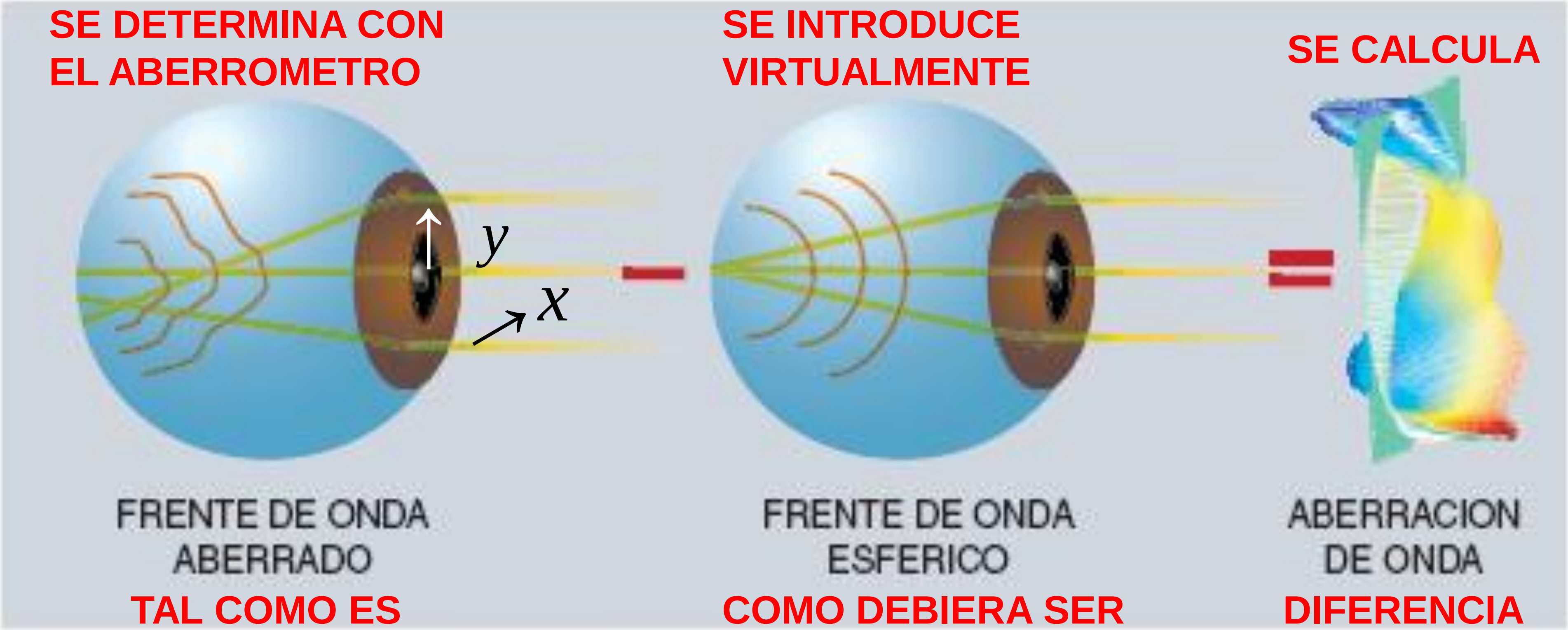

Concepto de aberración de onda.

Además, entre los dos frentes de onda se calculan las diferencias de fase y se elabora un interferograma virtual.

ABERROMETRO XI

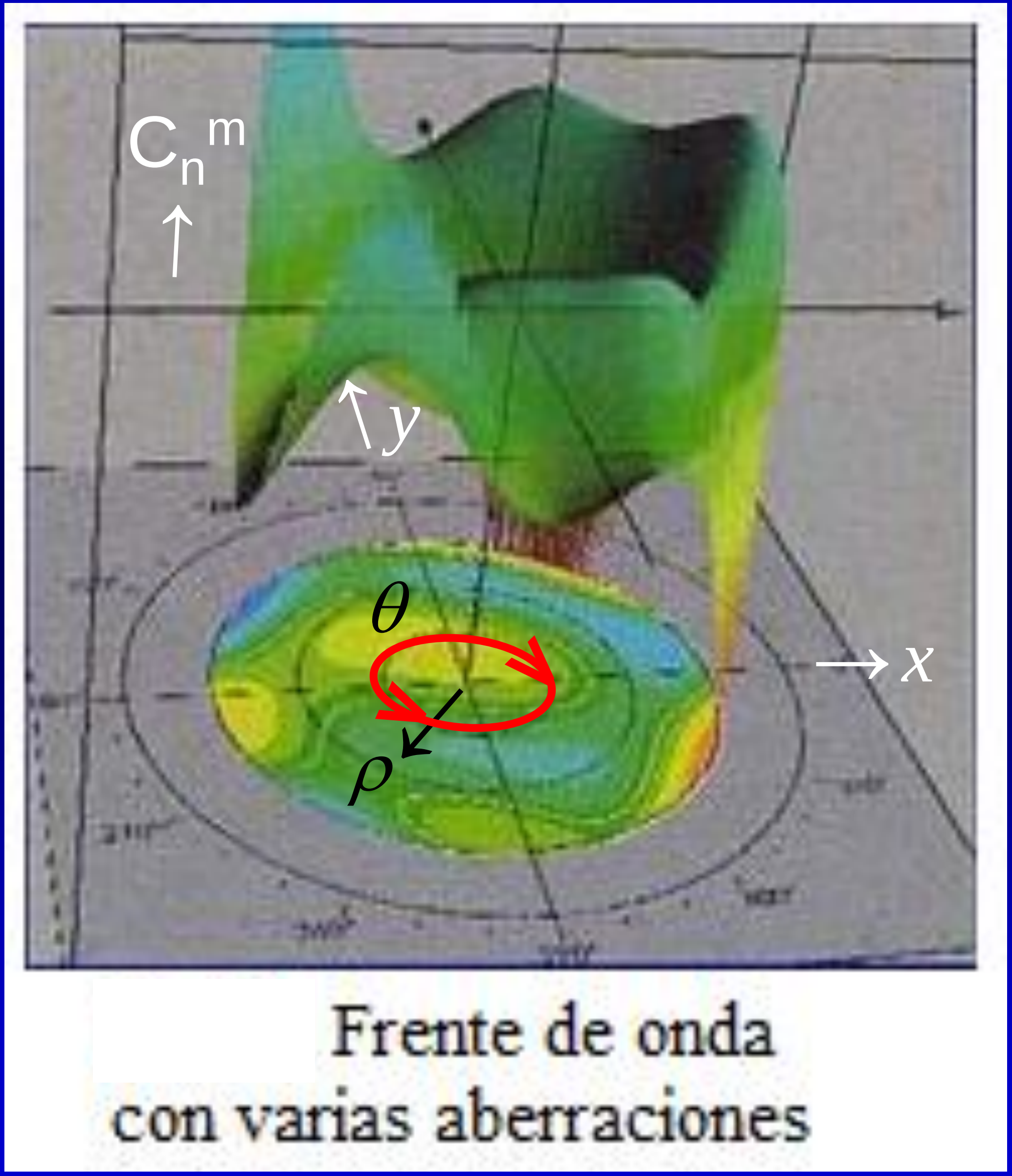

ABERROMETRO XII

- $W(\rho',\theta') = \sum \sum C_n^m \, Z_n^m \, (\rho',\theta')$

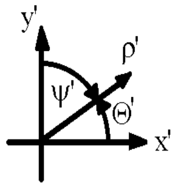

Coordenadas polares en la pupila de salida

- El **Polinomio de Zernike** $Z_n^m(\rho',\theta')$, representa una aberración balanceada y es un término de una base:

$$Z_n^m(\rho',\theta') = N_n^m \; R_n^{|m|}(\rho') \cos(m\theta'), \qquad \text{si } m \geq 0$$

$$Z_n^m(\rho',\theta') = -N_n^m \; R_n^{|m|}(\rho') \,\mathrm{sen}(m\theta'), \qquad \text{si } m < 0$$

$$N_n^m = \left(2\,(n+1) \,/\, (1+\delta_{m0}) \right)^{1/2}$$

$$\delta_{m0} = 1, \text{ si } m = 0; \; \delta_{m0} = 0, \text{ si } m \neq 0.$$

Los polinomios son ortonormales en el círculo de radio unidad:

- C_n^m : coeficiente de ***peso***
- $\boldsymbol{RMS}_{\boldsymbol{Totales}} = \left(\sum \sum (C_n^m)^2 \right)^{1/2}$
- $\boldsymbol{RMS}_{\boldsymbol{Elevado\ Orden}}$ es el $\boldsymbol{RMS}_{\boldsymbol{Totales}}$ quitando los términos $n \leq 2$.

Friderik ZERNIKE (1888-1966) recibió el Premio Nobel de Física de 1953, en particular, por el **microscopio de contraste de fase** que permitió estudiar las células vivas.

LOS 36 TERMINOS DEL POLINOMIO DE ZERNIKE Y SUS NOMBRES

$z0 = 1;$	Piston or Bias
$z1 = \rho\, \mathrm{Cos}[\theta];$	Tilt x
$z2 = \rho\, \mathrm{Sin}[\theta];$	Tilt y
$z3 = -1 + 2\rho^2;$	Power
$z4 = \rho^2\, \mathrm{Cos}[2\theta];$	Astig x
$z5 = \rho^2\, \mathrm{Sin}[2\theta];$	Astig y
$z6 = \rho\,(-2 + 3\rho^2)\, \mathrm{Cos}[\theta];$	Coma x
$z7 = \rho\,(-2 + 3\rho^2)\, \mathrm{Sin}[\theta];$	Coma y
$z8 = 1 - 6\rho^2 + 6\rho^4;$	Primary Spherical
$z9 = \rho^3\, \mathrm{Cos}[3\theta];$	Trefoil x
$z10 = \rho^3\, \mathrm{Sin}[3\theta];$	Trefoil y
$z11 = \rho^2\,(-3 + 4\rho^2)\, \mathrm{Cos}[2\theta];$	Secondary Astigmatism x
$z12 = \rho^2\,(-3 + 4\rho^2)\, \mathrm{Sin}[2\theta];$	Secondary Astigmatism y
$z13 = \rho\,(3 - 12\rho^2 + 10\rho^4)\, \mathrm{Cos}[\theta];$	Secondary Coma x
$z14 = \rho\,(3 - 12\rho^2 + 10\rho^4)\, \mathrm{Sin}[\theta];$	Secondary Coma y
$z15 = -1 + 12\rho^2 - 30\rho^4 + 20\rho^6;$	Secondary Spherical
$z16 = \rho^4\, \mathrm{Cos}[4\theta];$	Tetrafoil x
$z17 = \rho^4\, \mathrm{Sin}[4\theta];$	Tetrafoil y
$z18 = \rho^3\,(-4 + 5\rho^2)\, \mathrm{Cos}[3\theta];$	Secondary Trefoil x
$z19 = \rho^3\,(-4 + 5\rho^2)\, \mathrm{Sin}[3\theta];$	Secondary Trefoil y
$z20 = \rho^2\,(6 - 20\rho^2 + 15\rho^4)\, \mathrm{Cos}[2\theta];$	Tertiary Astigmatism x
$z21 = \rho^2\,(6 - 20\rho^2 + 15\rho^4)\, \mathrm{Sin}[2\theta];$	Tertiary Astigmatism y
$z22 = \rho\,(-4 + 30\rho^2 - 60\rho^4 + 35\rho^6)\, \mathrm{Cos}[\theta];$	Tertiary Coma x
$z23 = \rho\,(-4 + 30\rho^2 - 60\rho^4 + 35\rho^6)\, \mathrm{Sin}[\theta];$	Tertiary Coma y
$z24 = 1 - 20\rho^2 + 90\rho^4 - 140\rho^6 + 70\rho^8;$	Tertiary Spherical
$z25 = \rho^5\, \mathrm{Cos}[5\theta];$	Pentafoil x
$z26 = \rho^5\, \mathrm{Sin}[5\theta];$	Pentafoil y
$z27 = \rho^4\,(-5 + 6\rho^2)\, \mathrm{Cos}[4\theta];$	Secondary Tetrafoil x
$z28 = \rho^4\,(-5 + 6\rho^2)\, \mathrm{Sin}[4\theta];$	Secondary Tetrafoil y
$z29 = \rho^3\,(10 - 30\rho^2 + 21\rho^4)\, \mathrm{Cos}[3\theta];$	Tertiary Trefoil x
$z30 = \rho^3\,(10 - 30\rho^2 + 21\rho^4)\, \mathrm{Sin}[3\theta];$	Tertiary Trefoil y
$z31 = \rho^2\,(-10 + 60\rho^2 - 105\rho^4 + 56\rho^6)\, \mathrm{Cos}[2\theta];$	Quatenary Astigmatism x
$z32 = \rho^2\,(-10 + 60\rho^2 - 105\rho^4 + 56\rho^6)\, \mathrm{Sin}[2\theta];$	Quatenary Astigmatism y
$z33 = \rho\,(5 - 60\rho^2 + 210\rho^4 - 280\rho^6 + 126\rho^8)\, \mathrm{Cos}[\theta];$	Quatenary Coma x
$z34 = \rho\,(5 - 60\rho^2 + 210\rho^4 - 280\rho^6 + 126\rho^8)\, \mathrm{Sin}[\theta];$	Quatenary Coma y
$z35 = -1 + 30\rho^2 - 210\rho^4 + 560\rho^6 - 630\rho^8 + 252\rho^{10};$	Quaternary Spherical

j = Índice	n = orden	m = frecuencia	$Z_n^m(\rho,\theta)$
0	0	0	Pistón 1
1	1	-1	Inclinación $2\rho\sin\theta$
2	1	1	Inclinación $2\rho\cos\theta$
3	2	-2	± Astigmat. $\sqrt{6}\,\rho^2\sin 2\theta$
4	2	0	± Desenfoq. $\sqrt{3}\,(2\rho^2-1)$ Hiperm. Miope
5	2	2	± Astigmat. $\sqrt{6}\,\rho^2\cos 2\theta$
6	3	-3	$\sqrt{8}\,\rho^3\sin 3\theta$
7	3	-1	± Coma $\sqrt{8}\,(3\rho^3-2\rho)\sin\theta$
8	3	1	± Coma $\sqrt{8}\,(3\rho^3-2\rho)\cos\theta$
9	3	3	$\sqrt{8}\,\rho^3\cos 3\theta$
10	4	-4	$\sqrt{10}\,\rho^4\sin 4\theta$
11	4	-2	$\sqrt{10}\,(4\rho^4-3\rho^2)\sin 2\theta$
12	4	0	Aberración Esférica $\sqrt{5}\,(6\rho^4-6\rho^2+1)$
13	4	2	$\sqrt{10}\,(4\rho^4-3\rho^2)\cos 2\theta$

ABERROMETRO XIII

Coeficientes de Zernike y su representación matemática funcional

$$j = \frac{n(n+2)+m}{2}$$

ABERROMETRO XV

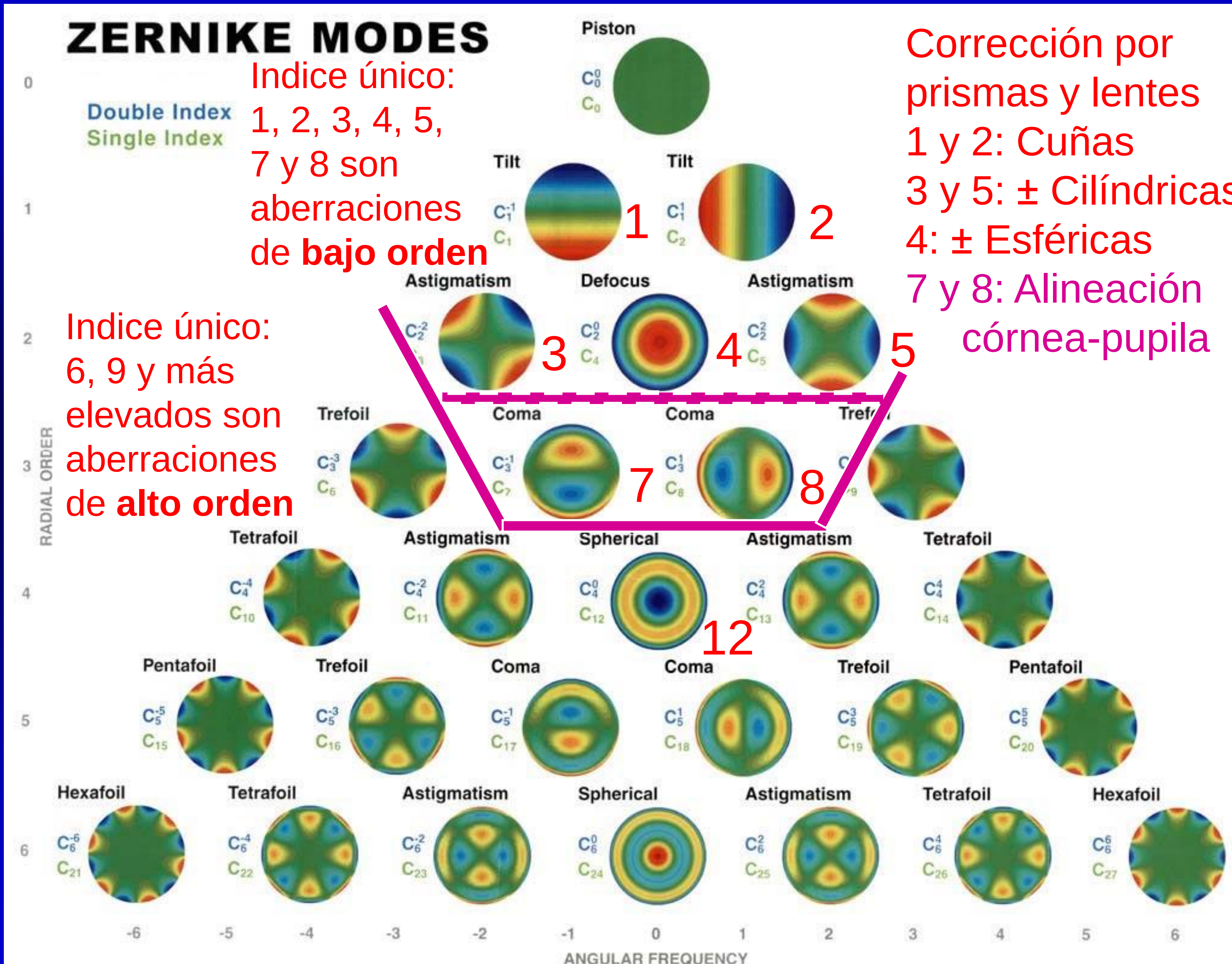

PSF: MODELO DE OJO IDEAL

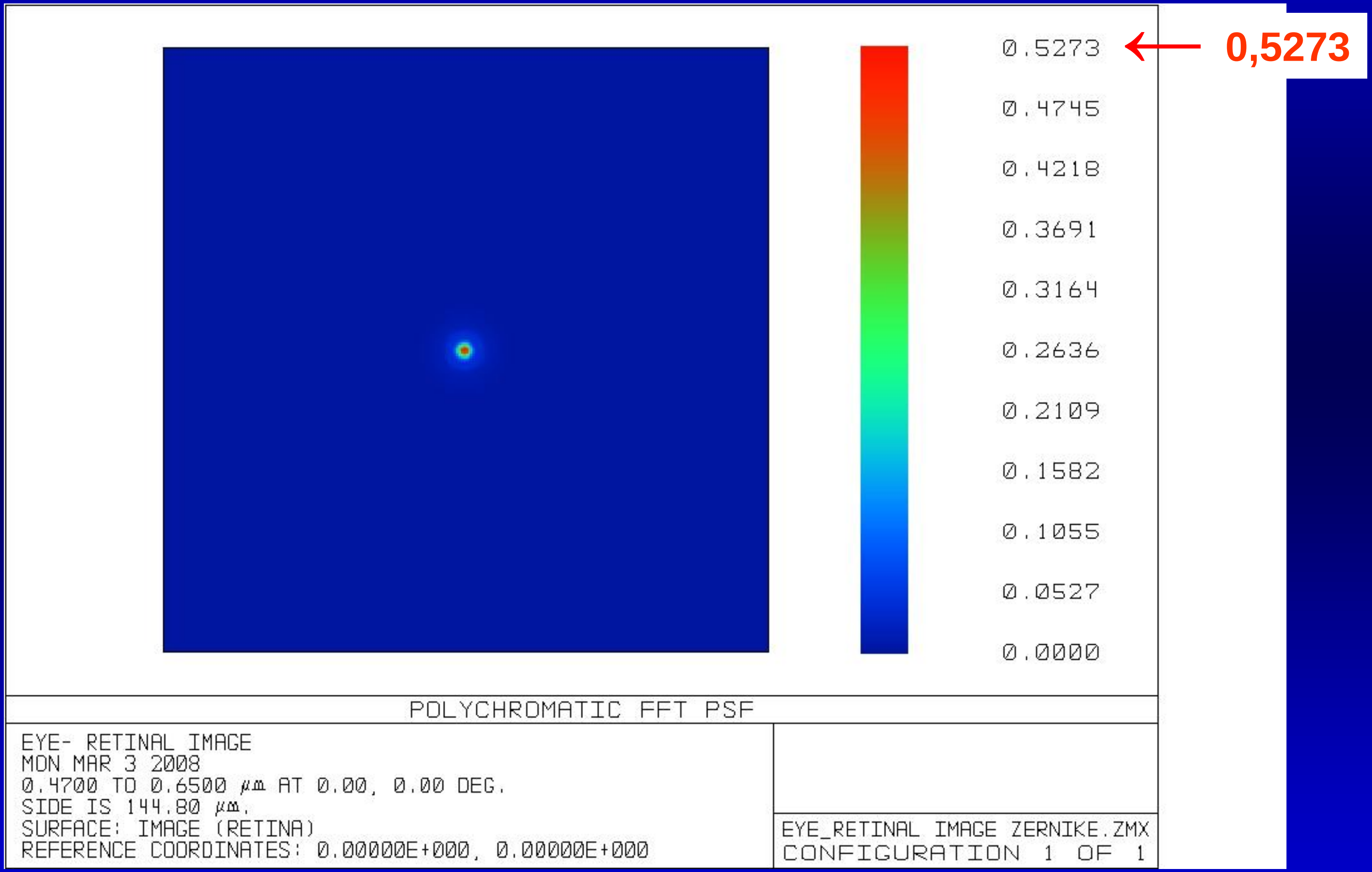

Rayos incidiendo a 0°

PSF: MODELO DE CORNEA CON COMA

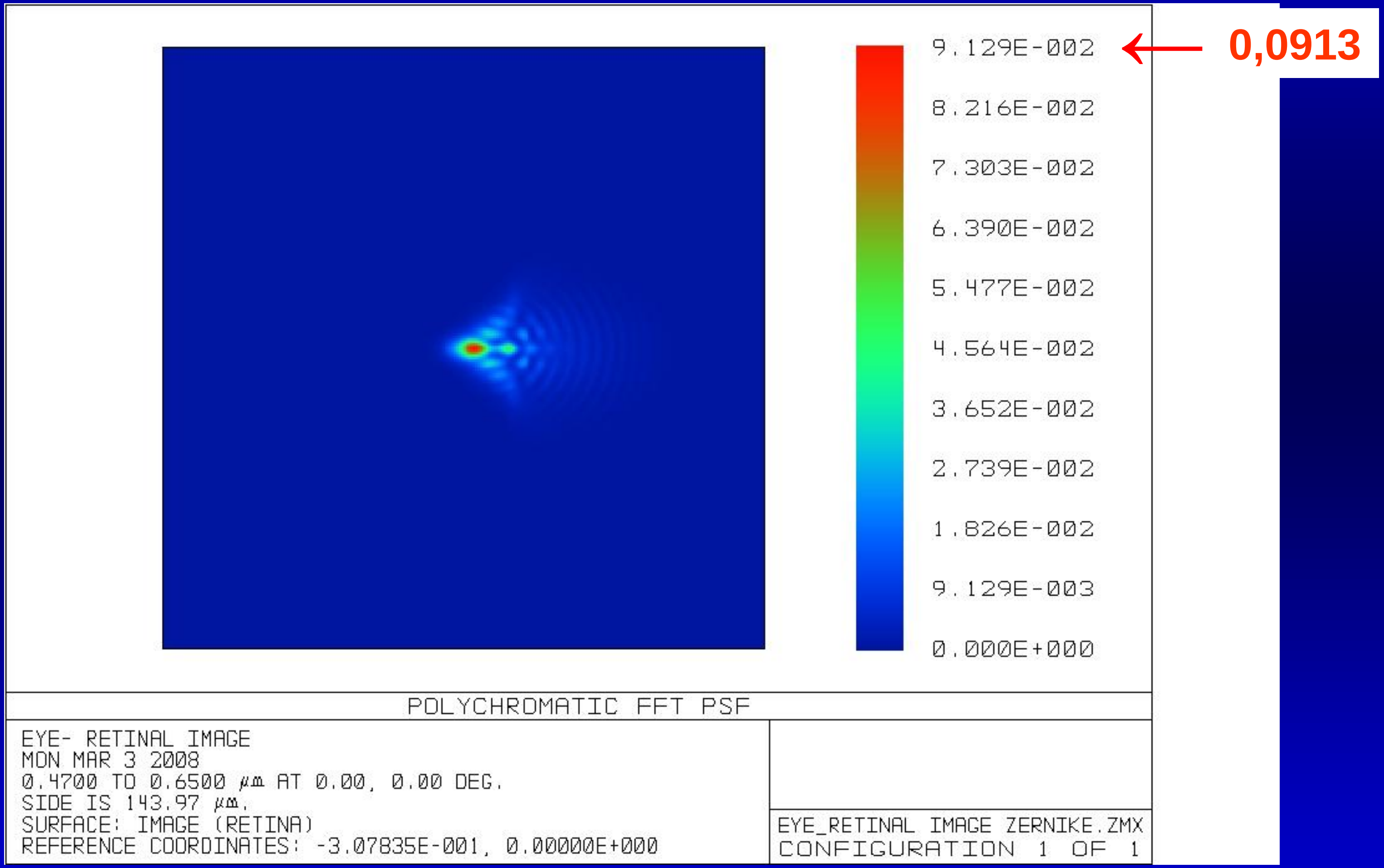

Rayos incidiendo a 0°

PSF: MODELO DE CRISTALINO CON COMA

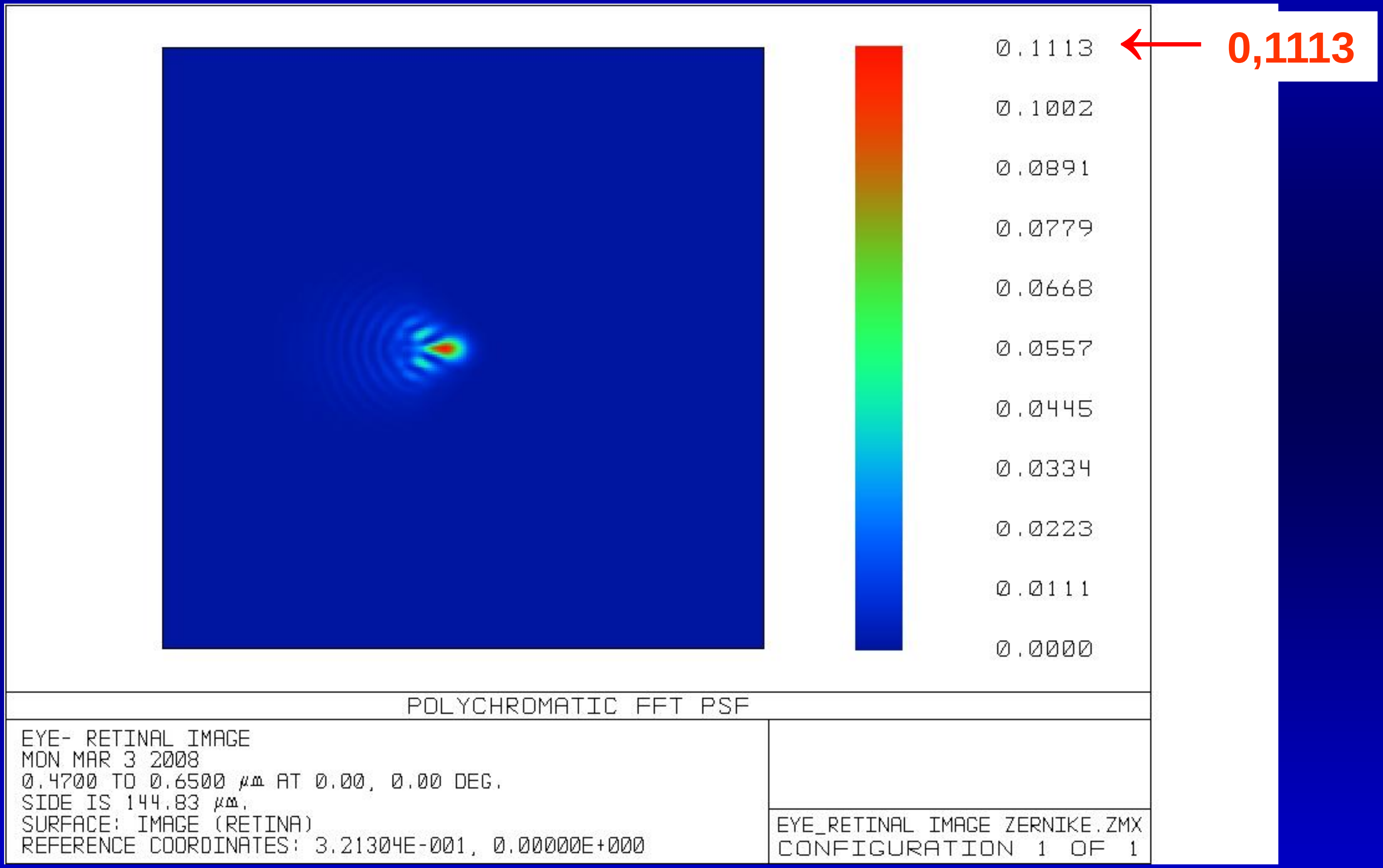

Rayos incidiendo a 0°

PSF: MODELO DE OJO CON COMA COMPENSADO

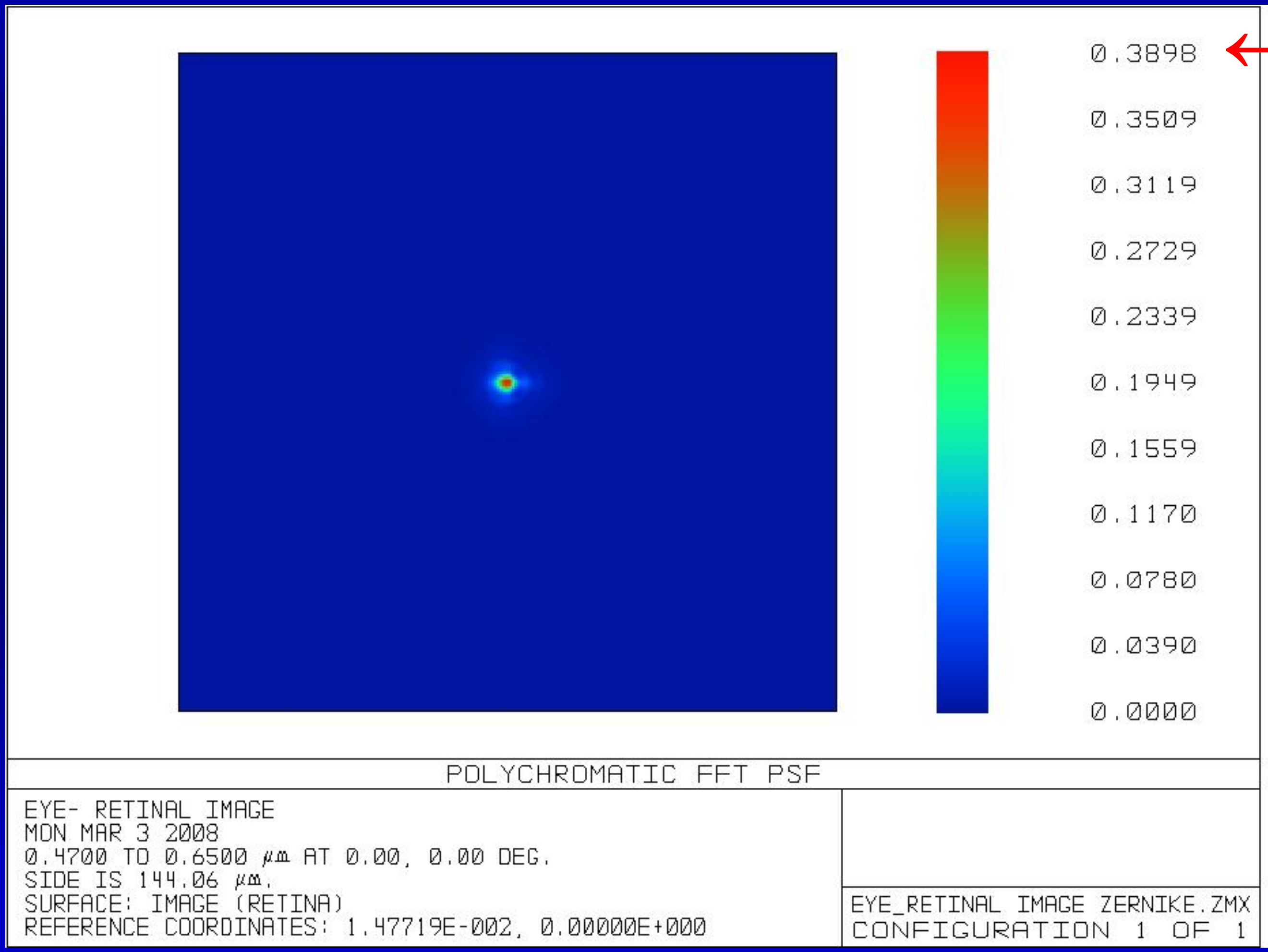

0,3898

Rayos incidiendo a 0°

A New Intraocular Lens to Correct Corneal Coma

Juan Tabernero and Pablo Artal

The aberrations of the eye tend to be well balanced among optical components of the ocular system, the cornea and the crystalline lens.[1,2] This means that a high level of corneal aberrations is usually compensated with a high level of opposite sign aberrations generated by the crystalline lens. This is a well-studied effect in the case of spherical aberration. Corneal spherical aberration is usually positive while lens spherical aberration tends to be negative. The result of these extensive investigations was a new generation of aspheric intraocular lenses with negative spherical aberration that replace the lens after cataract surgery.[3]

Apart from spherical aberration, other aberrations, such as coma, are well balanced in the eye.[4] The mechanism responsible for this effect has been recently studied,[5] revealing that the eye's optical characteristics are very similar to an aplanatic optical system, corrected for off-axis coma and on-axis spherical aberration.

Our main concern was that, after crystalline lens extraction in cataract surgery, the best intraocular lens design should imitate the optimal optical characteristics of the normal eye. However, the conventional intraocular lens designs have the same shape factor for a whole range of physiological optical powers (from 10 to 30 diopters). In many cases, these fixed shape factors (usually equibiconvex) are far from the optimized solutions. Therefore, we improved the intraocular lens designs according to the compensation of aberrations found in normal eyes.

Our target was to obtain an intraocular lens that compensates the average corneal spherical aberration and corneal off axis coma in the eye. We used two variables for the design: the shape factor of the intraocular lens that controlled the offaxis coma and the aspheric coefficients of both lens surfaces that controlled the level of spherical aberration.[6]

Two procedures were tested for design. First, an *ab initio* solution was obtained from Seidel aberration theory. This solution was used as the starting point for an optimization procedure performed with ray tracing software through schematic eye models. Finally, simulations were also performed using real eye models, with the corneal surface measured from topography, to check the real performance of the solution.

The resulting shape factors of the intraocular lens solution were meniscus bended toward the retina (for the lower powers) evolving to biconvex shapes with the increase of intraocular lens power. The aspheric coefficients in both surfaces generated negative spherical aberration opposite to the normal positive values of the cornea.

In conclusion, we designed a new generation of very promising intraocular lenses by mimicking the natural optimal situation found in the normal eye. Simulations using data of real measured aberrations indicated that a significant improvement in optical quality can be expected with respect to conventional intraocular lens implants. ▲

[Juan Tabernero (juant@um.es) and Pablo Artal are with the Laboratory of Optics, University of Murcia, Spain.]

References

1. P. Artal and A. Guirao. "Contributions of the cornea and the lens to the aberrations of the human eye," Opt. Lett. **23**, 1713-15 (1998).
2. P. Artal et al. "Compensation of corneal aberrations by internal optics in the human eye," J. Vision **1**, 1-8 (2001).
3. J.T. Holladay et al. "A new intraocular lens design to reduce spherical aberration of pseudophakic eyes," J. Refract. Surg. **18**, 683-91 (2002).
4. P. Artal et al. "The human eye is an example of robust optical design," J. Vision **6**, 1-7 (2006).
5. J. Tabernero et al. "Mechanism of compensation of aberrations in the human eye," J. Opt. Soc. Am. A **24**, 3274-83 (2007).
6. J. Tabernero et al. "Intraocular lens to correct corneal coma," Opt. Lett. **32**, 406-8 (2007).

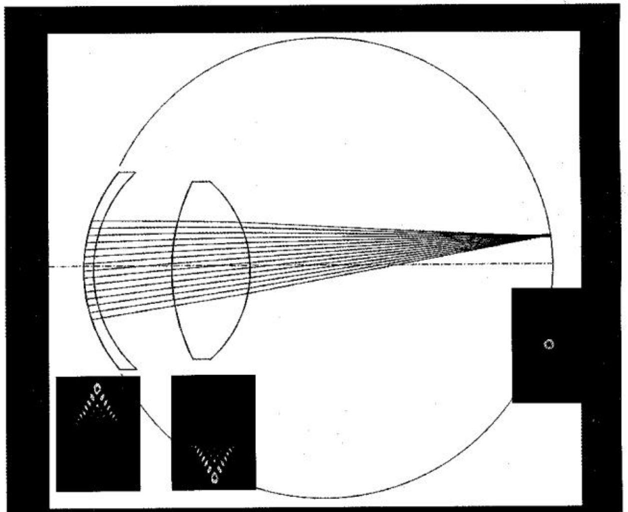

Coma is well balanced in the normal eye

Una nueva Lente Intraocular para Corregir la Aberración por Coma de la Córnea I

Optics and Photonics News, December 2007.

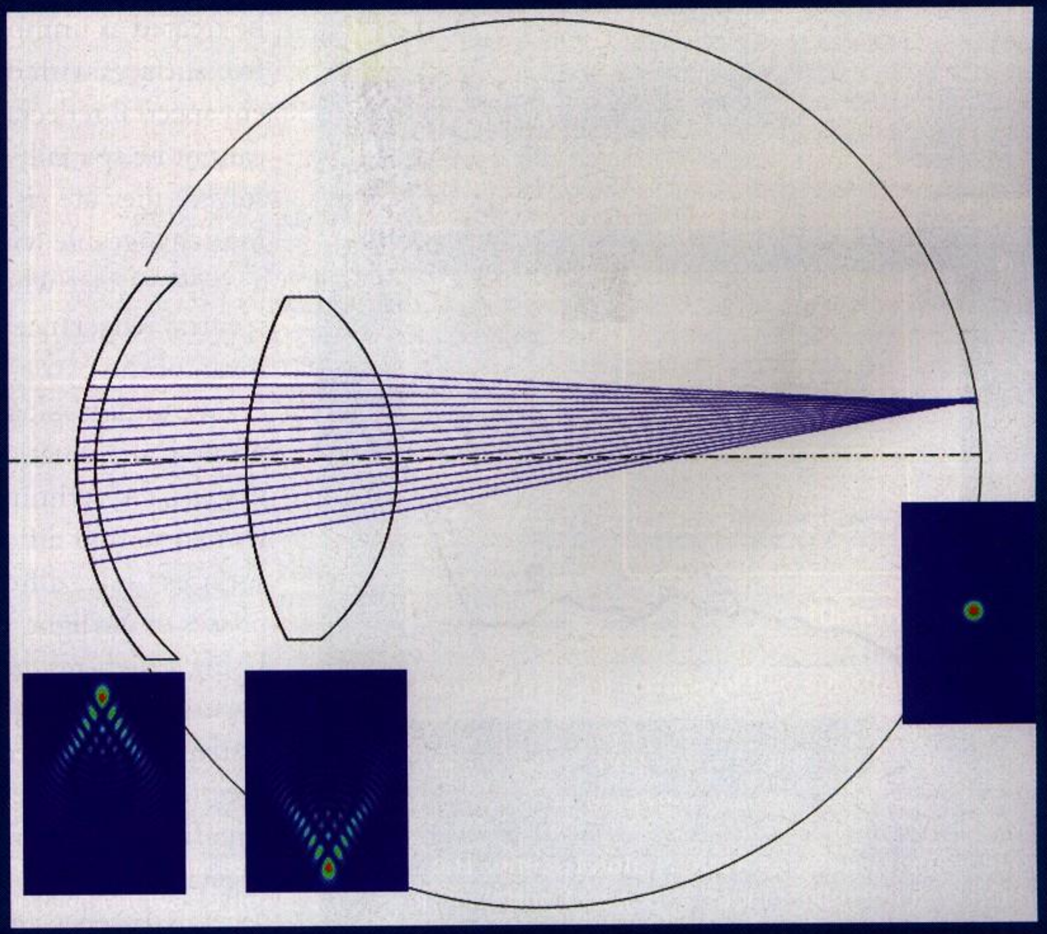

Coma is well balanced in the normal eye

Una nueva Lente Intraocular para Corregir la Aberración por Coma de la Córnea II

AGUDEZA VISUAL vs DISTANCIA A LA FOVEA

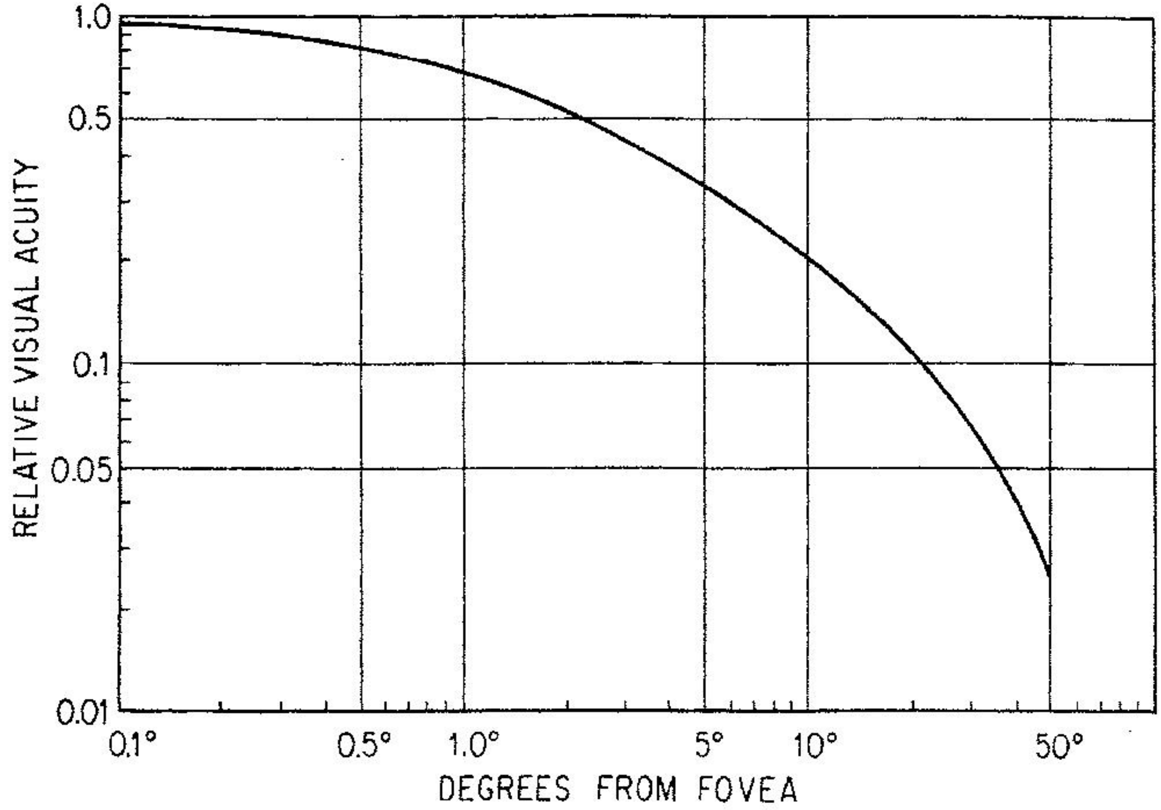

Fig. 11.25. The variation of visual acuity with retinal position relative to the fovea. (From [555]. Reprinted with permission of McGraw-Hill)

DISTRIBUCION DE CONOS Y DE BASTONES EN LA RETINA HUMANA

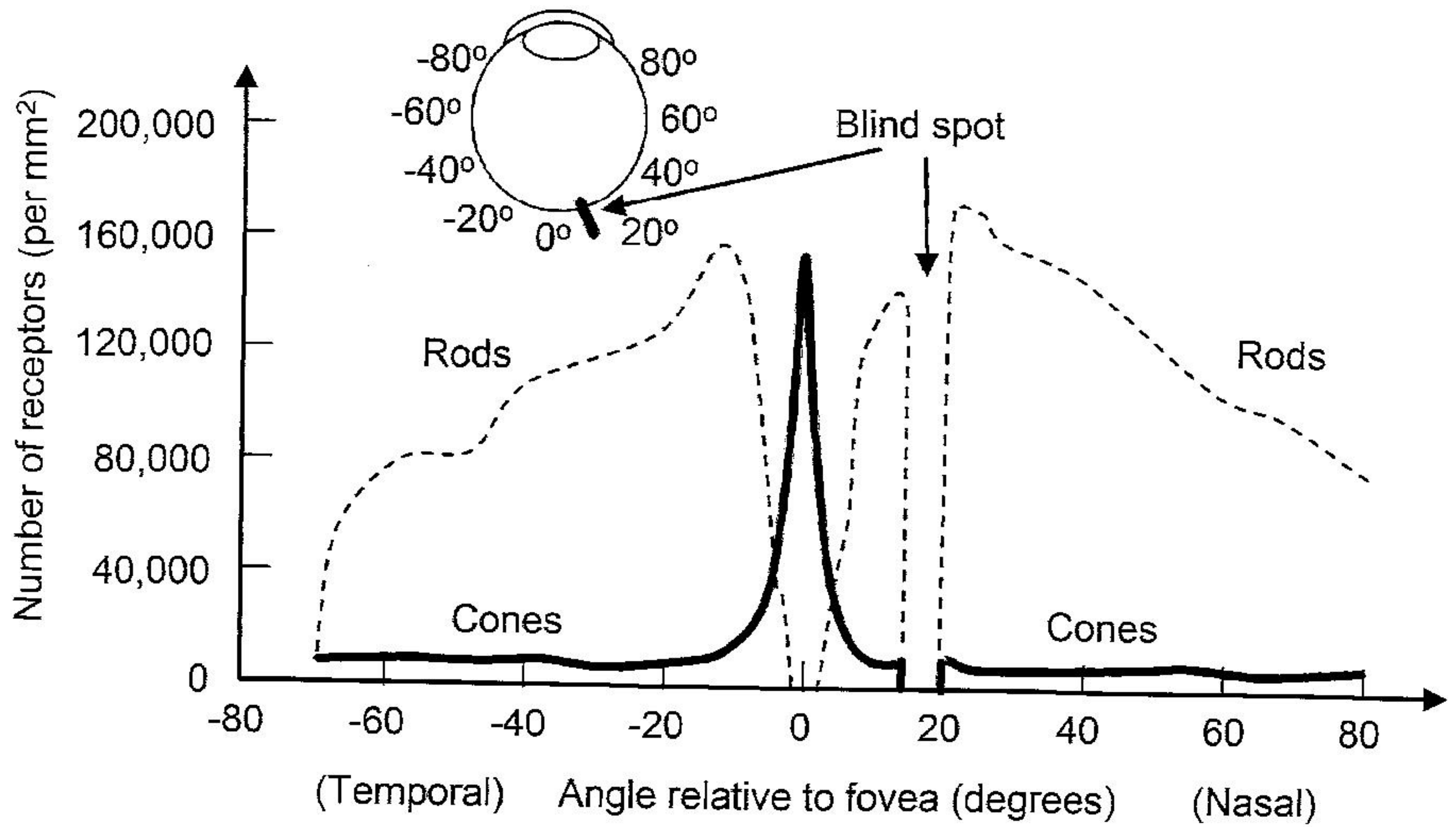

Fig. 11.3. Distribution of rods and cones on the retina, and the location of the blind spot. (Based on [523] and [560])

DIMENSIONES TIPICAS DE CONOS Y BASTONES II

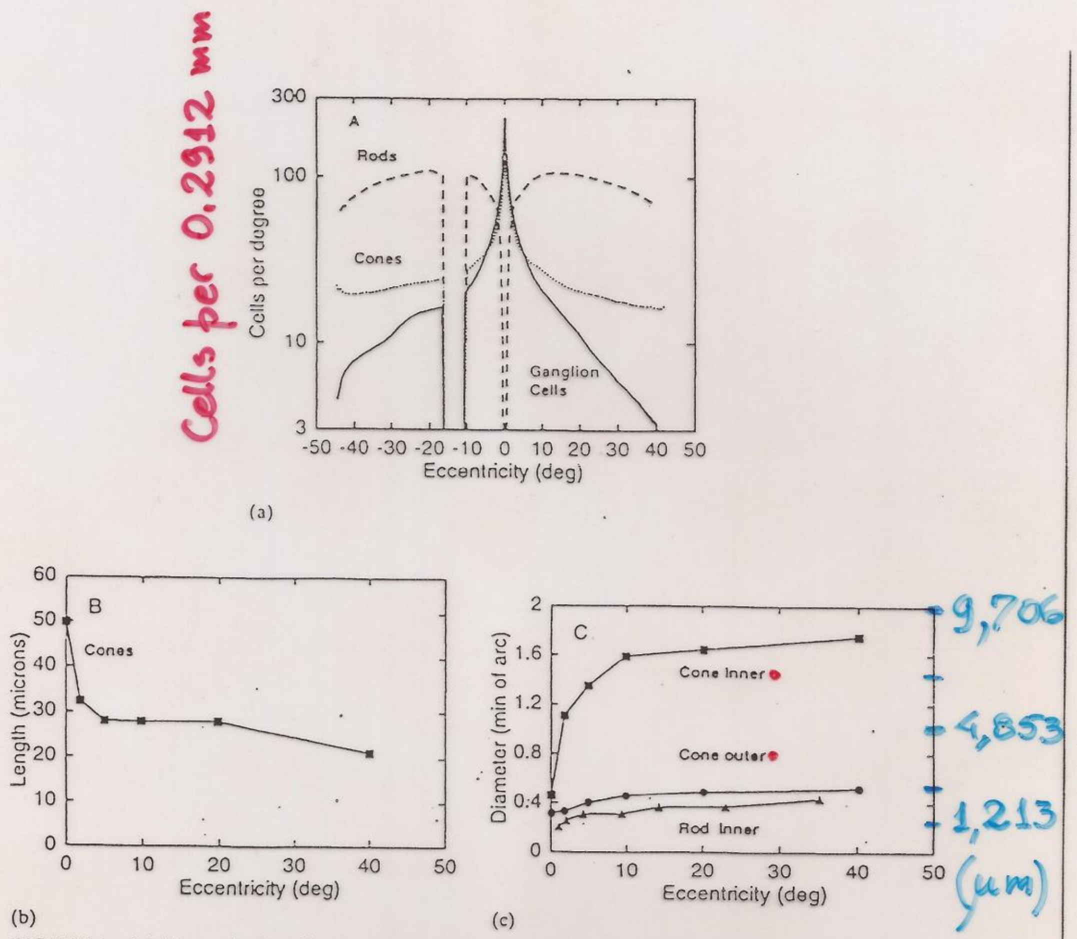

FIGURE 2 (*a*) Linear density of cones, rods, and ganglion cells as a function of eccentricity in the human retina. (The data were modified from Refs. 6 and 32.) Conversion from cells/mm^2 to cells/deg^2 was computed assuming a posterior nodal point 16.68 mm from the retina, and a retinal radius of curvature of 12.1 mm. Conversion to cells/deg was obtained by taking the square root of areal density. Ganglion cell density in the central 10 deg was derived assuming a 3:1 ratio of ganglion cells to cones in the fovea.[32] (*b*) Human cone outer segment length. (Modified from Ref. 125.) (*c*) Human cone inner segment, cone outer segment and rod diameter as a function of eccentricity. (Modified from Ref. 125.)

TIPO Y CANTIDAD DE COMPONENTES EN LA RETINA

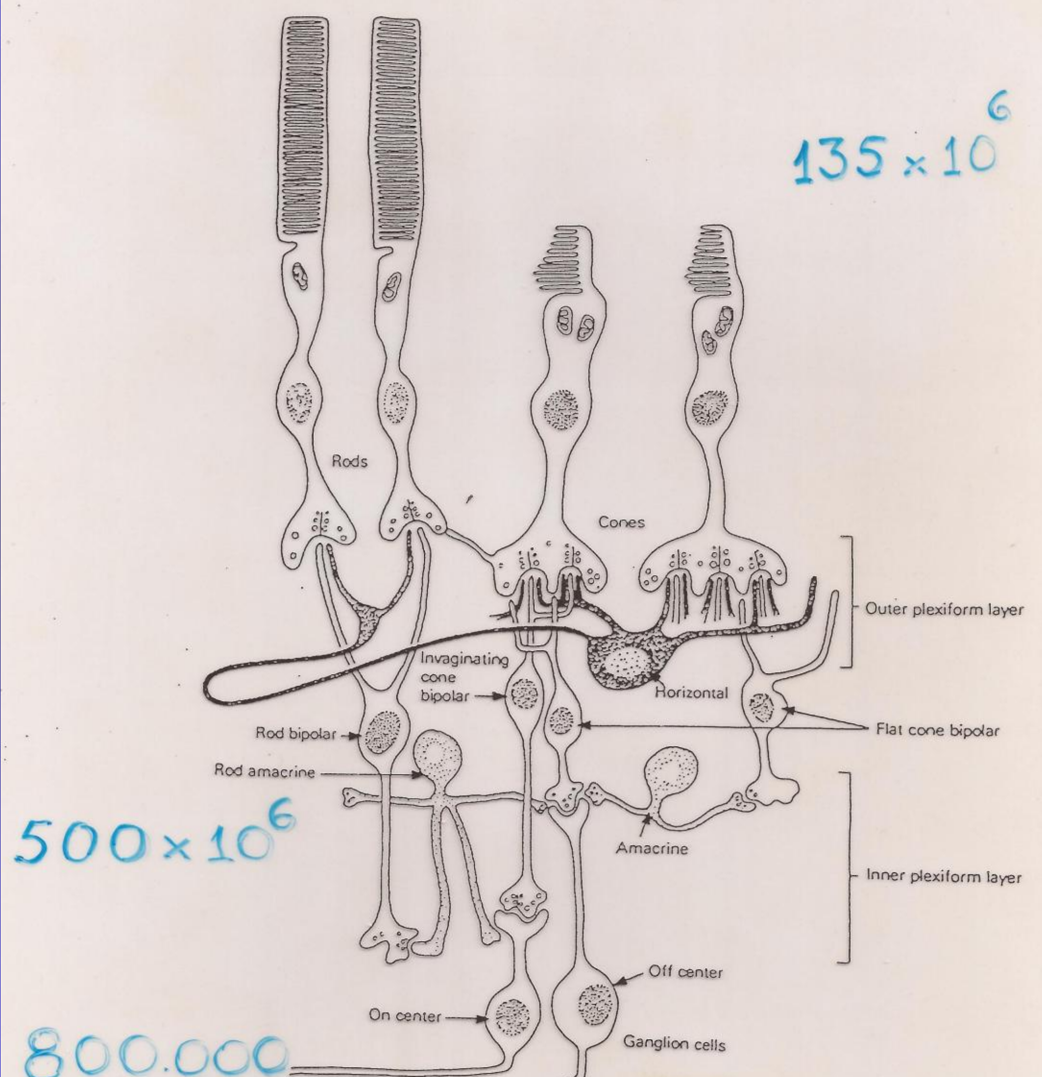

FIGURE 1 Schematic diagram of the retinal neurons and their major synaptic connections. Note that rods, rod bipolar cells, and rod amacrine cells are absent in the fovea. *(From Ref. 262.)*

AGUDEZA VISUAL vs BRILLO

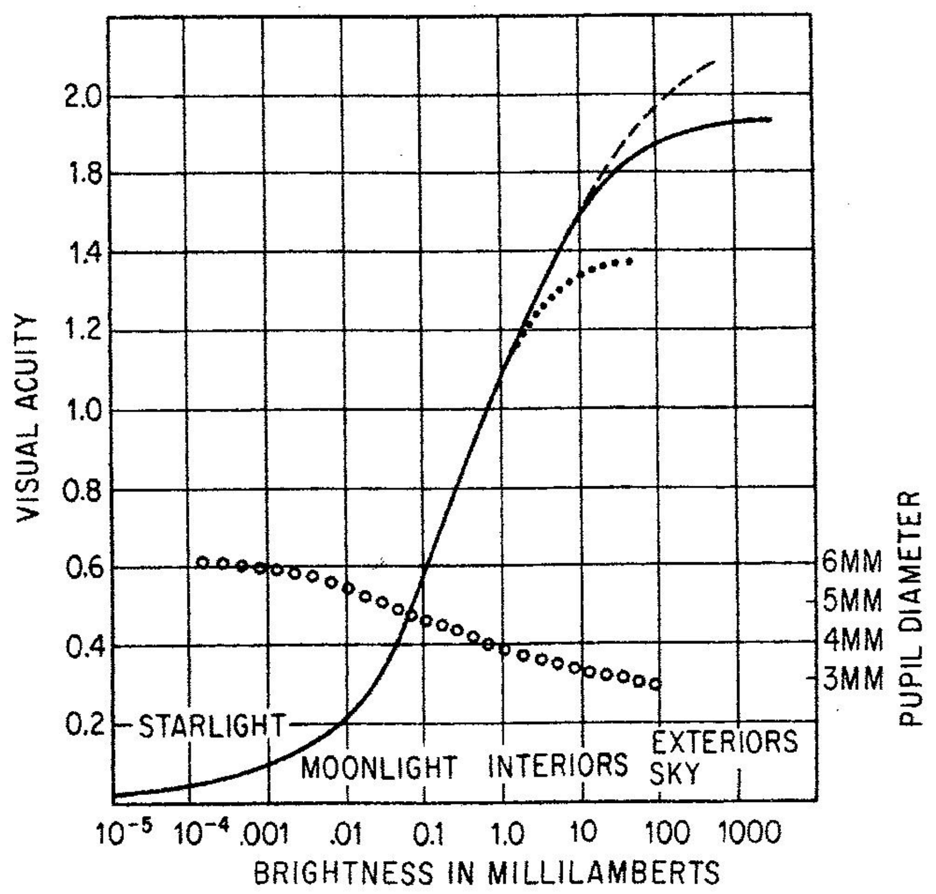

Fig. 11.37. Visual acuity (in 1/min) and pupil diameter (*circles*) as a function of object brightness. The *dashed* and *dotted* acuity lines are, respectively, for increased and decreased surround brightness of 1 milliLambert. (See Table 11.4: 1 milliLambert = 3.183 nit = 3.183 cd/m^2). (From [555]. Reprinted with permission of McGraw-Hill)

RESPUESTA ESPECTRAL RELATIVA

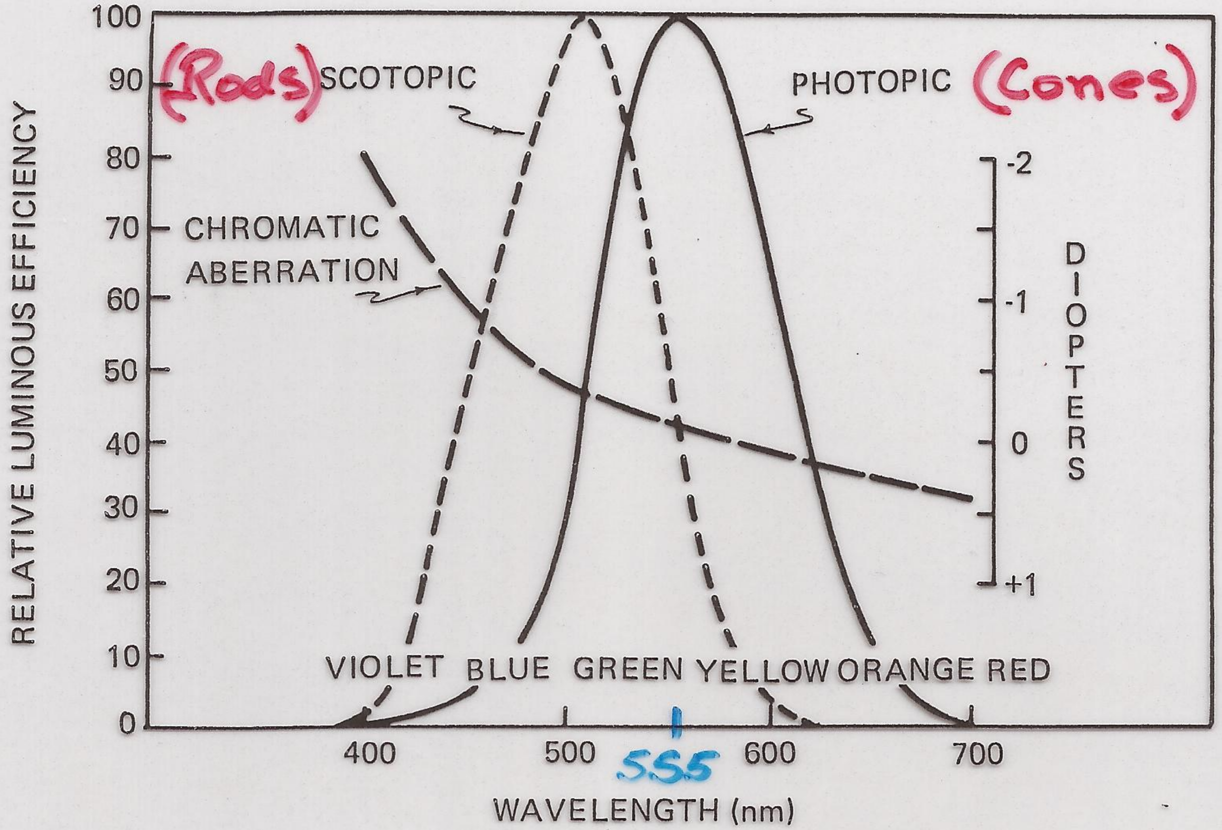

Figure 3-12. The scotopic (night) and photopic (day) responses of the eye. The CIE Function V_λ (photopic) and V'_λ (scotopic) for the CIE standard observer are illustrated as a function of wavelength. Peak rod sensitivy (scotopic) occurs at approximately 500 nm. Also shown is the variation of chromatic aberration as a function of wavelength. Notice the strong chromatic aberration existing in the short wavelength (blue) end of the spectrum. (Adapted from the Military Optical Design Handbook, 1962).

EFICENCIA LUMINOSA ESPECTRAL ABSOLUTA DE CONOS Y BASTONES

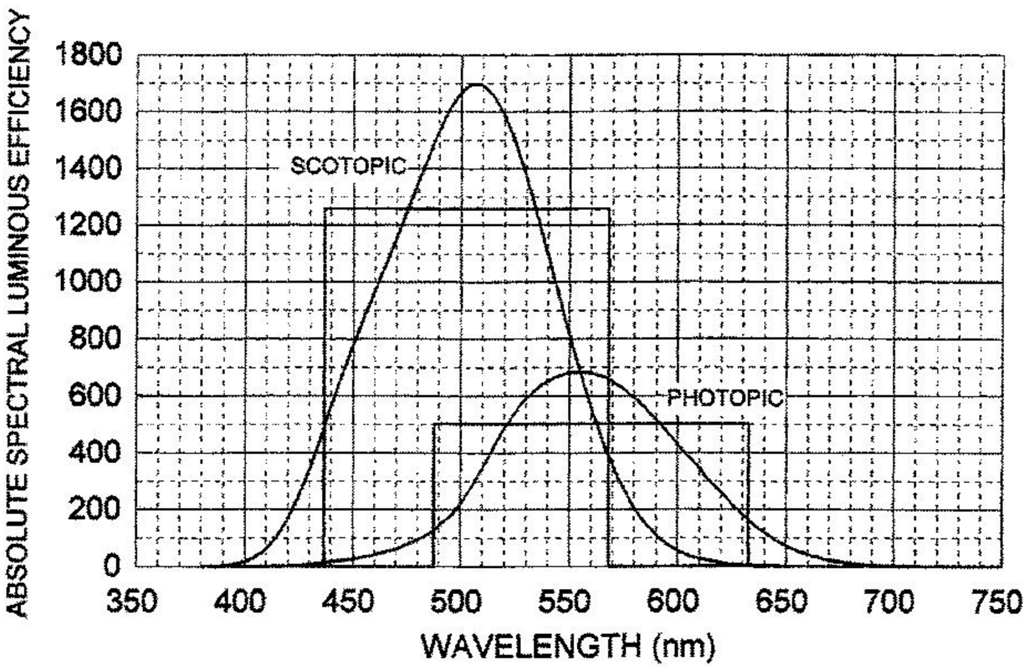

Fig. 11.49. Absolute spectral luminous efficiency of the eye for photopic vision (for normal levels of illumination, also known as the "luminosity curve") and scotopic vision (for dark conditions). The higher the number the more the eye is sensitive to a given light power or intensity at this wavelength. In some presentations each curve is given with its peak normalized to 1. The rectangles associated with each curve are approximations to the real curves. (From [548]. Reprinted with permission of McGraw-Hill)

UMBRAL DE SENSIBILIDAD DEL OJO

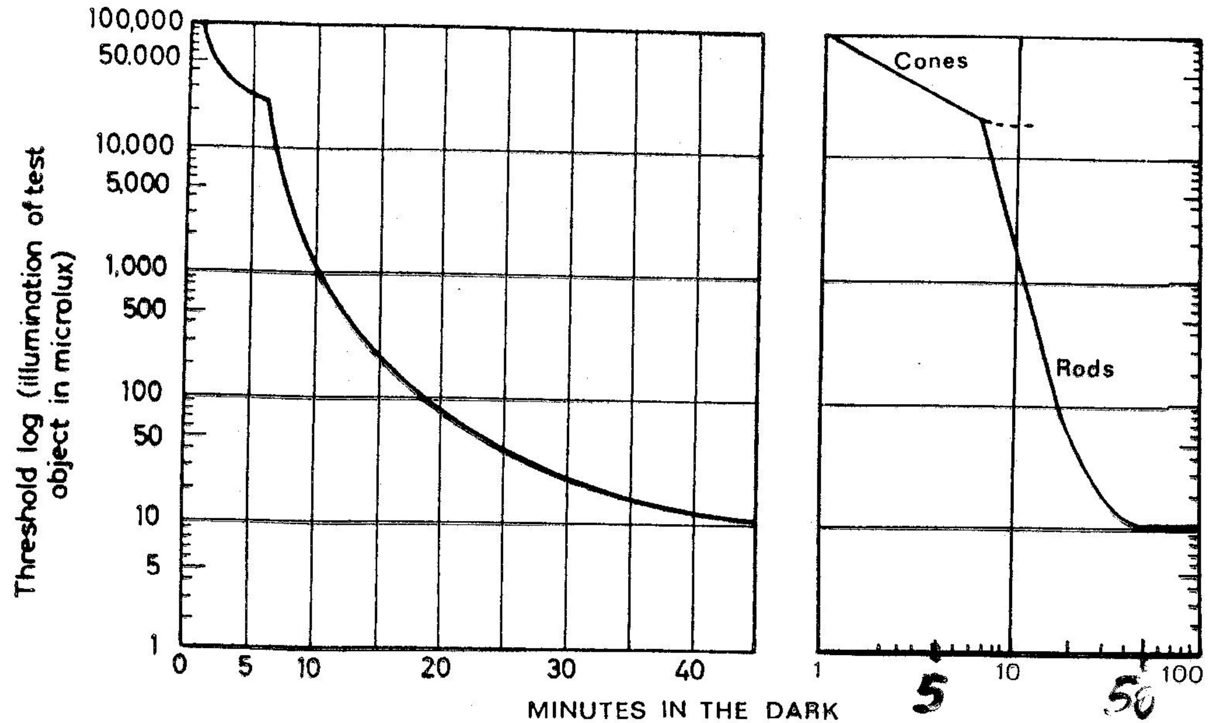

Figure 3-16. The threshold sensitivity of the eye for a point source of light varies as a period of adaptation to the dark. Note that the cones reach a plateau within a matter of 10 minutes, whereas the rods continue to adapt up to periods sometimes exceeding 30 minutes. The dark-adaptation curves are plotted in two panels—one with semi-logarithmic scales (left) and the other with log-log scales. For an extended source the cone plateau is approximately 500 td and the rod plateau is approximately 5×10^{-4} td. These retinal illuminances correspond to source luminances for an 8-mm pupil of 10 cd/m^2 and 10^{-5} cd/m^2 respectively. The unit of troland (td) is often used in these plots since it indicates the retinal illuminance and can be calculated easily from source luminance; i.e., the source luminance in cd/m^2 is multiplied by the pupillary area in mm^2 to obtain trolands.

EFECTO STILES-CRAWFORD I

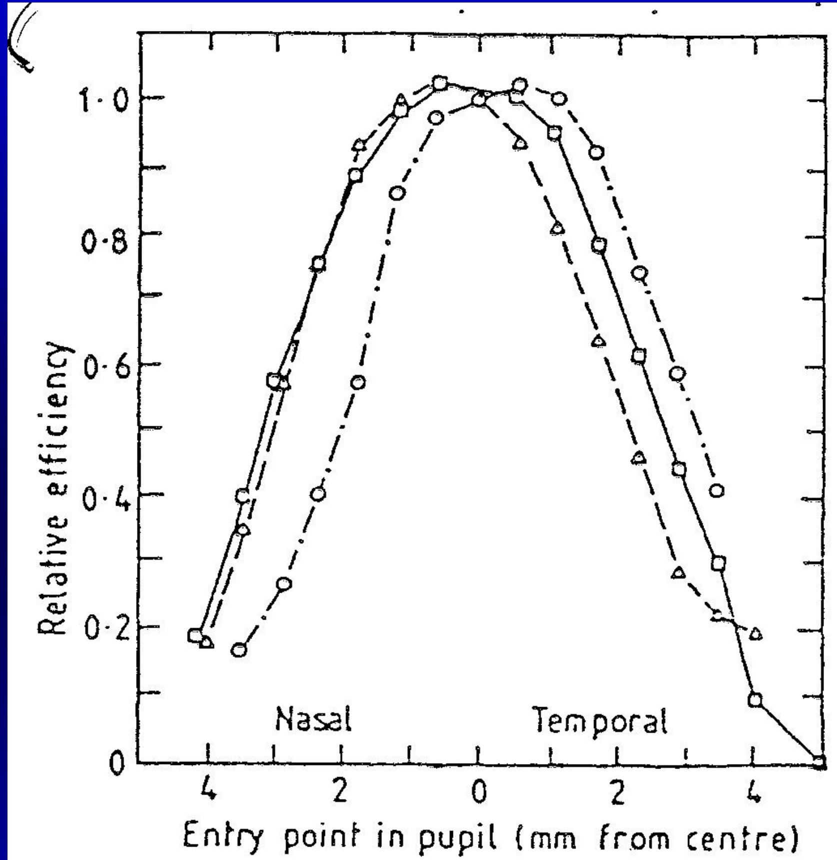

FIGURE 6 The relative luminous efficiency of a foveally viewed target as a function of horizontal pupillary position of the beam, under photopic conditions for three subjects (*after Stiles and Crawford*[91]). Note that the peak of the Stiles-Crawford function does not necessarily lie at the center of the pupil.

EFECTO STILES-CRAWFORD II

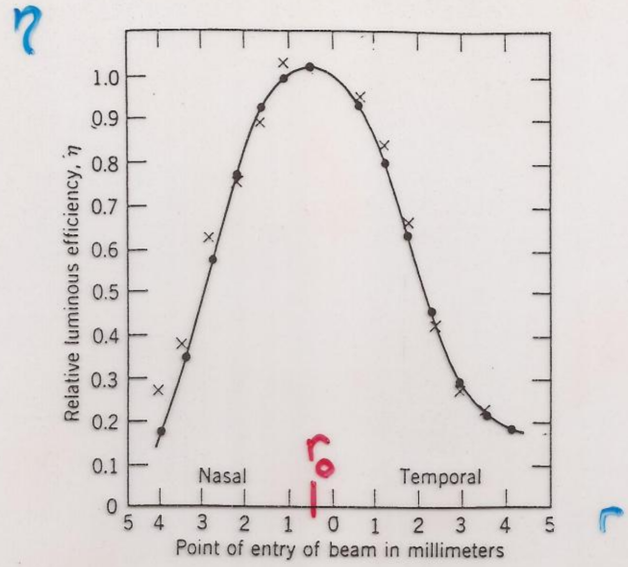

Figure 3-17. The Stiles-Crawford effect. In 1936 Stiles and Crawford discovered that light entering the pupil near the edge of the aperture is greatly reduced in its effectiveness for eliciting a visual response. This effect has been interpreted by many as an indication of the waveguide nature of the cones (adapted from Graham, 1956).

Stiles (1937) $\eta(r) = \exp\left[-p(r-r_0)^2\right]$.

Moon y Spencer (1944) $\eta(r) = 1 - 0{,}0850\,r^2 + 0{,}0020\,r^4$,

ó: $\eta(r) = 0{,}379 + 0{,}621 \cdot \cos(0{,}515 \cdot r)$.

Stiles y Crawford (1958) $\eta(r) = 0{,}25\left[1{,}0 + \cos(9{,}5 \cdot \theta)\right]^2$,

$\operatorname{tg}\theta = 0{,}045 \cdot r$

LEY DE STEVEN RELACIONANDO ESTIMULOS Y PSICOPERCEPCIONES

Table 1.15. Exponent n for perceived strength (P) of a stimulus (S) above a threshold S_0, with $P = K(S - S_0)^n$ in Steven's Law. (Using data from [57, 58])

psychoperception	n	stimulus
brightness	0.33, 0.5	5° target, point source – dark adapted eye
loudness	0.54, 0.60	monoaural, binaural
smell	0.55, 0.60	coffee odor, heptane
vibration	0.6, 0.95	250 Hz, 60 Hz – on finger
taste	0.8, 1.3, 1.3	saccharine, sucrose, salt
temperature	1.0, 1.6	cold, warm – on arm
pressure on palm	1.1	static force on skin
heaviness	1.45	lifted weights
electric shock	3.5	60 Hz through fingers

LEYES DE WEBER-FECHNER

- Experiment:

  Sugiere una expresión como las Leyes de Steven: Es la **Primera Ley de Weber-Fechner**

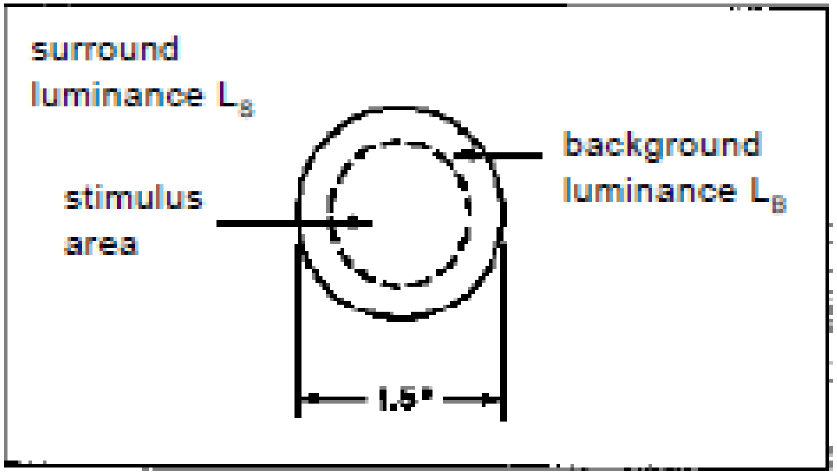

- Result:

  Puede ser de tipo logarítmico

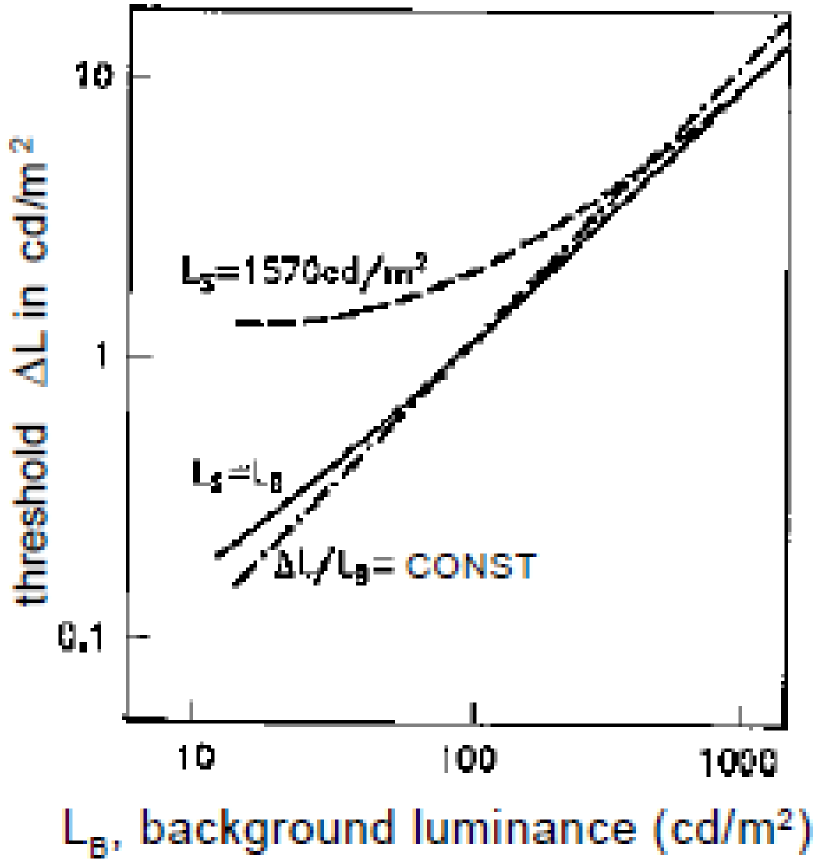

SEGUNDA LEY DE WEBER-FECHNER

- "Weber-Fechner Law"

$$\boxed{\Delta L = cL_B \qquad c = 0.01 \;\ldots\; 0.02}$$

- Implies logarithmic relationship between physical luminance and subjectively perceived brightness.
- Other proposed nonlinearities: square-root, cube-root, polynomials
- γ-characteristic of CRT displays is approximate inverse of nonlinearity of human brightness perception.

ESQUEMA DEL CAMPO RECEPTIVO DE UNA CELULA GANGLIONAR HUMANA Y MODELO DE INHIBICION LATERAL I

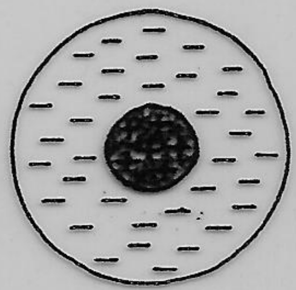

FIGURE 7.11

Schematic receptive field for a human ganglion cell. When light strikes any of the cones in the center of the receptive field, the ganglion is excited (denoted by +'s); when light strikes any of the cones in the surround, the ganglion is inhibited (denoted by −'s).

- Receptive field of a ganglion cell (=fiber of the optic nerve) shows „center-surround response“ with both
  - Lateral inhibition
  - Lateral excitation

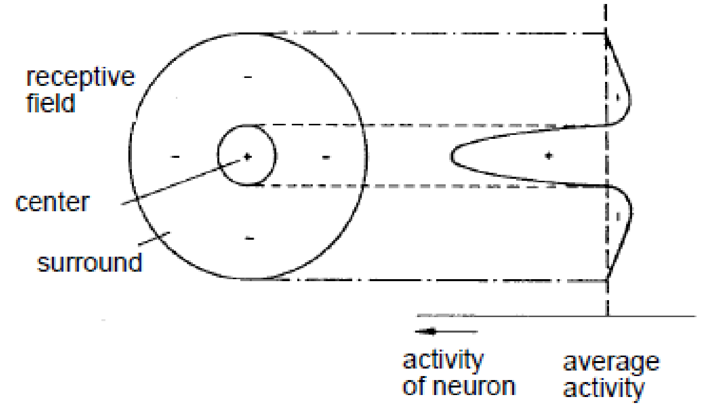

FOTONICA DE LA RETINA HUMANA I

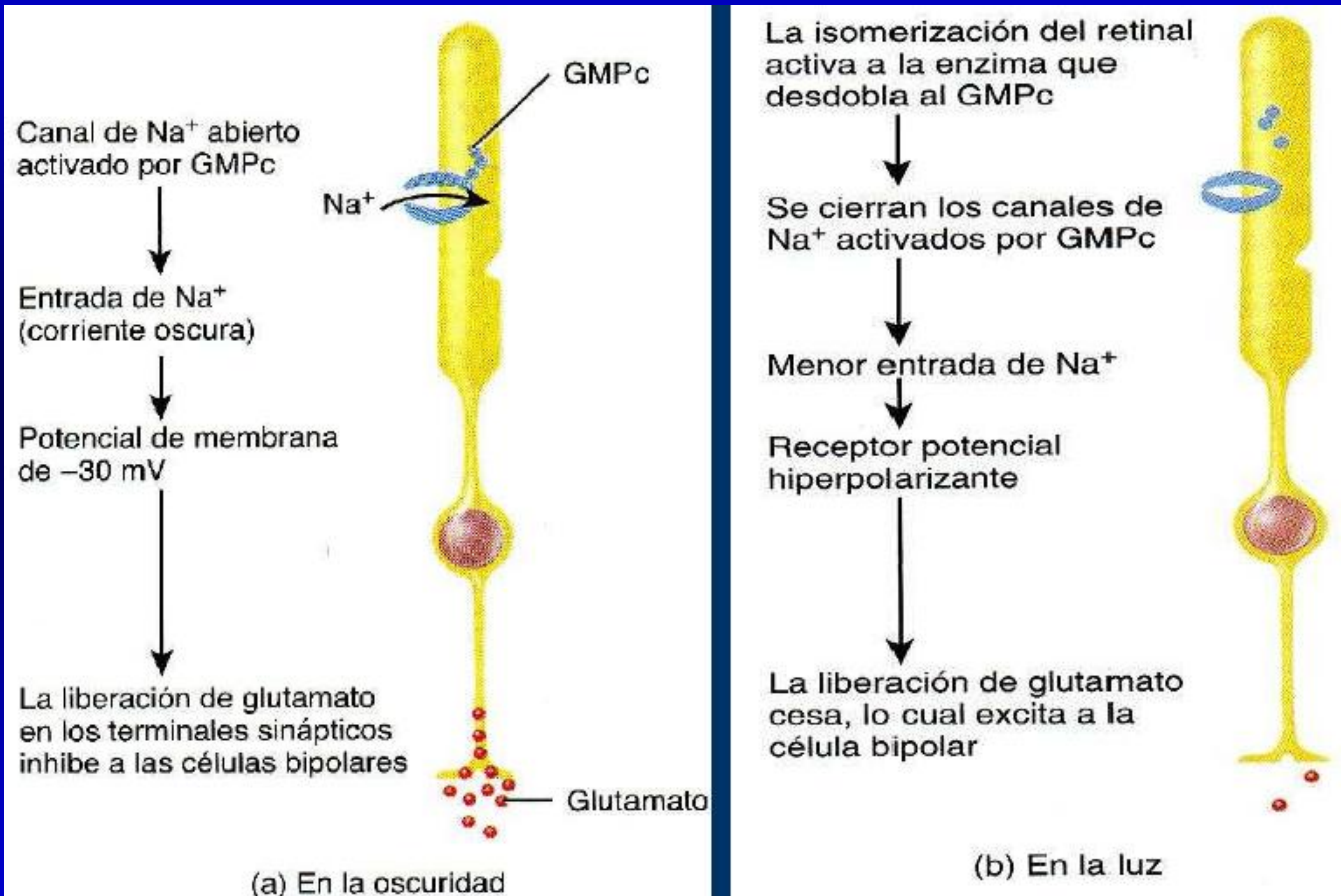

FOTONICA DE LA RETINA HUMANA II

1) En la oscuridad conos y bastones poseen una elevada concentración de monofosfato cíclico de guanosina. Éste se une a los poros de la membrana de los discos y los abre, es decir, aumenta la permeabilidad a los iones de sodio.

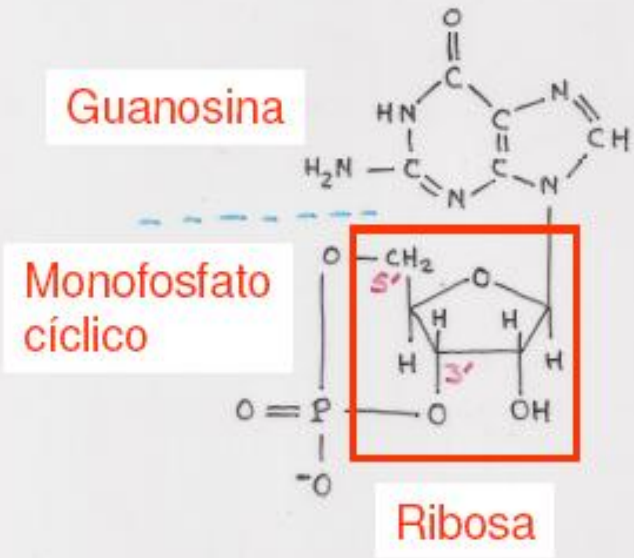

El MFCG es un nucleótido semejante a los que constituyen el ARN. Se compone de una base, la guanina, y un azúcar de 5 carbonos. Se denomina cíclico porque los carbonos 3' y 5' están unidos por el P

2) Las moléculas de rodopsina integran la membrana de los discos "maduros". La rodopsina es una molécula formada por:

Pico de absorción en 380 nm

11-cis retinal + opsina

Pico de absorción en 500 nm.

Derivado de la vitamina A.

Proteína con funciones enzimáticas. Es una cadena polipeptídica de 348 aminoácidos, que adopta la forma de siete hélices.

3) El 11 cis retinal se isomeriza al absorber un fotón, pasando a conformar el todo-trans retinal, con una eficiencia del 50%

Puede ocurrir la isomerización espontánea del retinal. En oscuridad total aparecen pulsos eléctricos semejantes a señales luminosas. En un bastón de retina de mono aparecen cada 2½ minutos, por término medio. El calor es capaz de activar la rodopsina. Vida media del proceso ~ 1000 años.

4) El enlace 3′ y 5′ por el grupo fosfato, llamado fosfodiéster, en estado estable mantiene los poros o canales abiertos. Se comprobó con un parche de membrana de disco en una pipeta de 1 μm.

La isomerización del retinal activa una enzima llamada transducina, la que, a su vez, activa una fosfodiesterasa que actúa sobre el 3′,5′ MFCG insertándole una molécula de H_2O (Hidrólisis) y cerrando los poros. Este proceso rinde un protón (H^+)

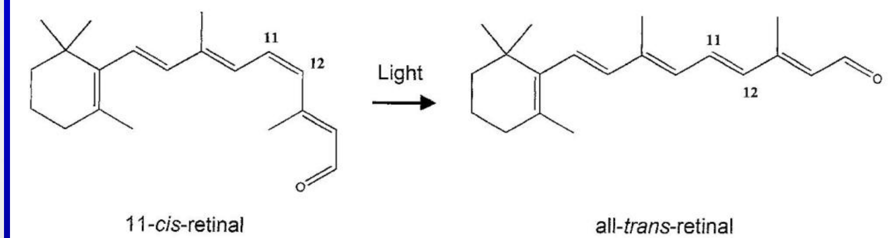

Fig. 11.7. The chromophore 11-*cis* retinal is photoisomerized by light to all-*trans* retinal (11-*trans* retinal)

FOTONICA DE LA RETINA HUMANA IV

FOTOISOMERIZACION EN 2D Y 3D

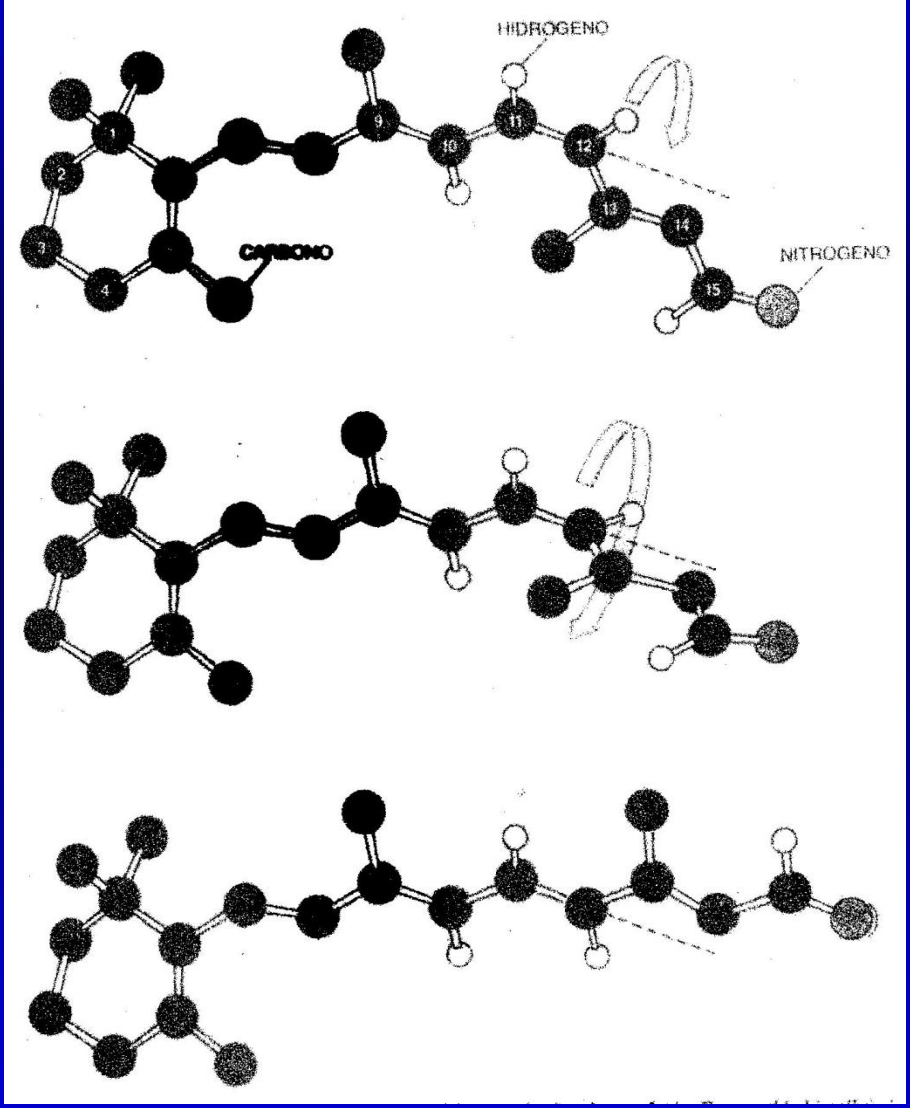

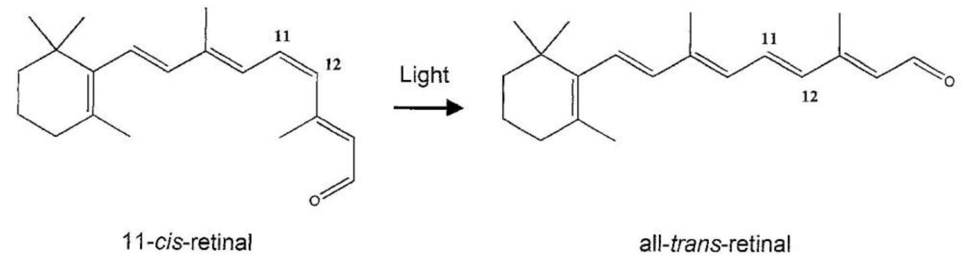

Fig. 11.7. The chromophore 11-*cis* retinal is photoisomerized by light to all-*trans* retinal (11-*trans* retinal)

FOTONICA DE LA RETINA HUMANA V

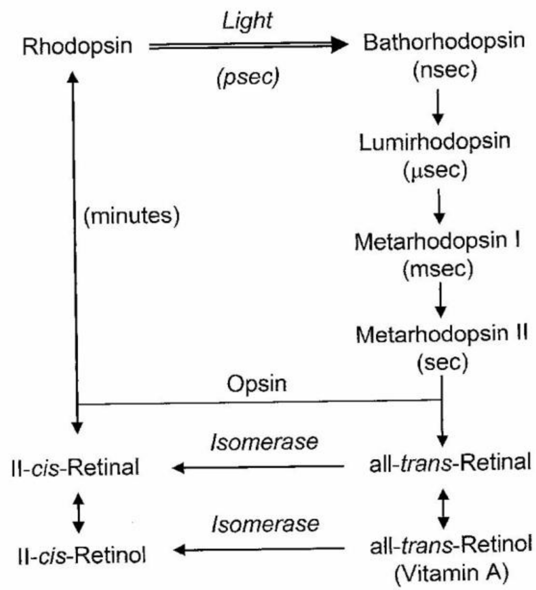

Fig. 11.23. After retinal exposure to light, rhodopsin in the rods reforms slowly by these chemical processes, with the time scales shown. (Based on [526])

5) La transducina se compone de tres segmentos α, β y γ. Uno de ellos, el α, sufre la interacción de la rodopsina activada o rodopsina$^+$, y en ella se sustitye difosfato cíclico de guanosina por trifosfato cíclico de guanosina

Rendimiento del proceso:

fotón — 1 fotón

Rodopsina — 50%

↓

Transducina — 1 molécula de rodopsina$^+$ activa ~71 moléculas de transducina en fragmentos de membrana o ~500 en bastones intactos

↓

Fosfodiesterasa

↓

Monofosfato cíclico de guanosina — 1 molécula de fosfodiesterasa activa ~4200 moléculas de MFCG y rinde ~4200 H^+

Luego:

1 fotón $\longrightarrow$ $\frac{1}{2} \cdot 500 \cdot 4200 \cong 10^6$ protones

GEOMETRIA DE LA ESTEREOPSIS

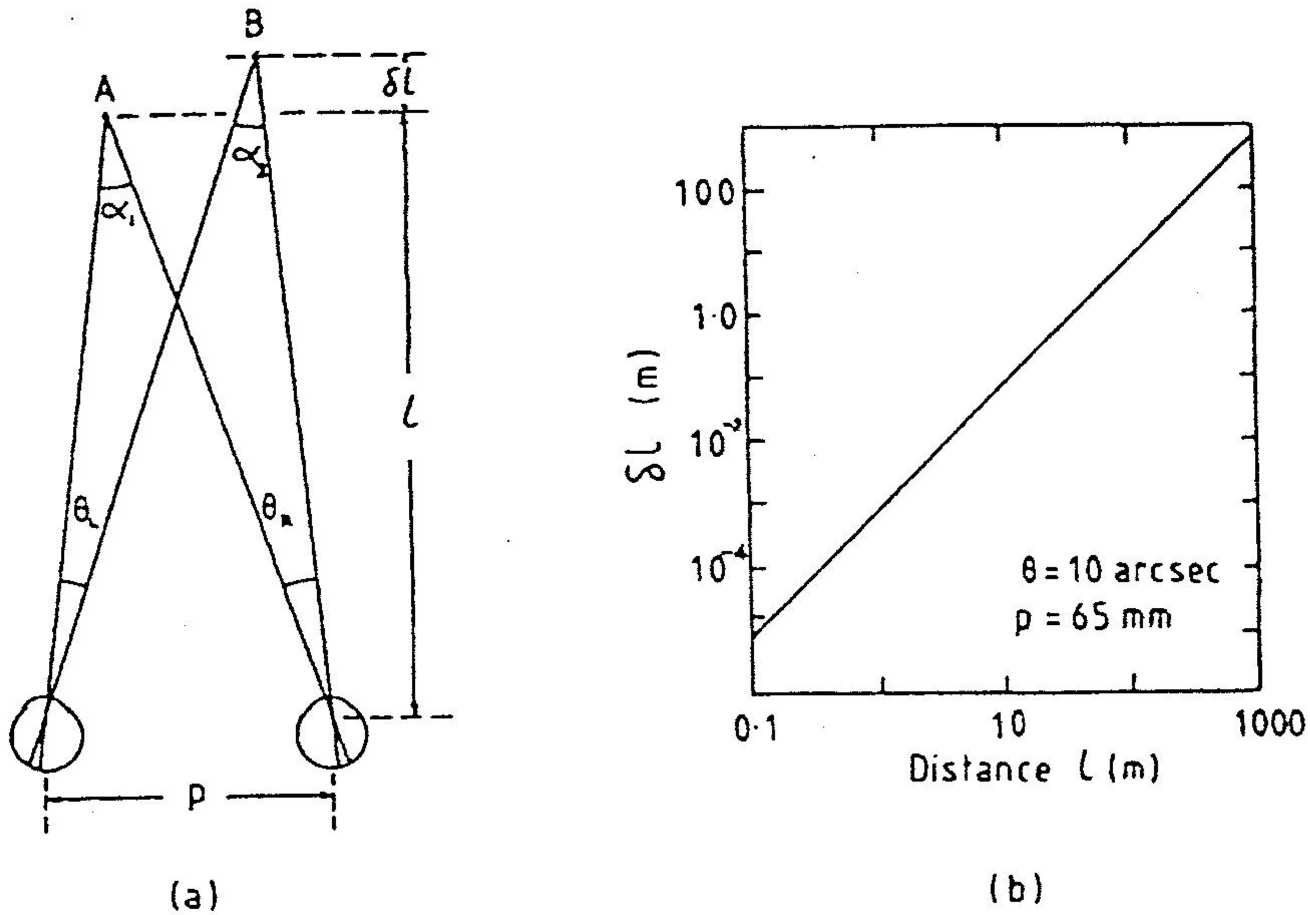

FIGURE 25 (*a*) Geometry of stereopsis. It is assumed that points *A* and *B* can just be discriminated in depth. (*b*) Theoretical just discriminable distance δl as a function of mean object distance l for the assumed values of p and δl indicated.

ESTEREOPSIS Y AMBIGÜEDAD

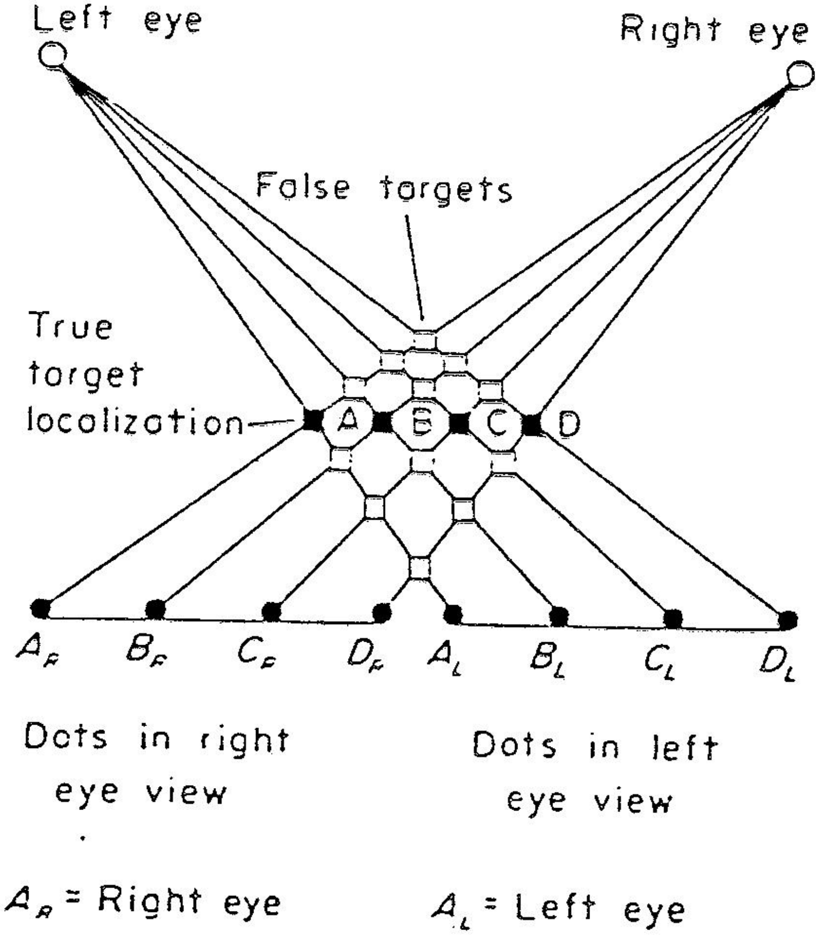

Geometry of stereopsis. Note the inherent ambiguity (false targets) for associating left and right disparity elements. (From Julesz. 1971).

ANATOMIA DE LA ESTREOPSIS I

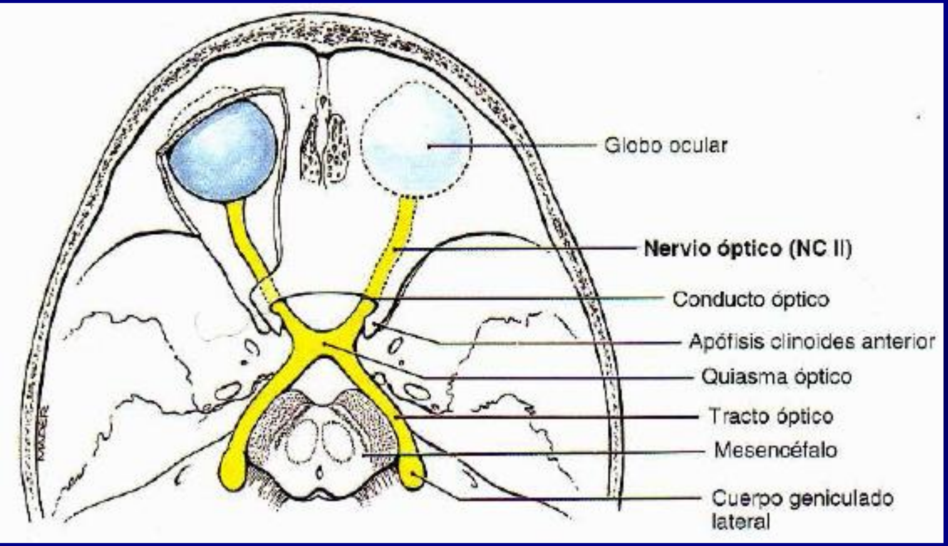

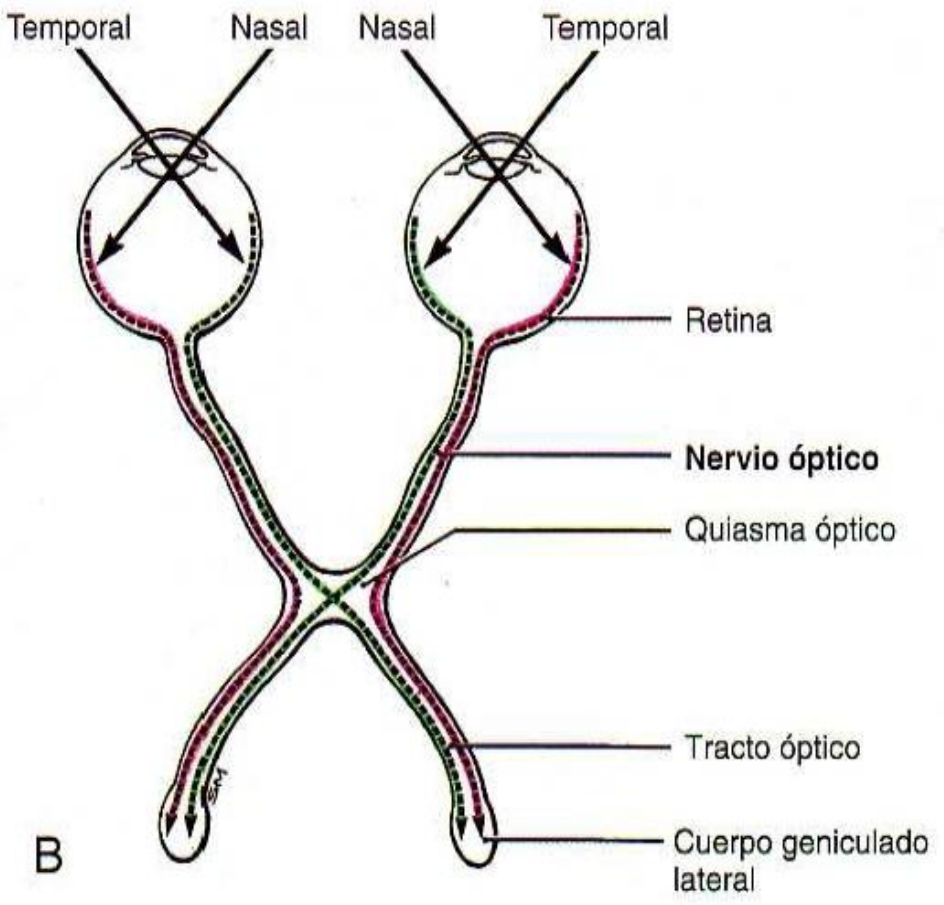

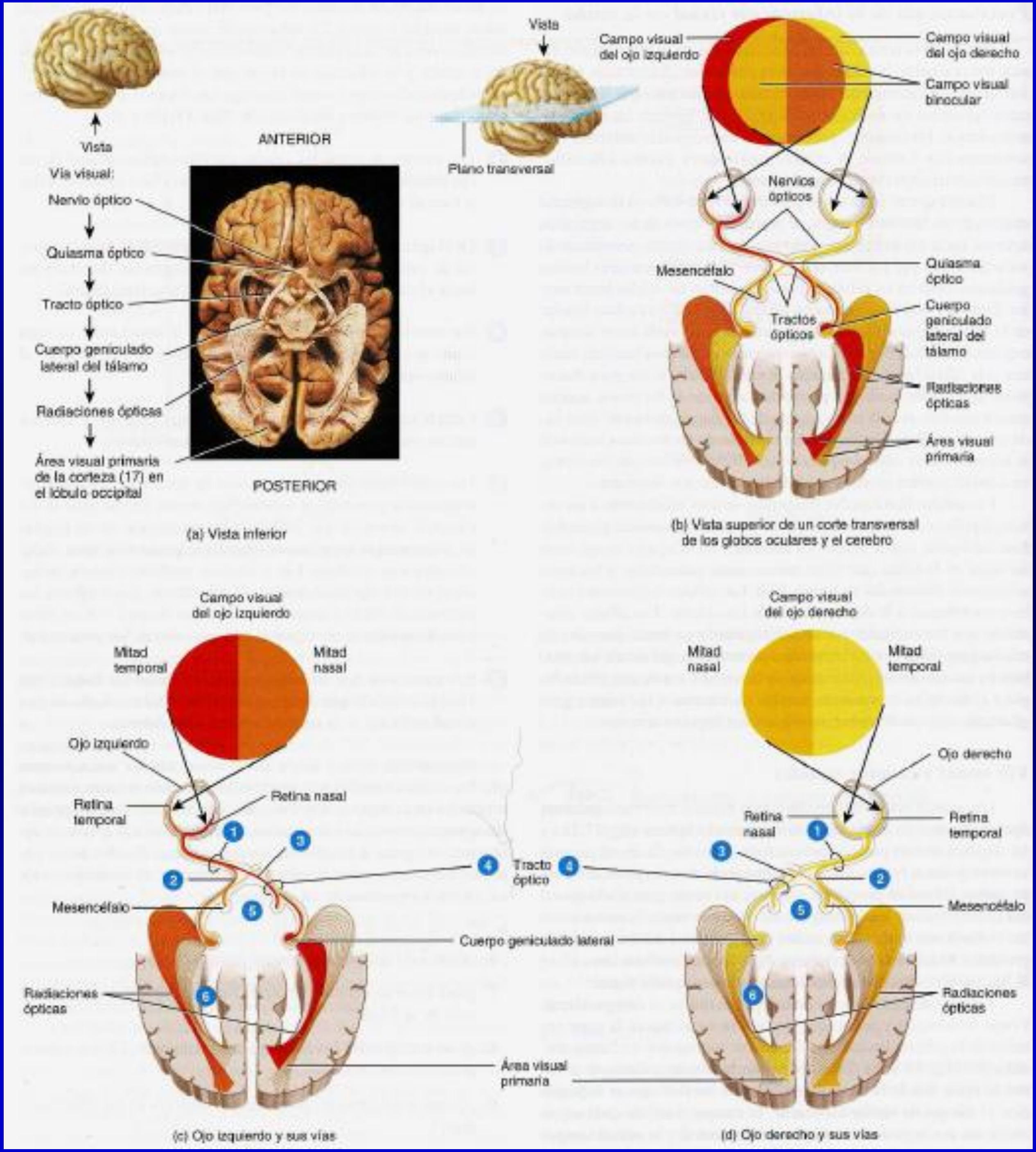

ANATOMIA DE LA ESTREOPSIS II

ESTABILIDAD EN LA FIJACION

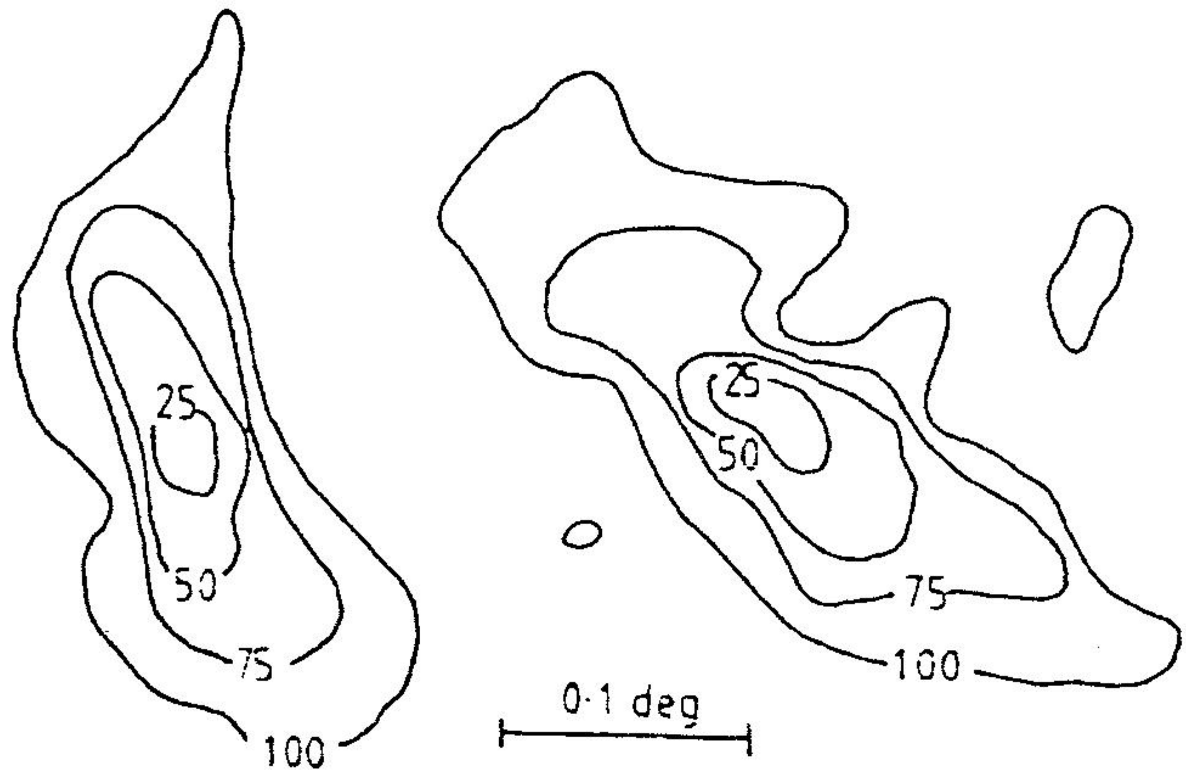

FIGURE 24 Stability of fixation for two subjects. The contours define areas within which the point of fixation was to be found 25, 50, 75, and 100% of the time (*after Bennet-Clark*[339]).

ESTABILIDAD EN LA FIJACION Y LOS MOVIMIENTOS SACADICOS

Instrumental de observación a 300 Hz

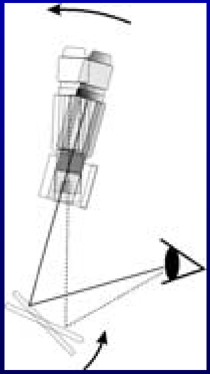

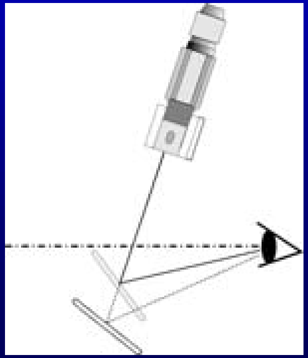

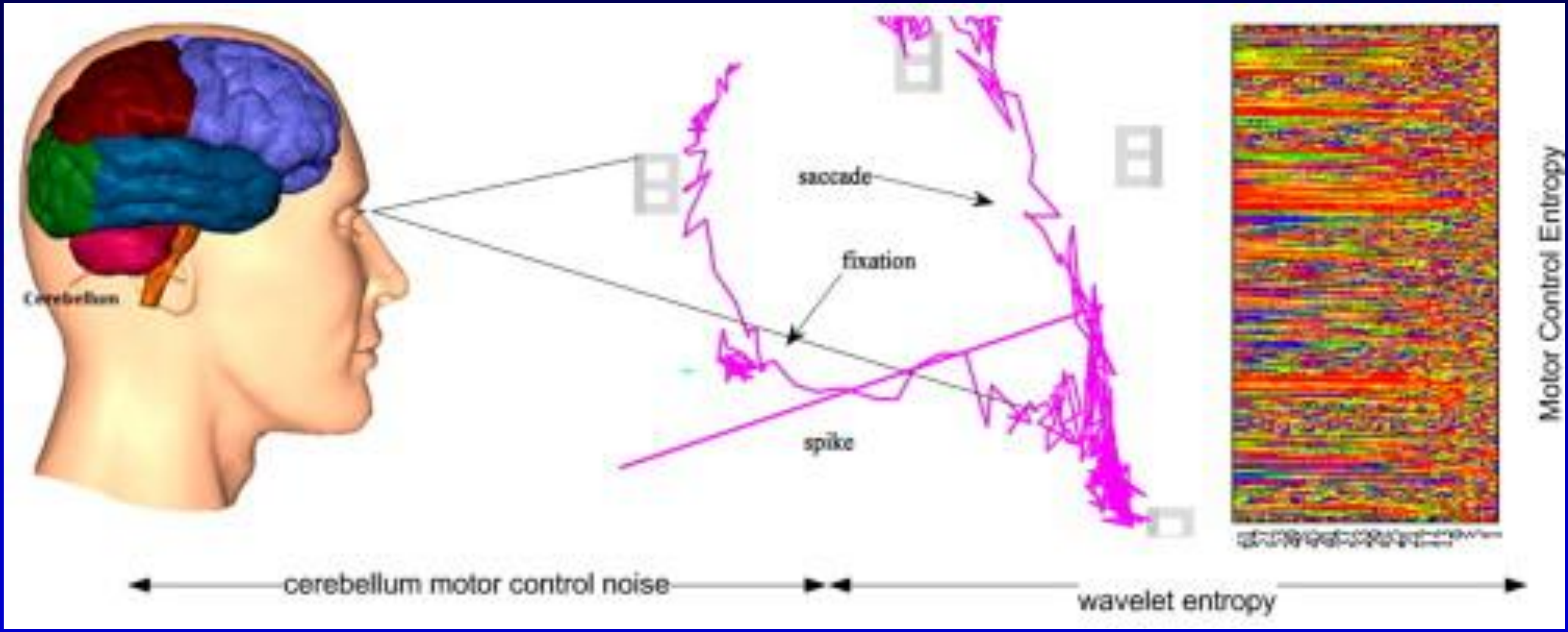

SPIKE DE TRASTORNO CEREBELAR

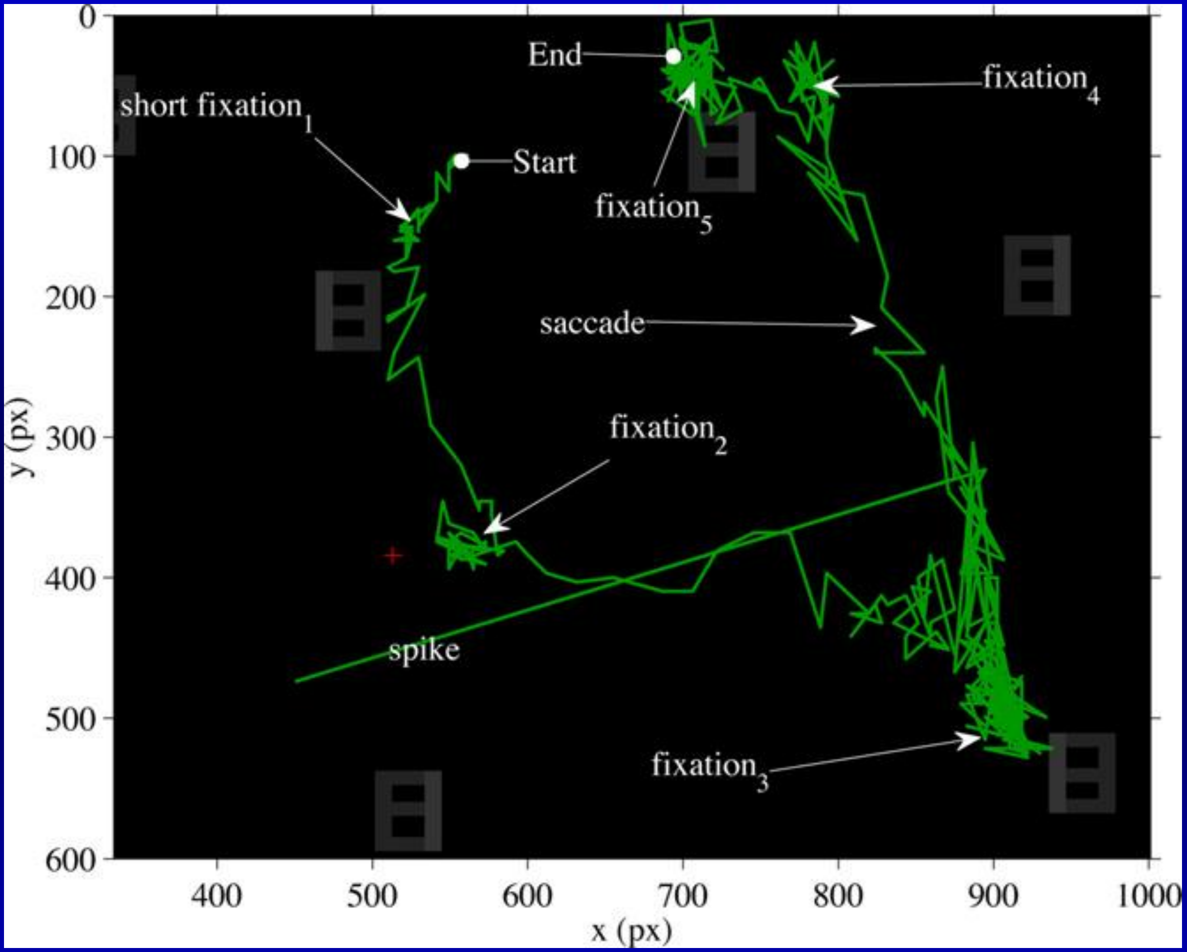

Spike removal through multiscale wavelet and entropy analysis of ocular motor noise: A case study in patients with cerebellar disease

Giacomo Veneri, Pamela Federighi, Francesca Rosini, Antonio Federico, Alessandra Rufa

Journal of Neuroscience Methods *196 (2011) 318–326*

EXPERIENCIA DE PULFRICH I

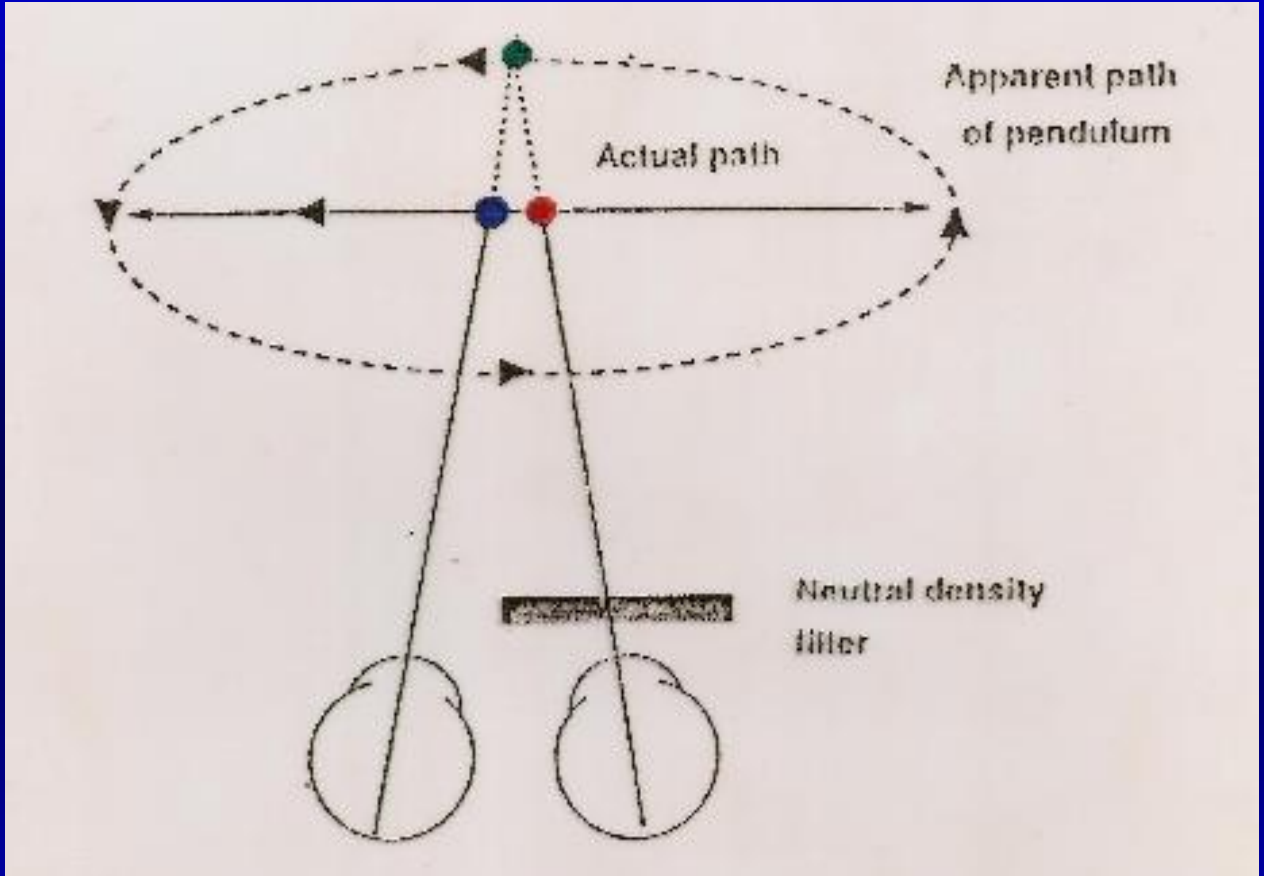

FIGURE 1. Pulfrich effect of a pendulum swinging in the fronto parallel plane, viewed from above. The blue circle is the actual bob, the red circle represents the delayed bob position that the attenuated right eye sees during leftward movement, and the green circle represents the perceived position of the bob. The apparent path of the bob then falls on an ellipse.

EXPERIENCIA DE PULFRICH II

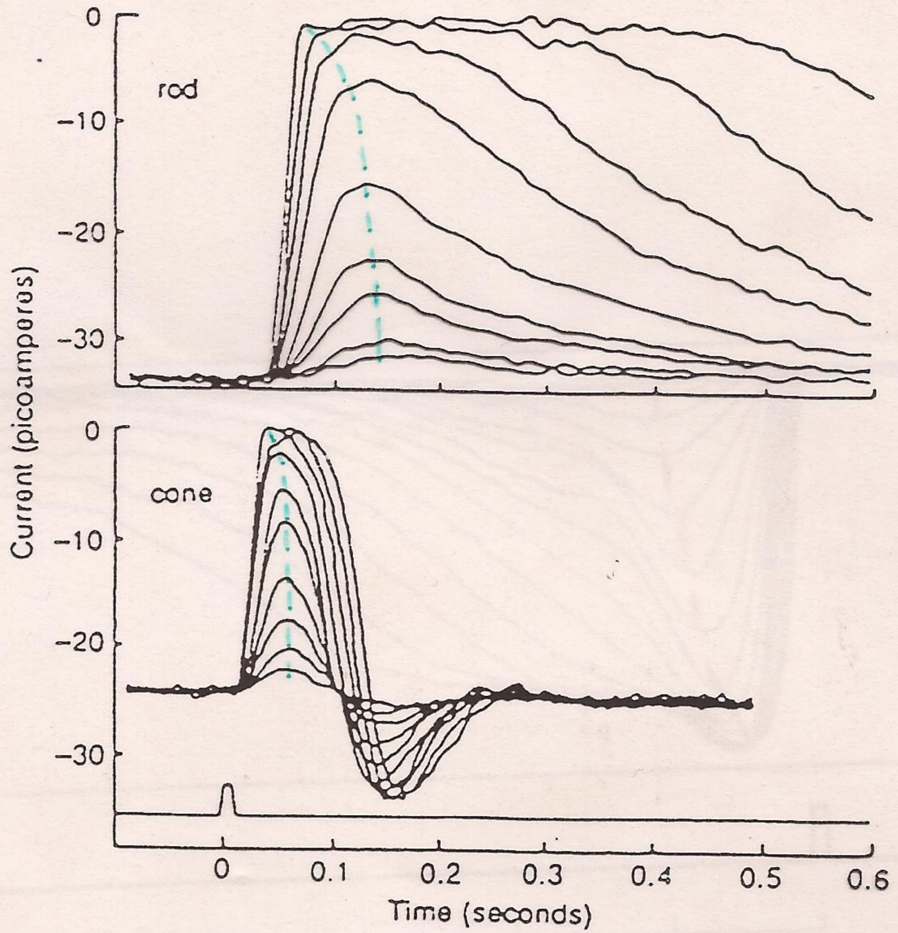

FIGURE 3 Photocurrent responses of macaque rod and cone photoreceptors to flashes of light. Each trace represents the response to a different intensity level. The flash intensities were varied by factors of two. *(From Ref. 23, "How Photoreceptor Cells Respond to Light," Julie Schnapf and Denis A. Baylor. Copyright . © 1989 by . Scientific American, Inc. All rights reserved.)*

EXPERIENCIA DE PULFRICH III

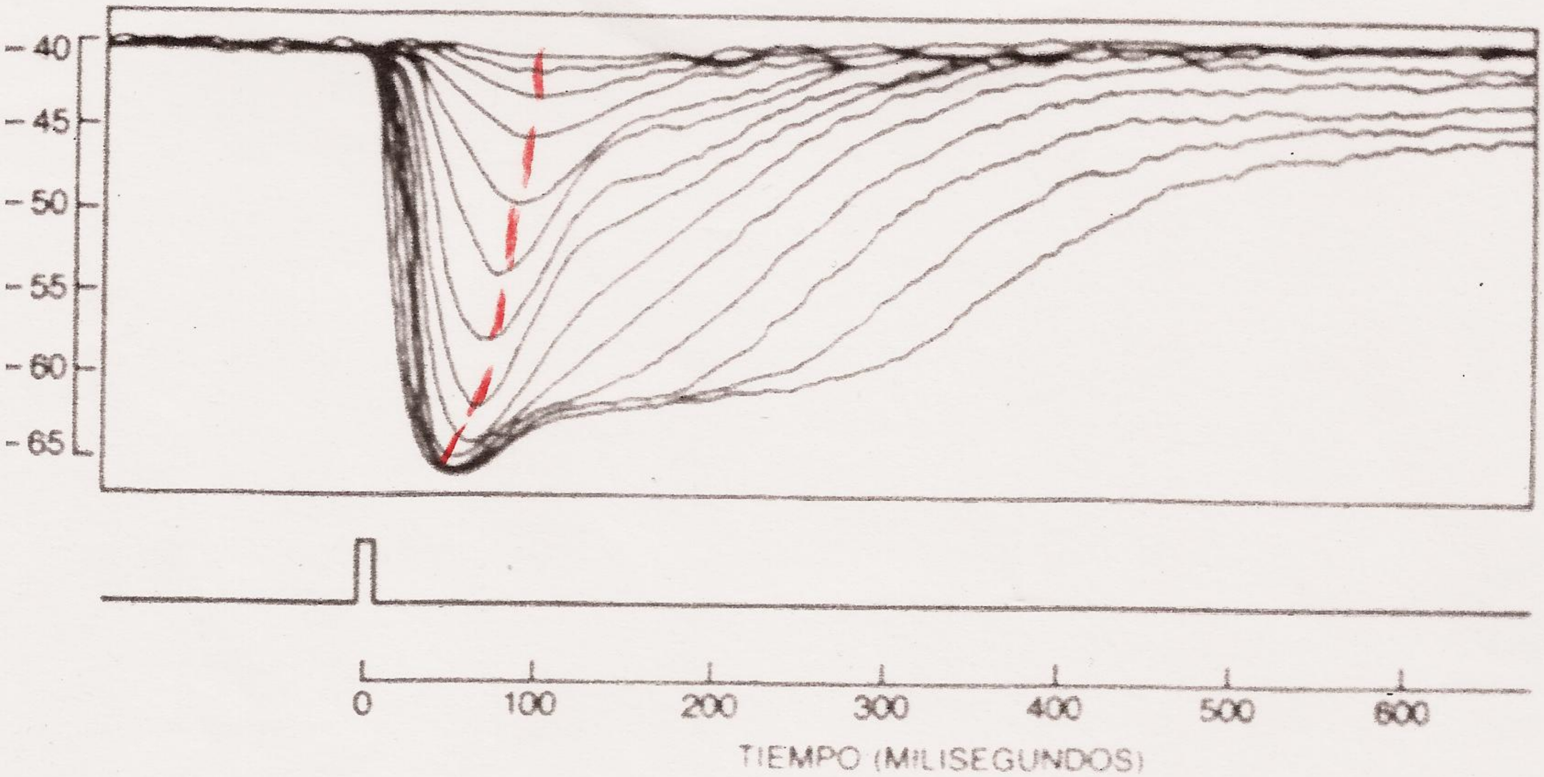

ESPUESTAS DE HIPERPOLARIZACION DEL POTENCIAL de un cono rojo de retina de tortuga, stradas por medio de un electrodo intracelular. Las líneas representan las respuestas, superpuestas, a ellos breves de intensidad creciente. La diferencia del potencial de transmembrana se traza en función iempo transcurrido después del destello, señalado en el eje inferior. Las intensidades de los destellos se entaban en un factor de dos; el destello más débil activaba una cincuentena de moléculas del pigmento absorbía la luz en el cono. Los destellos más luminosos saturaban la amplitud de la respuesta en un imo de casi 30 milivolt, alcanzando el potencial de membrana un valor aproximado de −65 milivolt.

CANTIDAD DE AXONES

1 a 2 x 10^6 por	1/100	100 a 200 millones de conos y bastones.
20.000 por	2/3	30.000 células ciliadas.
2.000 por	$2/10^4$	10 millones de células olfativas.
2.000 por	$2/10^5$	100 millones de células gustativas.
10.000 por	1/50	500 mil células táctiles.
¿...? por	¿...?	3 millones de células sensoras del dolor.

CORTEX VISUAL

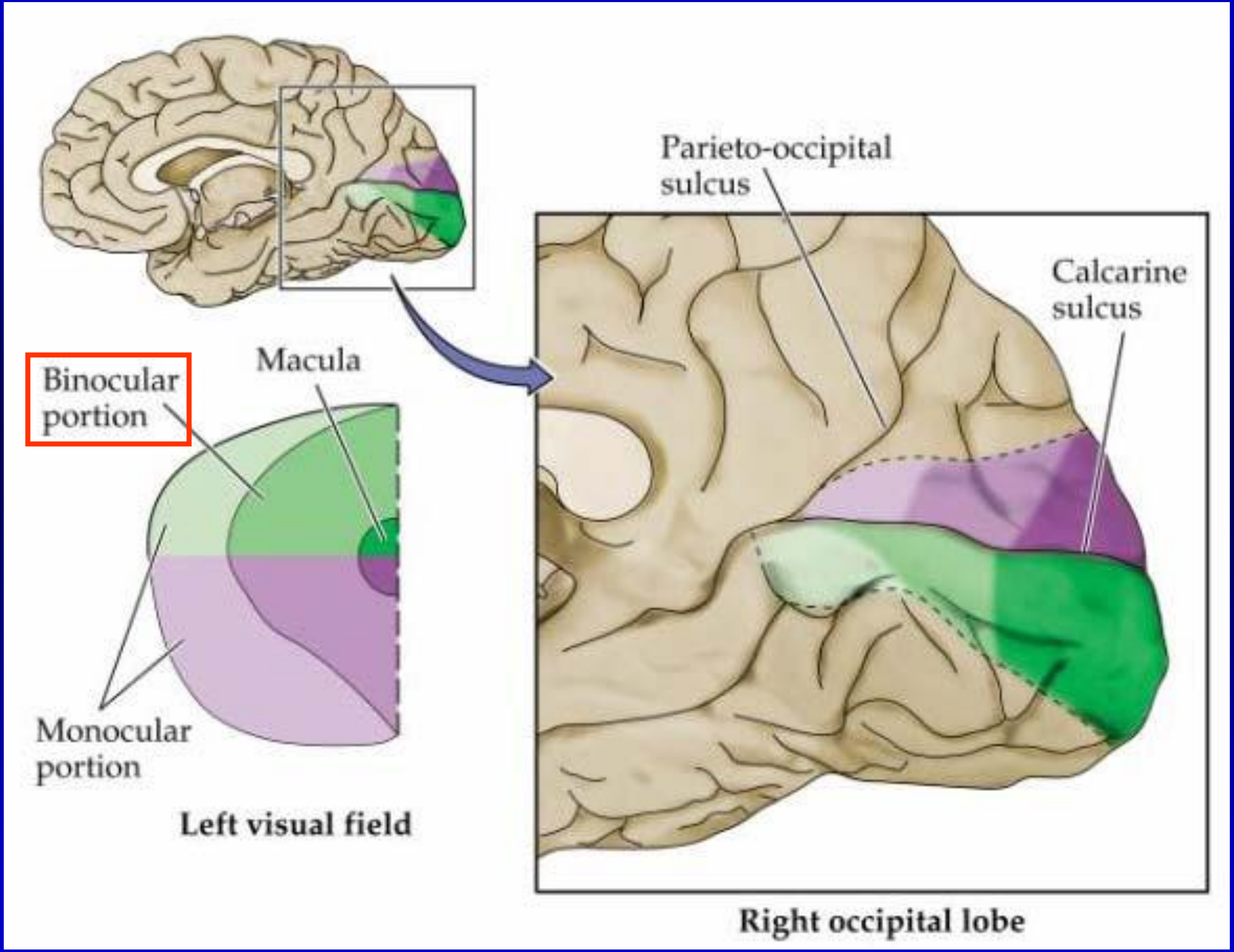

El 80% del Córtex Visual Primario es dedicado al 18% del campo de visión central